

Multimodality Analyses of 3D Flow in a Phantom Model of the Left Ventricle

Hicham Saaid

Promotoren: prof. dr. ir. P. Verdonck, prof. dr. ir. T. Claessens, prof. dr. S. Kenjeres
Proefschrift ingediend tot het behalen van de graad van
Doctor in de ingenieurwetenschappen: biomedische ingenieurstechnieken



UNIVERSITEIT
GENT

Vakgroep Elektronica en Informatiesystemen
Voorzitter: prof. dr. ir. K. De Bosschere
Faculteit Ingenieurwetenschappen en Architectuur
Academiejaar 2018 - 2019

ISBN 978-94-6355-270-7

NUR 954

Wettelijk depot: D/2019/10.500/79

Supervisors:

Prof. dr. Tom Claessens (Ghent University, EA11)

Prof. dr. Pascal Verdonck (Ghent University, EA06)

Prof. dr. Sasa Kenjeres (Delft University of Technology)

Research lab:

Institute Biomedical Technology

Biofluid, Tissue and Solid Mechanics for Medical Applications (bioMMeda)

Ghent University

Corneel Heymanslaan 10 - Blok B (entrance 36)

B-9000 Gent

BELGIUM

Members of the exam committee:

Chairman: *Prof. dr. Filip De Turck* (Ghent University, EA05)

Secretary: *Prof. dr. Joris Degroote* (Ghent University, EA08)

Reading committee:

Prof. dr. Joris Degroote (Ghent University, EA08)

Prof. dr. Patrick Segers (Ghent University, EA06)

Prof. dr. Gianni Pedrizzetti (University of Trieste)

Other member:

Dr. Dan Devos (Ghent University Hospital)

This research was funded by a research grant of the Bijzonder Onderzoeksfonds (BOF) (project 05V01713) and partly by ZonMw within the Innovative Medical Devices Initiative (IMDI), Netherlands program (project Heart Failure and 4D Flow; contract grant number: 104003001).

PREFACE

I have started the PhD-journey with no experience in experimental fluid dynamics. Working with expensive equipment, delicate cameras and dangerous lasers have challenged my patience and practical skills. I have loved to work in a dark room for months, with no windows and with walls painted in black. Yes, in a dark room like a monastery for inner peace (not really peaceful). So, if I needed vitamin D supplements it would not be due to the Belgian weather.

I would like to thank Tom and Pascal for the chance to do this research. A special thanks goes to Tom, my main supervisor. During the course of the project we have shared nice, difficult and interesting moments. We have passed afternoons brainstorming how to design new setups or how to continue the project and chatting on social-economical-scientific hot topics. Thanks to Pascal for his business-oriented advices on how to continue and expand my research. I would like to thank Patrick for his scientific inputs and his help to connect us with new research groups. In fact, we have spent the last two years working with Erasmus MC, TU Delft and Leiden Medical University.

I have passed 8 months in The Netherlands where I have collaborated with top-notch research groups. Which brings me to mention and thank Jason, with who I really enjoyed to collaborate, a super enthusiastic and clever guy. I hope to continue our friendship and to work together again in the future (even from distance). I would like to thank Hans Bosch, Frank Gijsen, Sasa Kenjeres and Jos Westenberg for the opportunity to collaborate with them on the interesting project Heart Failure and 4D Flow. Sasa thanks for hosting me and Jason in your high-tech PIV Lab. Big 'Merci' to Christiaan Schinkel for helping us setting up the tomographic PIV. I would like to express my thanks to Jos for the high-adrenaline MRI experiments, and thanks to Pieter and Hans for their assistance with MRI scans. If it was not for Mehdi, I would have slept in an Airbnb for weeks. Thanks a lot Mehdi for hosting me at your place in Rotterdam. Thanks to my Flemish housemates Pieter and Christophe that I learned a new language, Spanish. In return, they have learned some Italian-Moroccan words, which may be useful in Brussels. I think that they had really supported me in different ways, especially

by cooking amazing food (fine cuisine) more than moral support. I really enjoyed the 'peaceful' atmosphere with you guys (La Crème de la crème).

Although, I have spent a lot of time working in a Dark room, I have had some human being interactions. Which brings me to thank all my colleagues at Polymer group ('Plastic people' B building) and my Italian, Belgian, Iranian, German, Cuban, Brazilian, Portuguese, Slovakian, Danish and Indian colleagues at IBiTech. And a special thank goes to Saskia, Jurgen, Antoine, Frank and Ruddy.

Thanks to my family and my friends wherever they are spread around the world.

Hicham Saaid
Gent, 3 September 2019



TABLE OF CONTENTS

PREFACE	3
TABLE OF CONTENTS	5
NEDERLANDSE SAMENVATTING	9
ENGLISH SUMMARY	13
INTRODUCTION	17
1 Background	21
1.1 ANATOMY AND PHYSIOLOGY OF THE HEART	21
1.1.1 The heart as a pump	21
1.1.2 Pressure and flow	23
1.1.3 Multidisciplinary approach to study cardiac flow dynamics	25
1.1.4 LV flow visualisation 500 years ago	28
1.1.5 LV flow visualisation techniques	29
1.1.6 The role of LV flow	34
1.2 PARTICLE IMAGE VELOCIMETRY	36
1.2.1 2C-2D PIV	38
1.2.2 Seeding	38
1.2.3 Illumination	39
1.2.4 Imaging and processing	40
1.3 STEREOSCOPIC PIV (3C-2D PIV)	43
1.3.1 Calibration and self-calibration	44
1.4 3C-3D PIV TECHNIQUES	46
1.4.1 Reconstructive techniques: Scanning and multiplane PIV	46
1.4.2 Tomographic PIV	47
2 Single-calibration Multiplane PIV within an Idealized Pulsatile Left Ventricle Model	55
2.1 INTRODUCTION	56
2.2 METHODS	57
2.2.1 Optical configuration	57
2.2.2 Imaging system	59
2.2.3 Hydraulic circuit	59
2.2.4 Test fluid and tracer particles	60
2.2.5 Calibration	61
2.2.6 Validation	63
2.3 RESULTS	66
2.4 DISCUSSION	70

2.4.1	Setup limitations and future perspective	71
2.4.2	Conclusions and outlook	73
3	Tomographic PIV in a Model of the Left Ventricle: 3D flow Past Biological and Mechanical Heart Valves	75
3.1	INTRODUCTION.....	76
3.2	MATERIALS AND METHODS.....	77
3.2.1	Left ventricle membrane and tank.....	77
3.2.2	Hydraulic circuit	79
3.2.3	Imaging system and illumination volume	80
3.2.4	Working fluid and tracer particles.....	82
3.2.5	Calibration and volume self-calibration	83
3.2.6	Tomographic analysis.....	84
3.2.7	Measurement protocol	84
3.3	RESULTS AND DISCUSSION	86
3.3.1	Flow Velocity field	87
3.3.2	Inflow characteristics.....	90
3.3.3	Vortical structures.....	91
3.3.4	Kinetic energy.....	93
3.3.5	Limitations	93
3.3.6	Conclusion	95
4	4D Echo-Particle Image Velocimetry in a Left Ventricular Phantom	97
4.1	INTRODUCTION.....	98
4.2	METHODS	100
4.2.1	Left Ventricular Phantom.....	100
4.2.2	Tomographic Particle Image Velocimetry (Tomo-PIV)	101
4.2.3	Ultrasound	102
4.2.4	Beamforming and EchoPIV.....	104
4.3	VISUALIZATION AND COMPARISON.....	106
4.3.1	Vector Comparison	106
4.3.2	Signal-to-Noise Ratio (SNR)	106
4.3.3	Point-spread-function (PSF)	106
4.4	RESULTS	107
4.4.1	Description of flow field.....	107
4.4.2	Quantitative comparison	108
4.4.3	Volume flow rate.....	109
4.4.4	Velocity magnitude.....	111
4.4.5	SNR and PSF.....	112
4.5	DISCUSSION	112

4.5.1	Underestimation in jet.....	113
4.5.2	PSF & Kernel Size.....	113
4.5.3	SNR	114
4.5.4	Clutter	114
4.6	LIMITATIONS	114
4.6.1	LV phantom.....	114
4.6.2	Imaging View.....	115
4.6.3	Contrast Agent	115
4.6.4	Analyses	115
4.7	FUTURE PERSPECTIVES	116
4.7.1	Resolution	116
4.7.2	SNR	116
4.7.3	Frame Rate	116
4.7.4	MRI	117
4.8	CONCLUSION.....	117
5	Comparison of Two Accelerated 4D Flow MRI Sequences with Tomographic PIV in a Pulsatile Left Ventricle Phantom.....	119
5.1	INTRODUCTION.....	119
5.2	METHODS	122
5.2.1	The phantom model	122
5.2.2	Hydraulic circuit	123
5.2.3	MRI setup and acquisition.....	123
5.2.4	Tomographic PIV: setup	126
5.2.5	Tomographic PIV: Calibration, measurement protocol and analysis.....	126
5.3	PRELIMINARY RESULTS AND DISCUSSION.....	127
5.3.1	Comparison: EPI vs FFE	127
5.3.2	Comparison: Tomo-PIV vs EPI and FFE	130
5.4	CONCLUSIONS	131
6	Conclusions and future perspectives.....	133
6.1	CONCLUSIONS	133
6.2	FUTURE PERSPECTIVES.....	136
6.2.1	Clinical challenges.....	136
6.2.2	Technical challenges	137
6.2.3	Technological advancements in the field of PIV	139
7	Appendix: Technical drawings	141
8	Bibliography.....	157

NEDERLANDSE SAMENVATTING

Hoofdstuk 1

Dit hoofdstuk start met een korte inleiding tot de anatomie en fysiologie van het cardiovasculaire systeem en in het bijzonder van het linker ventrikel (LV). Daarna volgt een uitleg over de multidisciplinaire aanpak die wetenschappers hanteren bij het onderzoek naar de vloeistofdynamica in het LV. We beschrijven de algemene werkingsprincipes van traditionele en opkomende medische beeldvormingstechnieken, en geven de nodige achtergrondinformatie over numerieke simulaties en experimentele technieken. Dit eerste deel eindigt met een gedetailleerde beschrijving van de intraventriculaire stromingsstructuren die zich vormen tijdens de vullingsfase en een beknopte toelichting van de potentiële implicaties van de LV stroming voor de hartfunctie.

In het tweede deel focussen we op experimentele technieken om de stroming te visualiseren. In het bijzonder weiden we uit over de werkingsprincipes en relevante parameters van de experimentele meettechnieken voor de stromingssnelheid die gebruikt werd in het kader van dit doctoraat: Particle image velocimetry (PIV). De PIV-methode legt het verband tussen de verplaatsing van deeltjes in een kort tijdsinterval tussen twee opeenvolgende afbeeldingen om de snelheid van de onderzochte vloeistof te meten. Omwille van zijn hoge ruimtelijke resolutie en het feit dat het de stroming niet verstoort, wordt PIV vaak beschouwd als de standaardmeetmethode voor in vitro studies in het domein van de vloeistofdynamica. De informatie die conventionele PIV kan verschaffen over het stromingssnelheidsveld, m.n. twee snelheidscomponenten in één vlak, is echter beperkt. Een aanzienlijke verbetering in vergelijking met conventionele PIV is stereoscopische PIV. Met deze techniek kan de derde snelheidscomponent ook achterhaald worden. De opstelling wordt echter complexer omwille van de kijkhoek van het camerasysteem. Een zorgvuldige kalibratie is dus vereist om de mappingfunctie tussen de ruimtelijke coördinaten en het referentiesysteem van het vlak van de camera's te schatten. Verder worden nog een aantal voorbeelden behandeld die aantonen hoe stereoscopische (en conventionele) PIV kan ingezet worden voor metingen in meerdere parallele vlakken.

Tot slot volgt een uiteenzetting over de tomografische PIV-techniek, die wordt beschouwd als de “ware” volumetrische techniek voor stromingssnelheidsmetingen. We bespreken de volumetrische kalibratieprocedure en de invloed van experimentele parameters op de kwaliteit van de meting.

Hoofdstuk 2

Het in kaart brengen van de stromingspatronen in het LV kan helpen bij de ontwikkeling en interpretatie van stromingsgebaseerde parameters om de hartfunctie te beoordelen. Het visualiseren van de driedimensionale stromingspatronen in een ondoorzichtige en bewegende kamer in vivo is echter complex. Dit is reeds aangetoond in verschillende recente multidisciplinaire studies waar in vivo beeldvormingstechnieken worden gecombineerd met computersimulaties en/of andere in vitro methodes. Omwille van zijn specifieke eigenschappen wordt PIV volop gebruikt om stromingsdynamica in het cardiovasculaire domein te onderzoeken. Volledig volumetrische PIV-data gemeten in een dynamisch veranderende geometrie zoals het LV blijven echter zeldzaam. Dit verantwoordt de huidige studie. Een onderzoek naar de LV stroming die gebruik maakt van een speciaal gemaakte cardiovasculaire simulator wordt beschreven. Deze simulator bestaat uit een flexibel membraanmodel van het LV met een geïdealiseerde vorm, aangedreven door een programmeerbare zuigerpomp. Een multiplane scanning stereoscopisch PIV wordt efficiënt ingezet om in meerdere onafhankelijke vlakken over het meetvolume heen te meten. Omwille van de bereikte hoge nauwkeurigheid bij het verplaatsen van het belichting -en beeldvormingssysteem kan met de setup de stroming in een driedimensionaal volume gereconstrueerd worden met slechts één kalibratie. De effecten van de oriëntatie van een mitralisklepprothese in anatomische en anti-anatomische configuraties werden onderzocht tijdens de diastolische vulling. De meting is uitgevoerd volgens de phase locking strategie om de meetfout te reduceren. De gereconstrueerde driedimensionale stromingsstructuren stroomafwaarts van de tweebladige mitraalklep worden getoond en de gemiddelde snelheidscomponenten worden voorgesteld, samen met de vorticititeit en turbulente kinetische energie.

Hoofdstuk 3

Om het inzicht te verbeteren in de intraventriculaire vloeistofmechanica en de impact van verschillende soorten klepprothesen hierop, hebben we een verbeterd anatomisch realistische dynamische fantoom van het linker ventrikel ontworpen. De vorm is afgeleid van een dataset van CT opnames van 150 patiënten. Een biologische, een eenbladige en tweebladige mechanische klep (in twee verschillende oriëntaties) werden achtereenvolgens gemonteerd in de mitralispositie en getest onder dezelfde condities. Om de driedimensionale stroming in het fantoom te onderzoeken hebben we een tomografische PIV (Tomo-PIV) opstelling gebouwd met twee camera's en een spiegelsysteem om in totaal vier aanzichten te simuleren. De resultaten laten toe de evolutie van de driedimensionale stromingstopologie, de vortexstructuren en de

kinetische energie in het linkerventrikel tijdens de hartcyclus te vergelijken. Alle geteste kleppen, met uitzondering van de eenbladige klep, zorgden voor een stroming waarbij de uitstroom de instroom kruist, onder de mitralisklep. Een asymmetrische jet werd waargenomen wanneer de twebladige klep in de anatomisch correcte opstelling gemonteerd werd, terwijl de jet bijna symmetrisch bleef in de anti-anatomische opstelling. De biologische klep toont de sterkste jet met een pieksnelheid die bijna dubbel zo hoog lag in vergelijking met de mechanische hartkleppen, waardoor de jet dieper in de caviteit doordrong. De maximale kinetische energie in het LV in het geval van de biologische klep is dan ook ongeveer vier keer hoger dan bij de mechanische hartkleppen. We besluiten dat de tomografische PIV-opstelling een nuttige referentiemeting van stromingseigenschappen oplevert en de mogelijkheid biedt om het effect van de verschillende types kleppen op de stromingspatronen in het LV te vergelijken.

Hoofdstuk 4

In dit hoofdstuk beschrijven we een 4D echografisch Particle Image Velocimetry (Echo-PIV) systeem met hoge beeldfrequentie op basis van een prototype van een transoesofagale probe in combinatie. De nauwkeurigheid van het Echo-PIV in geval van complexe stromingspatronen in een dynamisch LV fantoom werden nagegaan en vergeleken met de resultaten verkregen met optische Tomo-PIV gebruikt als referentie. Echo-PIV en Tomo-PIV stemden overeen wat betreft de globale LV stromingspatronen, maar Echo-PIV bleek de kleinere stromingsstructuren af te vlakken. Echo-PIV onderschatte ook de stroomsnelheden op grotere beelddieptes, terwijl de PIV kerngrootte en de puntspreidingsfunctie van de transducer relatief groot waren ten opzichte van de snelheidsgradiënten. De resultaten zijn veelbelovend en tonen aan dat de 4D Echo-PIV uitgevoerd kan worden in slechts vier hartcycli, waarbij de adem dus maar beperkte tijd moet worden ingehouden. Er is echter nog een werkwijze nodig om hogesnelheidsgradiënten in de zones met beperkte spatiale resolutie om te zetten alvorens deze methode klinisch vertaald kan worden.

Hoofdstuk 5

4D flow MRI is een veelbelovende medische beeldvormingstechniek die toelaat om met één enkel onderzoek zowel anatomische als functionele beeldinformatie te verschaffen. 4D flow MRI is een verbetering van de fase contrast MRI met codering van de stromingssnelheid in alle ruimtelijke richtingen. Het laat toe het snelheidsvectorveld te meten in een driedimensionaal domein en zodoende de hemodynamische parameters te schatten. De matige resolutie (zowel in tijd als in ruimte) en de gevolgen hiervan op

de lange scantijd leiden tot informatieverlies. Ook de verschillende pulssequenties zijn nog niet voldoende gevalideerd, zoals recent geconcludeerd werd in een consensus paper. Dit belemmert het gebruik van 4D flow MRI in de klinische praktijk. Er zijn echter nog maar zeer weinig studies uitgevoerd, de meeste bovendien met een vereenvoudigde geometrie, waarin de 4D flow MRI vergeleken wordt met referentiedata. Hier hebben we 4D flow MRI-metingen uitgevoerd met verschillende versnelde pulssequenties (EPI, FFE en TFE) in ons realistisch LV model. We stellen de preliminaire resultaten voor van de vergelijking tussen de snelheidsvectoren verkregen met 4D flow MRI en met Tomo-PIV.

ENGLISH SUMMARY

Chapter 1

This chapter starts with a brief introduction to the anatomy of the heart and the hemodynamic events that occur during the cardiac cycle, specifically within the LV. Then it continues explaining the multidisciplinary approach taken by a wide range of scientists that are interested in LV flow dynamics from different perspectives. Therefore, we illustrate the general working principles of conventional and emerging medical imaging techniques, numerical simulations and experimental techniques. This first part ends with a detailed description of the intraventricular flow structures that form during the filling phase with a concise explanation of the potential implication of LV flow in cardiac function.

In the second part, we focus on experimental flow visualization techniques. Specifically, we provide detailed notions on the working principles and relevant experimental parameters of the adopted flow velocity measurement technique during the PhD project: *Particle image velocimetry* (PIV). Essentially, the PIV method relates *particle* displacement over a short time interval between two consecutive *images* to *measure* the *velocity* of the fluid under investigation. Due to its high spatial resolution and non-intrusive character, PIV is often considered as the gold standard approach for in vitro fluid dynamics studies. However, the conventional PIV provides limited information (two velocity components in one plane) on the flow velocity field. An important upgrade of the conventional PIV is stereoscopic PIV, which allows to recover the third velocity component. The setup complexity increases with stereoscopic PIV due to the viewing angle of the camera system. Therefore, a careful calibration is needed to estimate the mapping function between the spatial coordinates and the camera plane reference system. The section ends with some examples of reconstructive techniques which extend stereoscopic (or conventional) PIV into multiplane measurements. Finally, a separate section is dedicated to the Tomo-PIV technique, which is considered a “true” volumetric for flow velocity measurements. We will discuss the volumetric calibration procedure and the influence of experimental parameters on the quality of the measurement.

Chapter 2

The characterization of flow patterns in the LV may help the development and interpretation of flow-based parameters of cardiac function and (patho-) physiology. Yet, in vivo visualization of highly dynamic 3D flow patterns in an opaque and moving

chamber is a challenging task. This has been shown in several recent multidisciplinary studies where in vivo imaging methods are often complemented by in silico solutions, or by in vitro methods. Because of its distinctive features, PIV has been extensively used to investigate flow dynamics in the cardiovascular field. However, full volumetric PIV data in a dynamically changing geometry such as the LV remains extremely scarce, which justifies the present study. An investigation of the LV flow making use of a customized cardiovascular simulator is presented. It consists of a flexible membrane model of the LV with an idealized shape that is driven by a programmable piston pump. A multiplane scanning stereoscopic PIV setup is used, which allows for the measurement of independent planes across the measurement volume. Due to the accuracy in traversing the illumination and imaging systems, the present setup allows to reconstruct the flow in a 3D volume performing only one single calibration. The effects of the orientation of a prosthetic mitral valve in anatomical and anti-anatomical configurations have been investigated during the diastolic filling. The measurement is performed in a phase-locked manner, which allows to reduce the random measurement errors. The reconstructed 3D flow structures downstream the bileaflet mitral valve are shown and mean velocity components are presented, together with the vorticity and turbulent kinetic energy maps.

Chapter 3

To improve our understanding of intraventricular fluid mechanics and the impact of various types of prosthetic valves thereon, we have developed an improved custom-designed dynamic left ventricular phantom with an anatomically realistic shape. The shape has been extracted from a data set of computed tomography recordings of 150 patients. A biological, a tilting disc and a bileaflet valve (in two different orientations) were mounted in the mitral position and tested under the same settings. To investigate the 3D flow within the phantom, a four-view Tomo-PIV system has been set up with two cameras and a mirror splitter system. The results compare side-by-side the evolution of the 3D flow topology, vortical structures and kinetic energy in the LV during the cardiac cycle. Except for the tilting disc valve, all tested prosthetic valves induced a crossed flow path, where the outflow crosses the inflow path, passing under the mitral valve. An asymmetric jet was observed when the bileaflet valve is mounted in its anatomical configuration, while the jet remained nearly symmetric in the anti-anatomical orientation. The biological valve shows a strong jet with a peak velocity about twice as high compared to all mechanical heart valves, which makes it easier to penetrate deeply into the cavity. Accordingly, the peak kinetic energy in the LV in case of the biological valve is about four times higher than the mechanical heart valves. We conclude that the Tomo-PIV setup provides a useful ground truth measurement of flow

features and allows a comparison of the effects of different valve types on left ventricular flow patterns.

Chapter 4

In this study we describe high frame rate 4D echo-Particle Image Velocimetry (Echo-PIV) using a prototype matrix transesophageal transducer and a dynamic LV phantom for testing the accuracy of Echo-PIV in the presence of complex flow patterns. Optical time-resolved Tomo-PIV was used as a reference standard for comparison. EchoPIV and Tomo-PIV agreed on the general profile of the LV flow patterns but Echo-PIV smoothed-out the smaller flow structures. EchoPIV also underestimated the flow rates at greater imaging depths, where the PIV kernel size and transducer point-spread-function were large relative to the velocity gradients. We demonstrate that 4D Echo-PIV could be performed in just four heart cycles, which would require only a short breath-hold, providing promising results. However, methods for resolving high velocity gradients in regions of poor spatial resolution are required before clinical translation.

Chapter 5

4D flow MRI is a promising medical imaging technique that allows to picture the functional and anatomical information in a single exam. 4D flow MRI is an upgrade of phase-contrast MRI with flow velocity encoding in all spatial directions. It permits to measure the velocity vector field in a 3D domain and to estimate hemodynamic parameters. However, its mediocre space-time resolution and the consequences of long time scan lead to a loss of information, and the various pulse sequences have not been validated sufficiently, as stated in a recent *consensus* paper. This hampers the use of 4D flow MRI in clinical practice. However, only very few studies, mostly performed in simplified geometries have been conducted so far to compare 4D flow MRI measurements with other reference data. In this work, we have performed 4D flow MRI measurements with different accelerated pulse sequences (EPI, FFE and TFE) in our realistic LV model. Preliminary results of the comparison between the velocity vector field obtained with 4D flow MRI and Tomo-PIV are shown.

INTRODUCTION

Framework

The work presented in this PhD dissertation is framed within the multidisciplinary field of intracardiac flow visualization. In the last decade, we have experienced a growing interest in the study of the fluid dynamics within the left ventricle (LV), from a physiological, a clinical and an engineering point of view. Left ventricular flow dynamics is intrinsically complex, three-dimensional (3D) and unsteady. Its features are determined, inter alia, by the structure and function of the ventricular wall, the mitral and aortic valve apparatus and characteristics of inflow and outflow. The intraventricular flow field should therefore be susceptible to cardiovascular pathology and treatment, in particular to surgical interventions involving the valve repair or replacement.

Researchers from different areas are highly interested in narrowing the gap in our understanding of the global behaviour of the intraventricular flow and its potential impact on pumping efficiency and pathology progression. Their interest focuses on studying the correlation between hemodynamic events that have a strong fluid mechanical component on one hand and physiological and pathophysiological conditions on the other hand. Researchers are not only interested in developing diagnostic flow-based parameters that can be used by clinicians. Significant research efforts have also allocated to study for example: (i) the effects of different prosthetic heart valves on intraventricular flow dynamics (ii) the optimal setting of active medical devices (such as cardiac resynchronization therapy devices) that leads to favourable LV flow dynamics (iii) the dynamics of blood flow mixing in pathological LV geometries such as dilated cardiomyopathy.

These interdisciplinary studies rely on medical imaging methods, in vitro experiments using optical flow measurement techniques and/or computational fluid mechanics simulations. Still, visualizing such complex flow phenomena in an opaque and beating cavity is a challenging task. To date, in vivo imaging that are available in clinical practice are not able to accurately resolve the unsteady blood flow dynamics and picture the 3D flow field. Thus, new medical imaging techniques (such as echocardiographic PIV and 4D flow MRI) that allow to map the LV flow in a 2D or 3D domain are under-development.

Particle image velocimetry (PIV) techniques have been extensively applied in cardiovascular field, to investigate the flow dynamics near prosthetic heart valves, in vascular segments (aorta, aneurysms and cerebral arteries) and ventricular assist

devices. Until now, in vitro LV flow investigations were primarily performed in 2D or pseudo-3D, where the volumetric flow was reconstructed from a series of planar measurements. It is well agreed, however, that LV flow analyses would highly benefit from a volumetric measurement technique to capture the complex spatiotemporal behaviour of the LV flow.

The research objectives

The objectives of the PhD project are as follows:

- Develop an accurate, versatile and reproducibly controllable hydraulic setup that mimics as closely as possible the flow in a physical model of the LV, and that is compatible with PIV, MRI and ultrasound imaging;
- Implement advanced experimental PIV setup that allows to capture the 3D flow;
- Evaluate the effect of the different heart valve prostheses (in term of their geometries and orientations) on the 3D flow;
- Compare the 4D flow MRI and ultrasound techniques with reference velocity measurements in the LV model obtained with PIV.

To achieve the abovementioned goals and to overcome technical challenges, a first PIV setup was designed and developed at the bioMMeda-lab (UGent). Further, throughout the duration of the PhD project a broad collaboration was set up with various groups: Thoraxcenter of Erasmus Medical Centre, Transport Phenomena group of Delft University of Technology, Cardiovascular Magnetic Resonance group of Leiden University medical centre (The Netherlands) and German Aerospace Centre (Gottingen, Germany). These collaborations have allowed to interact with experts from different disciplines and to have access to the most advanced technologies in medical imaging, state-of-the art optical measurement equipment and data processing software. Therefore, we have jointly designed a second LV phantom that is more compact, MRI-compatible and that allows optical access for a multi-camera PIV technique and acoustically compatible with ultrasound imaging.

Dissertation outline

The thesis is divided into three major parts:

The first part consists of an introductory chapter with background information for the reader who is not familiar with LV physiology and the flow structures that form within

the LV cavity. A brief description of the flow visualization techniques that are available in clinical practice or under development is also provided. The second half of the chapter addresses PIV more in detail. It starts with a description of the working principles, calibration procedure and experimental parameters. Subsequently, more advanced PIV-based techniques such as stereoscopic and tomographic PIV (Tomo-PIV) are described.

The second part starts with the 2nd chapter that presents an experimental setup that allows volumetric reconstruction of the flow velocity field in an axisymmetric transparent LV membrane model. The setup permits to perform PIV measurements at different parallel planes without repeating the complex and time-consuming calibration needed for stereographic PIV.

The 3rd chapter describes a Tomo-PIV setup that has been implemented to picture the 3D flow structure in one single measurement. The measurements were performed in a more realistic LV model and the effect of different prosthetic heart valves on the LV flow is also shown.

The third part covers two comparison studies with medical imaging techniques. The 4th chapter presents a feasibility study for high-volume rate Echo-PIV (4D Echo-PIV). It describes the ultrasound data acquisition using a prototype transesophageal matrix array ultrasound transducer. Subsequently, it compares the Echo-PIV results and tomographic-PIV data, considered as the ground-truth technique. The 5th chapter describes a comparison between 4D flow MRI acquisition within the LV model and Tomo-PIV measurements.

The dissertation ends with a recapitulation of the most important findings and the perspective future works.

Contributions

In the following work, I have designed and implemented a novel stereoscopic PIV setup. I was closely involved in the design of the LV phantom, the implementation of the tomographic PIV setup and the data processing. In addition, I have participated in setting up the MRI measurement sessions. I have processed the velocity fields obtained with the 4D flow MRI and carried out the MRI vs PIV comparison analysis. The 3D Echo-PIV measurements and data processing were performed by J. Voorneveld. The MRI acquisitions and the data post-processing were conducted by Prof. J. Westenberg, Dr. Pieter van den Boogaard and Prof. H. van Assen. Finally, Dr. M. Novara has processed the PIV data using the Shake-The-Box technique.

List of A1 publications

H. Saaid, P. Segers, M. Novara, T. Claessens, and P. Verdonck, “Single calibration multiplane stereo-PIV : the effect of mitral valve orientation on three-dimensional flow in a left ventricle model,” *Exp. Fluids*, vol. 59, no. 3, pp. 1–13, 2018.

H. Saaid, J. Voorneveld, C. Schinkel, J. J. M. Westenberg, F. J. H. Gijsen, P. Segers, P. Verdonck, N. de Jong, J. G. Bosch, S. Kenjeres, and T. Claessens, “Tomographic PIV in a Model of the Left Ventricle: 3D Flow Past Biological and Mechanical Heart Valves,” *J. Biomech.*, vol. 90, pp. 40–49, 2019.

J. Voorneveld, **H. Saaid**, C. Schinkel, N. Radeljic, B. Lippe, F. J. H. Gijsen, A. F.W. van der Steen, N. de Jong, T. Claessens, H. J. Vos , S. Kenjeres and J. G. Bosch “4D Echo-Particle Image Velocimetry in a left ventricular phantom,” (Submitted for review to J. Ultrasound Med Biol)

Background

1.1 ANATOMY AND PHYSIOLOGY OF THE HEART

1.1.1 The heart as a pump

A normal adult heart beats about 100,000 times a day and pumps approximately 300 litres of blood in one hour. All this is accomplished with an organ as small as a fist, weighing less than 350 grams. The heart is the main component of the cardiovascular system and can be subdivided in a left heart and a right heart, which can be seen as two pulsatile pumps in series. Each side consists of two compartments: an atrium (upper chamber) and a ventricle (lower chamber) (**Figure 1.1**). The right atrium receives deoxygenated blood via the inferior and superior vena cava and coronary sinus (which collect the blood from coronary veins), and then passes to the right ventricle (RV). During the systole, the RV pumps blood towards the left and the right lung. Oxygen rich blood then returns to the left heart via pulmonary veins, passing first in the left atrium (LA). During the diastole the blood is sucked into the LV that will eject it into

the systemic circulation during systole.

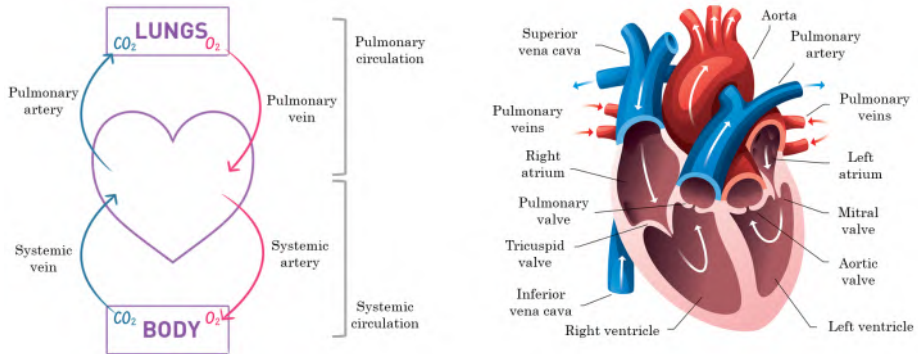


Figure 1-1: *Left:* sketch of the cardiovascular system. *Right:* Schematic diagram of the four chambers with respective valves, arteries and veins. (Adapted from qcg.com.au)

The blood enters and leaves the ventricle compartments across flexible valves that have the role to open efficiently or to attain perfect closure. There are four valves in the heart that we can group in atrioventricular valves (mitral and tricuspid) and semilunar valves (pulmonary and aortic) (**Figure 1.2**). The first ones separate the atria from the ventricles and the second type separate the ventricles from the big vessels (aorta and pulmonary artery). The atrioventricular valves consist of little flaps (cusps) that are connected to papillary muscles via chordae tendineae. These tiny structures help preventing regurgitation by keep the valve in a taut position when the heart contracts. Conversely, the semilunar valves are more symmetrical and are not attached to chordae tendineae (**Figure 1.2**).

The shape of the heart is somewhat conical, broad at the base (superior surface) and reducing to the apex. Although both ventricles pump the same amount of blood, the muscle of the LV is more developed and thicker (approximately 3 times thicker) than the RV (**Figure 1.2**), in order to overcome the high resistance necessary to pump blood into the systemic circulation.

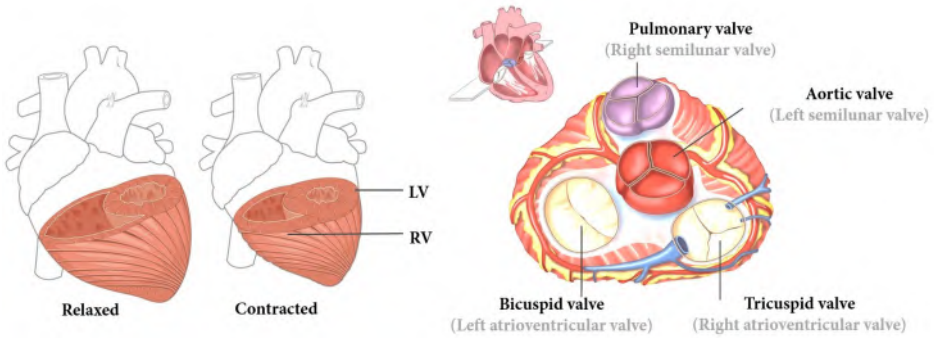


Figure 1-2: Left: Differences in ventricular wall thickness. Right: Structures of the heart valves. (Adapted from uptodate.com and biology-forums.com)

1.1.2 Pressure and flow

The cardiac cycle is typically divided into diastolic (filling) and systolic (ejection) phase, during which a sequence of complex electrical and mechanical events take place, with resulting changes in pressure and flow in the heart (**Figure 1-3**).

The filling phase starts when the ventricular pressure drops below the atrial pressure and the mitral valve opens (MVO), which allows the blood to flow into the LV. At the onset of the diastole, the filling process is passive due to ventricular relaxation (early filling). It is followed by a second, late filling, caused by an extra push due to the atrial contraction. The ventricle is fully relaxed at the end of the diastole and the respective volume is called the end-diastolic volume (EDV) (approximately 120 ml). Next, the mitral valve closes and the ventricle starts contracting. Since both aortic and mitral valve are closed, the blood volume in the LV remains constant, but pressure increases rapidly (iso-volumetric contraction). When the LV reaches a pressure around 75 mmHg (systemic diastolic blood pressure DBP) the aortic valve is forced to open (AVO) allowing the ejection of the blood through the whole arterial system. During this phase both ventricular and aortic pressure continue to increase until a peak of 120 mmHg (systolic blood pressure SBP) is reached. The residual blood volume at the end of the ventricular contraction, usually about 50 ml, is called the end-systolic volume (ESV).

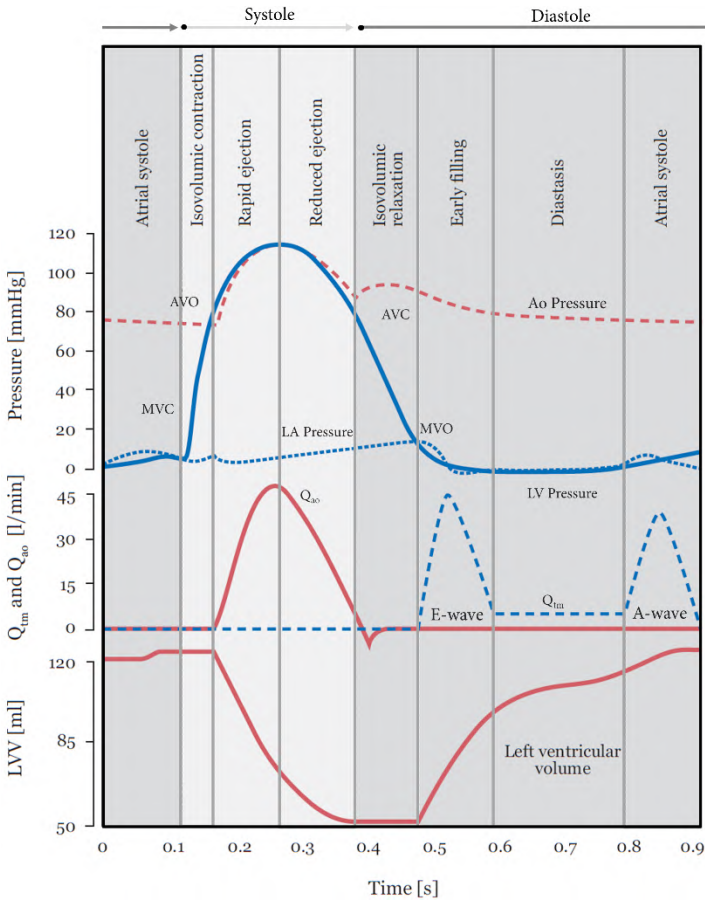


Figure 1-3: Temporal sequence of various events in the cardiac cycle. Abbreviations: **AVC** and **AVO**: Aortic valve closure and opening, **MVC** and **MVO**: mitral valve closure and opening. **ESV**: end-systolic volume. **EDV**: end-diastolic volume. Q_{tm} : Transmittal blood flow rate. Q_{ao} : Aortic blood flow rate. **LVV**: left ventricle volume (adapted from [1]).

The difference between the EDV and ESV, the stroke volume (SV), is the amount of blood that the LV ejects per heartbeat (around 70 ml). In physiological conditions at least half of the blood volume in the LV is ejected during each heartbeat. In other words, the ejection fraction (EF), defined as the SV divided by the EDV should be higher than 50%. The cardiac output is the volume of blood ejecting to the pulmonary or systemic circulation multiplied by the heart rate (approximately 4.9 L/min, considering a SV of 70 ml and a heart rate of 70 beats/min). Further, the aortic pressure exceeds the pressure in the LV marking the end of the systolic phase: the aortic valve (AVC) closes and the ventricle muscle starts to relax and ventricular pressure falls sharply during the

isovolumic relaxation period. This phase is ended when atrial exceeds ventricular pressure and the mitral valve opens again.

The pressure-volume loop (**Figure 1-4**) is derived from the LV pressure and volume curves shown in **Figure 1-3**. The area within that loop represents the LV work and is a useful tool to assess ventricular function since it provides the link between different cardiac events and hemodynamic parameters. However, it does not provide any information on the local flow structures in the LV. Additionally, the pressure-volume loop is obtained via cardiac catheterization which is a complex and invasive technique. Cardiac catheterization requires insertion of multisensory-catheter in the heart cavity and arteries using an angiography technique. Cardiac catheterization provides instantaneous pressure-volume waveforms by using multiple sensors to measure: (i) the time varying conductance drop (of the blood) between two points of the inserted catheters and (ii) intraventricular pressure. Despite its invasive approach and complexity, it is still considered the gold standard in hemodynamic for LV assessments and for patient with sever stenosis or congenital heart diseases.

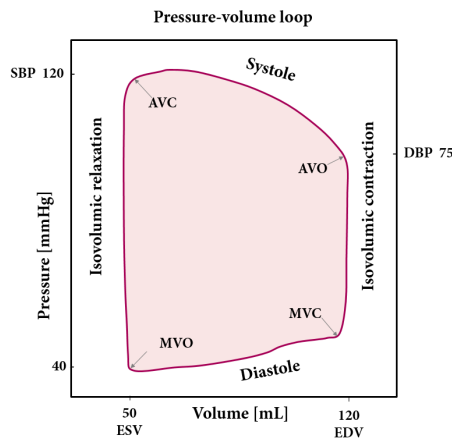


Figure 1-4: Left: Pressure-Volume loop. **SBP** and **DBP**: systemic systolic and diastolic blood pressure. (adopted from [2]).

1.1.3 Multidisciplinary approach to study cardiac flow dynamics

All knowledge on the properties of the blood flow inside the heart chambers is the result of intense collaborations between clinicians, engineers and physicists. Their multidisciplinary approach has drastically improved our understanding of the LV flow dynamics in recent years. The following paragraph attempts to summarize the

contribution and/or points of view of those who are involved in this relatively new research discipline.

Clinical point of view: Clinicians consider studying local flow and pressure within the LV chamber may help in understanding the pathophysiology of heart diseases and evaluate the cardiac performance before and after interventions such as valve repair or replacement. With the hypothesis that abnormal LV flow dynamics may initiate and modulate LV remodelling, the assessment of LV flow may provide diagnostic tools for early stratification of patients. Clinical researchers are interested to overcome the limitations of the current tools (such as cardiac catheterization and Doppler-based techniques) for LV flow dynamics assessment.

The mapping and quantification of flow-related information remains a challenging task due to difficulties in resolving the highly unsteady velocity field in 3 spatial directions in an opaque and beating cavity. In clinical practice, cardiac performance is evaluated by measuring the blood velocity through valve and/or tracking the wall displacement and deformation. Technological advancements give the opportunity to explore more details and analyse intracardiac flow distribution in order to study its potential clinical implications. Thus, the development and improvement of emerging medical imaging techniques such as echocardiographic PIV (Echo-PIV), Flow vector mapping (FVM) and advanced MRI-based methods such as 4D flow MRI was possible owing to strong collaborations between clinical researchers, companies and engineers. *Clarification:* The term “4D” (3D+time) is more used in medical imaging world when a technique is able to image the 3D anatomy (or phenomena) over a certain time. Instead, in engineering world the term 3D is more adopted also for time resolved techniques. In the following sections (1.1.5) we will discuss the available tools to assess LV flow and the emerging medical techniques.

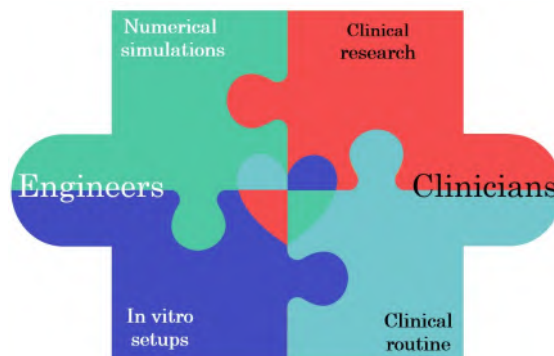


Figure 1-5: Schematic overview of the different scientists that are interested in studying LV flow.

Our current knowledge on quantitative LV flow does not only result from medical imaging, but also from the interplay between numerical simulations and experimental methods. In vivo imaging methods are still limited in terms of temporal and/or spatial resolution and are often complemented and/or validated with in silico methods, where the flow within the patient-specific LV is simulated numerically, or by in vitro methods (Figure 1-6).

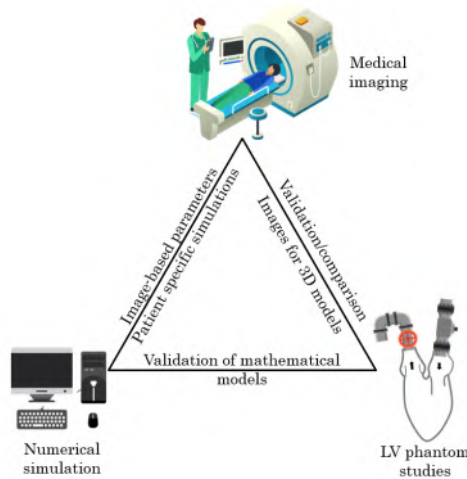


Figure 1-6: Schematic representation of the interplay between numerical simulations, experimental investigations and medical imaging.

Engineers’ and physicists’ contribution: Many engineers focus on solving the complex governing equations for the fluid (blood) and structural (tissue) domain via numerical simulations, with the ultimate goal to model the whole LV system (including fluid, valves, LV wall and papillary muscles) as a fluid-tissue dynamic system. Such simulations are performed to explore for example the LV flow dynamics in different physio- and pathological conditions or to help surgical planning in a specific patient model/geometry (e.g. patient specific surgical planning).

Fluid dynamics experimentalists are traditionally interested in implementing sophisticated hydrodynamic setups combined with flow visualization tools to evaluate for example the effects of different artificial valves or ventricular assist devices on the LV flow dynamic, or comparing experimentally obtained data with numerical simulation results. They are also involved in developing compact and radiologically-compatible phantoms used to validate medical imaging techniques. In the next section we recount of one of the first Engineers that unified between engineering and medicine. He discovered two more chambers of the heart, provided detailed sketches of the heart and valve anatomy and performed hemodynamic flow visualization experiments.

1.1.4 LV flow visualisation 500 years ago

Leonardo Da Vinci (1452-1519) is best known for his paintings, inventions and sophisticated human anatomy sketches. He combined words and drawings to convey functional anatomical information, but considered illustrations a form of expression superior to writing because of its effectiveness. One of the advantages over his contemporary anatomists, is that Leonardo was also an engineer and artist with more intuitive understanding of forms.

Leonardo investigated several aspects of cardiovascular anatomy and physiology. For example, to study the role of the Sinus of Valsalva in the closure dynamics of the aortic valve, he carried out an in vitro hemodynamic experiment on an ox's heart. He injected mottling wax in the LV outflow tract and made a glass model from it. Consequently, he connected the glass model to a pump and added small seeds to the fluid to be able to visualise the trajectories (patterns) of the flow inside the glass model. Leonardo described how the flow passes from the low ventricle (left ventricle) to the aorta and he noticed that the jet in the centre is stronger than the flow closer to the cusps of the valve (no-slip condition). Leonardo correlated the formation of eddies in the Sinus of Valsalva with the shear layer fluid-valve (**Figure 1.6**). Further, he identified the vortex formation in the Sinus as a flow phenomenon that plays an active role in the valve's closure.

This flow experiment conducted by Leonardo may be considered as one of the earliest qualitative PIV experiments. As in Leonardo's experiment, many researchers nowadays combine optical velocity measurement techniques and transparent models to investigate flow dynamics in complex geometries. In the subsequent section we provide a brief description of the currently available modalities used in research and/or in clinical practice to characterize the intracardiac flow field.




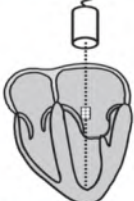
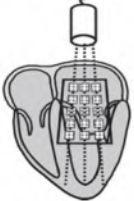
Figure 1-7: Bottom left: Sketch of the outline of the mold of the LV outflow tract. On the right, Leonardo shows vortices in the sinus of Valsalva. (Courtesy of: The Royal Collection - 2002, Her Majesty Queen Elizabeth II)

1.1.5 LV flow visualisation techniques

Medical imaging. The most used imaging techniques to evaluate flows inside the LV are ultrasound and magnetic imaging-based.

Echocardiography is the most used ultrasound based bedside technique for assessment of flows inside the LV. It is based on the Doppler principle which relates the frequency of a wave to the relative speed of the source and the observer. In echocardiography a series of pulses is transmitted by a transducer to detect flowing blood. The reflected echoes by moving blood have different frequencies, whose value is proportional to the blood velocity towards or away from the transducer (observer). The difference between the emitted and the received frequency is called Doppler shift or frequency shift. **Table 1**, shows different Doppler-shift-based methods that allow qualitative and quantitative blood flow assessment. The briefly summarized ultrasound-based techniques are the most used tools for LV flow assessment in clinical routine (in combination with cardiac catheterization). However, the above-mentioned techniques measure only the axial velocity along the line of each ultrasonic beam.

Table 1-1: Schematic overview of the Doppler modes measuring blood flow velocity (Adapted from [3])

Continuous Wave Doppler (CW Doppler)	Pulsed Wave Doppler (PW Doppler)	Color Flow Doppler (CF Doppler)
		
<p>Along a single beam, continuous sending and receiving of ultrasound takes place. All Doppler shifts recorded along the scan line are displayed against time in the CW Doppler spectral display</p>	<p>In a defined sample volume, the size and the location of which can be adjusted, velocity are measured by sending and receiving a short ultrasound pulse. Doppler shifts recorded are displayed against time in the PW Doppler spectral display</p>	<p>In many sample volumes (by size and location) selectable CF Doppler area velocities are measured by sending and receiving short ultrasound pulses. Mean Doppler shifts recorded are displayed in color superimposed on the 2D image</p>
<p>No limitations in measuring high velocities</p>	<p>Only low velocities can be measured</p>	<p>Only low velocities correctly detected</p>
<p>Location of velocity can not be determined</p>	<p>Precise measurement at a defined location</p>	<p>Precise measurements at defined locations</p>

Therefore, technological advancements, along with the increased interest in intracardiac flow drove the development of new ultrasound methods for 2D flow mapping, such as Vector Flow Mapping (VFM) [4] and echocardiography-PIV (Echo-PIV) [5], [6]. VFM is based on color Doppler application developed to extract velocities perpendicular to the beam direction. VFM assumes laminar flow and that through-plane flow component is negligible. VFM combines the measured (axial) velocity and the estimated (radial) to provide 2D velocity maps. A further development of VFM combines color Doppler data with ultrasound speckle tracking to extract the radial velocity component. The second ultrasound-based modality, Echo-PIV, applies Particle Image Velocimetry (PIV) methods on B-Mode images. The ultrasound images are obtained by injecting small contrast agent (microbubbles). Echo-PIV allows visualization of blood flow patterns and vortices in 2D velocity map, by tracking the in-plane displacement of a group of contrast agent particles between two consecutive frames.

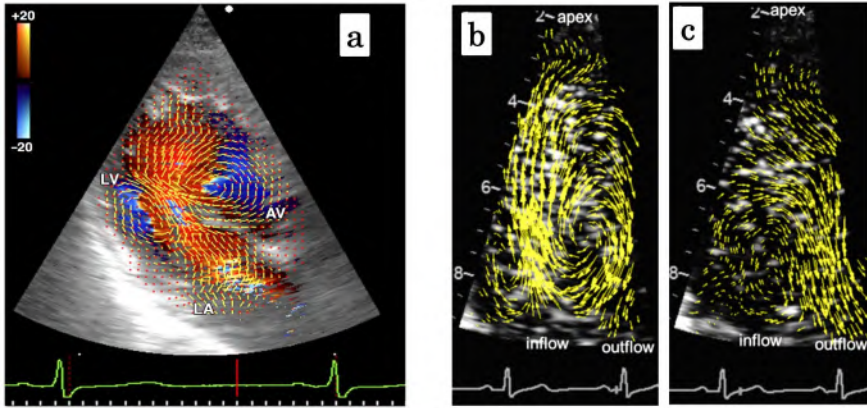


Figure 1-8: *left:* VFM velocity and vorticity map by using cross-sectional image obtained by bi-mode color Doppler and speckle tracking information (Image courtesy of Tokuhsa Uejima, Cardiovascular Institute, Tokyo, Japan). *Right:* Echo-PIV, velocity vector maps at early diastole and ejection phase (adopted from [7]).

Phase-contrast magnetic resonance imaging (PC-MRI) is a promising technique that measures the blood flow velocity in any direction without using contrast agents. In PC-MRI the magnitude of the radiofrequency signal is used to reconstruct anatomical images. The phase information is affected (proportionally) by the blood motion and is used to extract the blood flow velocity. In PC-MRI moving spins under bipolar gradients have net phase shift proportional to their velocity. Instead stationary spins experience no net phase shift. So, by measuring the changes in phase, flow velocity can be computed. By applying bipolar gradients along the spatial directions and measuring phase changes, flow velocity components along each encoding direction can be computed. The degree of sensitivity to slow or fast flow is determined by the amplitude, duration and spacing of the bipolar gradients.

The 2D flow velocity-encoding is the most used MRI-based technique for flow visualization and assessment and it is integrated in clinical routine. The blood flow motion can be measured along flexibly encoding directions. The MRI acquisition is synchronized with the cardiac cycle using the electrocardiogram (ECG) signal, which allows to explore the velocity over the cardiac cycle. When velocity encoding is used in the three-spatial directions (known as 4D flow MRI method) and ECG gating (triggering) are used, the result is a complete velocity (three components) field at several time points over one cardiac cycle. One peculiarity of 4D flow MRI is providing a complete scenario of the region of interest by allowing retrospective visualization and analysis of the anatomical structure and temporal evolution of the blood flow field in the volume of interest. Additionally, 4D flow MRI allows estimation of advanced hemodynamic quantities such as turbulent kinetic energy, wall shear stress and

pressure gradients [8].

The listed ultrasound and MRI imaging techniques have various advantages and disadvantages that are listed in **Table 2**.

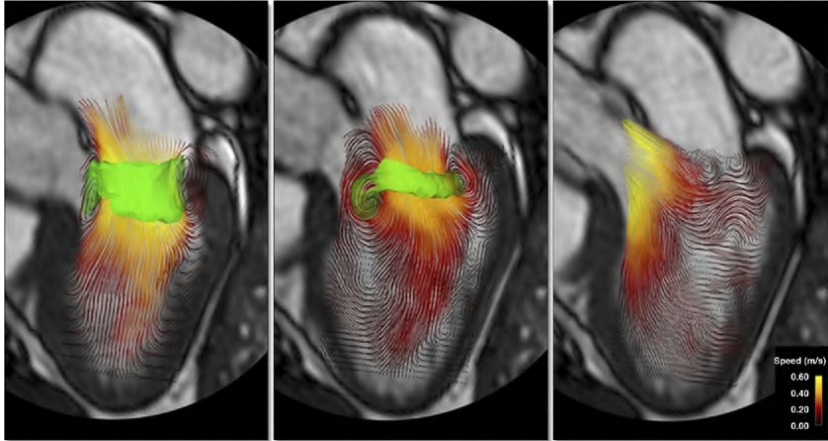


Figure 1-9: LV displayed in a 3-chambers view with streamlines color encoded with velocity magnitude, (a) early diastole, (b) late diastole, and (c) ejection phases of the cardiac cycle. For vortex visualization an isosurface is shown in green in early and late diastole (Adapted from [9]).

Table 1-2: Summary of technical characteristics, limitations and advantages of flow-visualization modalities (Snapshot from [9])

	Phase-Encoded MRI	Echocardiography	
		Echo-PIV	Color Doppler
Resolution and coverage relative to all 3D of space	Good spatial resolution in all 3D or in 2D in shorter acquisition times; unrestricted access	Good spatial resolution in 2D planes, and in multiple planes if required	High spatial resolution in 2D; good resolution in 3D
Coverage relative to all 3-directional components of velocity	All 3 can be acquired, or 2, or 1, through a plane placed in any orientation	Both in-plane components represented but not the through-plane	Only the 1 component directed to or from the transducer is currently measurable clinically
Temporal resolution	Typically 20–50 ms, each phase is calculated from acquisition over many heart cycles	High temporal resolution (4–20 ms), allows assessment of velocity fields even during brief isovolumic contraction and relaxation phases over few heartbeats	Good temporal resolution in 2D (4–20 ms), relatively low in 3D
Scan time	Long (5–20 min) for a dataset covering all 3D and all 3-directional components but seldom real-time	Both scan time and offline analysis can be done over few heartbeats in minutes	Rapid scan times, real-time visualization
Breath-holding	Breath-hold used for short, unidirectional velocity acquisitions, or diaphragm navigation for long acquisitions during free breathing	Imaging relatively easier during breath-hold but also possible during respiration	Not required
Low-velocity accuracy	Low velocities are measurable but less accurate if high velocities also have to be measured	Well-visualized	May be underestimated or affected by noise
High-velocity accuracy	Measurable up to the chosen VENC limit, but only where a stream or jet core is wide enough to include whole voxels	May be underestimated	Well-resolved within aliasing limit
Applications	Flow visualization and measurement of volume flow through all cardiac chambers and large vessels	Flow visualization through all cardiac chambers, aortic flow evaluation may require use of transesophageal echocardiography	
Implanted devices	Metal stents or valve rings cause local artifact; most pacemakers rule out MRI	Flow can be visualized through implanted cardiac devices, and in the presence of pacemakers and defibrillators	

2D = 2-dimensions; 3D = 3-dimensions; Echo-PIV = echocardiography particle imaging velocimetry; MRI = magnetic resonance imaging; VENC = velocity encoding.

Numerical simulations (or computational fluid dynamics CFD) is based on defining an idealization of the phenomena by a mathematical model based on physical equations. The conservation of mass equation and the conservation of momentum equation (Navier-Stokes equation) describe the motion of a fluid by relating spatiotemporal derivatives of physical variables. Basically, the Navier Stokes equation is an extension of Newton's second law for viscous flow. Additionally, the dynamics of a flow depends on its interaction with the environment, which is mathematically prescribed by the type of boundary conditions needed to solve the governing equations. The numerical solution of these mathematical equations is described by partial differential equations. The most used numerical approaches to solve these equation are: the finite-difference method, finite-volume and finite-element method [10]. The differences between these methods is how the flow domain is discretised (grid points or small control volumes) and how the set of flow-governing equations is solved (as algebraic or differential equations). Additionally, the fluid and structural governing equations can be solved simultaneously at each step or separately and then merged iteratively.

Numerical simulations of the flow inside cardiac chambers are a complementary approach to unveil LV fluid dynamics that may not be easy to access with in vivo imaging. CFD has the advantage to relative easily study the effect of different scenarios (flow and geometry related parameter), such as surgical procedures, (patho-) physiological conditions, and development of cardiovascular devices. However, computational modelling of the flow inside LV requires sophisticated numerical models and powerful computational resources. Nowadays, numerical simulations attempt to couple fluid and structural media by solving complex equations. Additionally, the LV structures contains different elements that may affect the flow dynamic scenario (heart valves, cardiac wall, chordae tendineae and papillary muscles). The interaction of blood flow with these structures gives rise to several challenges in computational modelling which are modelled as dynamic boundaries. For example, the immersed boundary method takes into account the "active" dynamic behaviour of the tissue elements and their interaction with blood. Numerical studies have been conducted in simplified geometries (axial symmetric) to understand the general flow patterns [11][12][13], the formation of vortical structures [14] or more complex patient-specific cases by integrating data from medical imaging and measurements, with a more clinically orientated perspective.

An extended explanation on the numerical simulation of the flow dynamics inside the LV is provided in extended review papers [15], [16] and book chapters ([17] and [10])

Optical flow measurements techniques require hydraulic setups to physically mimic the flow in an organ or in the vicinity of a medical device. Such experimental setups are

normally equipped with pressure and flow sensors to monitor the hydrodynamic conditions, and more advanced velocity measurement tools such as PIV techniques and laser Doppler anemometry, and additional camera systems to register the motion of moving structures (such as the wall of the LV or the leaflets of the valves).

The PIV method relates **particle** displacement over a short time interval between two consecutive **images** to **measure** the **velocity** of the fluid under investigation. The measurements are performed within transparent LV membrane with a shape that is either based on medical images or an idealized geometry. Because of its distinctive features, such as non-invasivity, high accuracy and its ability to provide whole-field information with an excellent spatial-temporal resolution, PIV is recognized as a gold standard technique for fluid velocity measurements. Section 1.2 provides a detailed explanation on its working principles and highlights the relevant experimental parameters of planar and volumetric PIV techniques.

1.1.6 The role of LV flow

The LV is the component that links between low- and high-pressure systems of the cardiovascular circulation. During diastole, the LV works as part of the low-pressure system, while it operates as a part of the high-pressure system during the systole. The periodic contraction and relaxation of the LV generates hemodynamic work needed to pump blood.

Figure 1.10 illustrates the temporal evolution of the flow patterns inside the LV cavity in a healthy subject. The illustration is a result of various *in vivo* and *in vitro* studies, for a more detailed review of LV flow dynamics, the reader is referred to the following books (chapter 7 [17] and chapter 3 of [7]) and manuscripts [2], [18].

During iso-volumetric relaxation the ventricle chamber geometry becomes more spherical. At the same time, the mitral valve (MV) cusps move towards the apical direction leading to a blood displacement into the LV before the MV starts to open (before leaflet separation). When the atrial pressure exceeds the ventricular pressure, the mitral valve opens forming a conical canal with its cusps and marking the onset of the filling phase. The inflow stream in contact with the valve cusps develops a shear layer due to the velocity difference between blood and leaflet. The shear layer is transported inside the LV and starts rolling-up into an asymmetrical vortex-ring. The transmitral jet hits the septal and the lateral wall and interacts with the (end systolic) blood volume already within the LV. The vortex-ring becomes wider behind the posterolateral leaflet while its inferolateral part gradually decays until it disappears. The blood stream travels away from the mitral valve forming a large toroidal structure, often referred to as a “vortex-ring”, towards the apex until it pinches off.

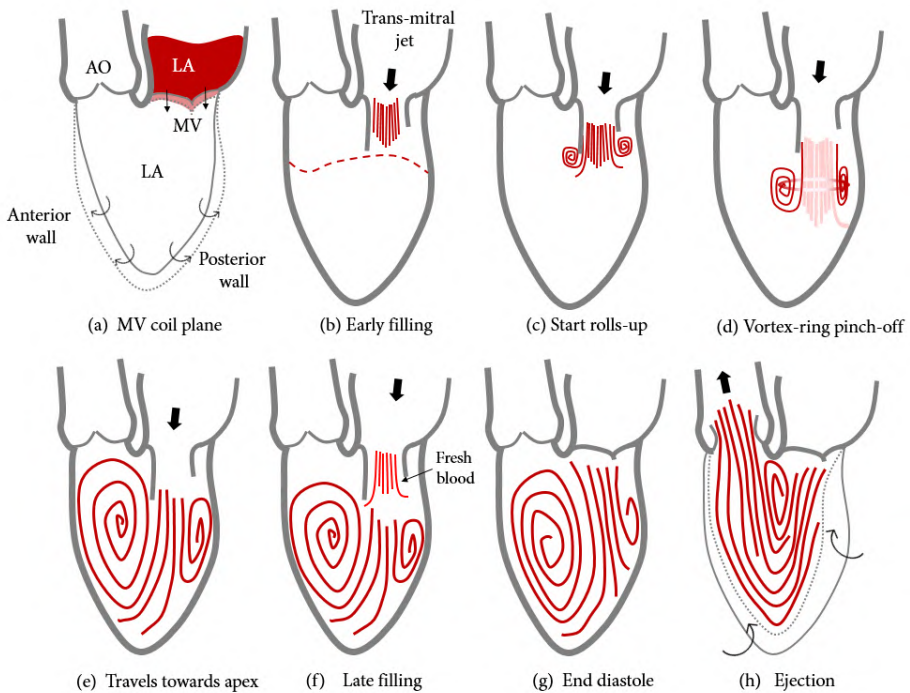


Figure 1-10: Sketches of intraventricular flow structures during one cardiac cycle.

The vortical structures inside the heart were first documented by Taylor and Wade (1970 and 1973) in dogs and sheep. The flow visualization was performed by injecting contrast agent and using cine-angiography and endoscopic intracardiac cine-photography to record the flow. Their primary goal was to determine whether the flow in the heart is laminar or turbulent. They have observed formation of vortex close to the mitral valve and its evolution during the ventricular filling. The presence of swirling flow inside the heart cavity was also shown in different experimental studies, performed by Bellhouse 1969, 1972 and Reul 1981 [13][14]. Another pioneer work was published in 1988 by Beppu and co-workers [21] performing one of the first contrast and pulsed-Doppler echocardiography. In this case the flow visualization was possible using contrast agent (saline agitated with carbon dioxide) and ultrasound to assess flow in healthy and ischemic dogs' hearts and they describe the differences in terms of flow pattern between the two groups.

Further in time, with technological advancements in medical imaging tools, Walker et al 1993 performed one of the earliest studies on 2D velocity vector map using MR imaging. Kim and his colleagues have confirmed the presence of vortices adopting color Doppler mapping [22] in pig models and an MR imaging [23] in healthy subjects. In a

MRI study, Kilner et al [24] postulated that the peculiar vortical flow that forms during the filling phase has an active role. They suggested that the asymmetric vortical motions preserve the kinetic energy of the entering blood, which would reduce the workload needed for reacceleration of the blood during ejection. Additionally, it has been suggested that the formation of the vortex may increase the mass transport from LA to LV by channelling the inflow blood stream, which may facilitate early filling [25], [26]. This mechanism depends on whether the vortex remains attached to inflow jet, pinches off or breaks down.

LV filling is a rich flow dynamic event, known to be an unsteady and 3D phenomenon, with straight flow at the onset of the filling phase and formation of swirling structures. As we described above, the formation of vortical flow patterns keeps the incoming fresh blood in motion throughout diastole and redirects it towards the outflow tract for ejection. Therefore, filling and ejection phase are not to be considered as separate events. The flow dynamic behaviour of the blood flow inside the LV is influenced by several factors: change in chamber volume and shape, wall motion and structure, valve performance and timing intervals (electric activity).

The LV flow has been widely investigated with different tools to understand the dynamics of the interaction of the LV with its flow diastolic patterns in physiological and pathological conditions, aiming to comprehend the slow transition from gradual adaptive changes into pathology. However, even in some healthy subjects, the described diastolic vortex formation during the E-wave and A-wave does not occur [27]. In dilated cardiomyopathy patients the vortex ring induced at early filling lasts longer and the anteroseptal vortex component (that decay in healthy case) continues growing during the diastasis. This behaviour may be due the remodelled geometry (spherical shape) of the ventricle. The temporal evolution of the intraventricular diastolic patterns is not only affected by the geometrical changes but also by the timing intervals of the cardiac cycle, such as in the presence of tachycardia (Benito 2012). An overview of the most recent works on LV fluid dynamics (especially in vitro studies) will be provided in the introduction sections of the second and third chapters (paragraphs 2.1 and 3.1).

1.2 PARTICLE IMAGE VELOCIMETRY

PIV is a well-established non-invasive optical technique for flow visualization and quantification [28], [29]. PIV-based techniques have been used to solve fluid dynamic problems in a wide range of domains, such as aircraft, naval and biomedical engineering. The advantage of PIV with respect to point-wise velocity measurement techniques (such as laser Doppler anemometry) is that PIV can estimate instantaneous velocity in the whole field of interest.

Considering that there is no true standardization of the nomenclature of PIV-based

techniques we propose the following terminology, based on dimensional size of data (number of velocity components and number of spatial dimensions) that are covered (**Figure 1.11**). For example, the conventional PIV (2C-2D PIV) resolves the two velocity components (2C) in one plane (2D). Note that conventional PIV (and also stereoscopic PIV) are also often referred to as planar PIV techniques. Additionally, in case of periodic flows, PIV measurement can be performed in two different manners: (i) Time-resolved (high-speed) or (ii) phase-locked (phase_averaging). In the first case, particle images are acquired at several time points in one cardiac cycle (Time-resolved). The alternative is to acquire data at one specific time point over several repeatable cycles and then to ensemble-average the data (phase-averaging) (**Figure 1.12**).

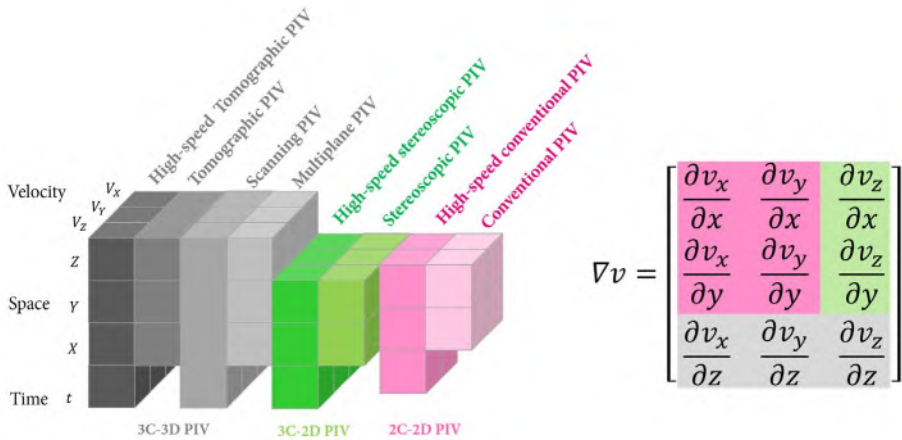


Figure 1-11: PIV techniques are labelled based on the number of velocity components measured and whether a measurement is performed in a single plane or in the whole domain. ‘Time’ indicates if a measurement yields velocity files at a single time instant or a complete sequence.

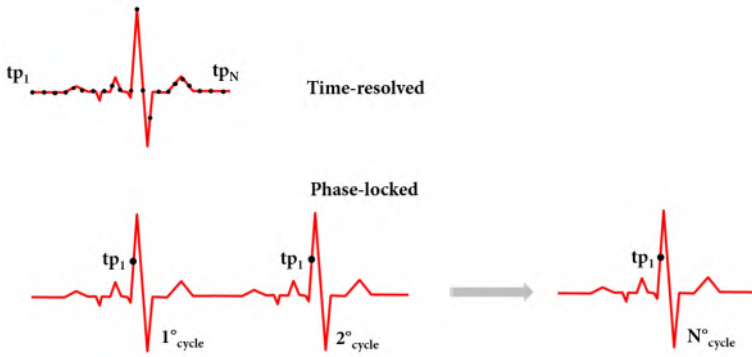


Figure 1-12: Illustration of difference between time resolved and phase-locked acquisition.

1.2.1 2C-2D PIV

PIV relies on fundamental quantities (displacement and time) to derive **indirectly** the velocity $\mathbf{U}(\mathbf{x}, t)$ of the fluid by estimating the displacement ($\Delta\mathbf{x}$) of the particles in the medium over a certain time (Δt). Additionally, PIV does not count on the displacement of a single particle but of a group of particles. Since the number of particles per unit area is large, it is not feasible to measure displacements by tracking individual particles (as in particle tracking techniques).

Figure 1.13 shows a typical PIV setup, which consists of a powerful laser beam shaped into a sheet of light that illuminates the particles in the region of interest. A digital camera (high-speed if needed) is placed perpendicular to the laser sheet so that its in-focus object plane coincides with the illuminated slice. The illuminated particles scatter into a photographic lens and the camera freezes the particle image at two or more frames. Subsequently, the images are transferred to a computer for further processing.

1.2.2 Seeding

The choice of the seeding is a fundamental step in obtaining accurate measurements. Ideally, the introduced particles are neutrally buoyant with respect to the fluid medium and thus faithfully follow the flow dynamics. In practice, one way to evaluate the ability of a particle to follow the flow is to estimate the settling velocity (U_∞) of the particle under gravity. Particles are considered suitable if U_∞ is negligible compared to the actual flow velocities.

$$U_\infty = \frac{gd_p^2(\rho_p - \rho_f)}{18\mu}$$

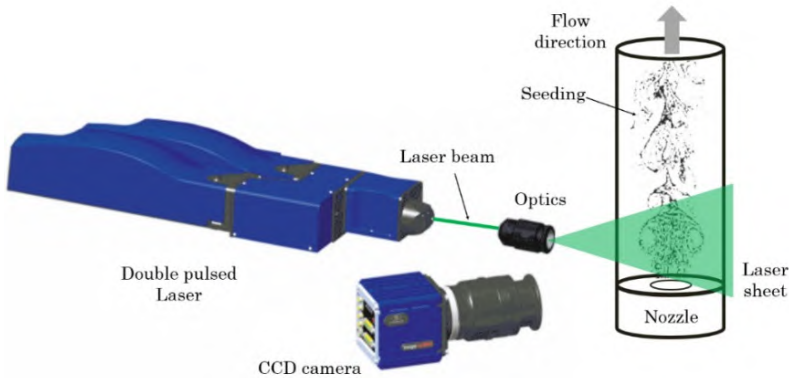


Figure 1-13: Schematic sketch of experimental setup. It comprises a pulsed light source collimated in a light sheet, flow circuit, digital camera and seeding (Adapted from LaVision poster).

Where g is the gravitational acceleration, d_p and ρ_p are the particle diameter and density, and ρ_f and μ are the fluid density and dynamic viscosity. An alternative way to assess the discrepancies between fluid dynamic and particle motion is to evaluate the relaxation time (in a continuously accelerating fluid).

For liquid flow applications, the particle choice is more easily achievable compared to air flows where the density ratio is typically $\rho_p/\rho_f = \mathbf{O}(10^3)$. The most commonly used seeding particles for experiments in liquids are polystyrene, aluminium, glass or synthetic material. The size ranges from a few μm to hundreds of μm .

Choosing a good particle size is more effective and economical than choosing a more sensitive camera or increasing the laser power to increasing the signal-to-noise ratio of the particle images. The size of the particles is a compromise between the ability to fulfil the fluid-mechanical requirements (using small particles) and the need to diffuse sufficient light (with large particles) in order to be visible.

In cardiovascular flow experiments the investigated model/region is typically enclosed in a complex geometry. Consequently, in order to avoid reflections that reduce the quality of the measurement, fluorescent particles are used as tracer. For example, in case of a Nd: YAG laser (532 nm) illuminating Rhodamine-B coated particles scatter the laser light at 550-680 nm. Thus, by using an appropriate optical filter it is possible to separate the wavelength of the incident light from the re-emitted fluorescent light.

1.2.3 Illumination

Laser light is widely adopted in PIV-based techniques because of its ability to generate monochromatic light with high density and short pulse length. The intensity of the

illumination source affects the intensity of the backscattered light and dimensions of the region that can be investigated. The most common light sources are semiconductor lasers such as Nd:YAG (neodymium-doped yttrium aluminum garnet) and Nd:YLF (Neodymium-doped yttrium lithium fluoride). This latter produces the highest pulse energy and average power, with repetition rates up to approximately 10 kHz and as such is mostly used in high-speed PIV setups.

Most frequently used lasers in PIV operate at a fundamental wavelength of $\lambda = 1064$ nm or 1053 nm in case of Nd:YAG and Nd:YLF, respectively. As it is advantageous to work with visible light, the fundamental wavelength is turned in the visible range (approximately 526 nm) by frequency doublers. Usually, the laser for PIV application has a double cavity to generate two separate beams with equal intensity in a short time interval. In a planar PIV arrangement, the laser beam is shaped into a thin light sheet using a compound of spherical and cylindrical lenses placed between the light source and the measurement section (**Figure 1.14**).

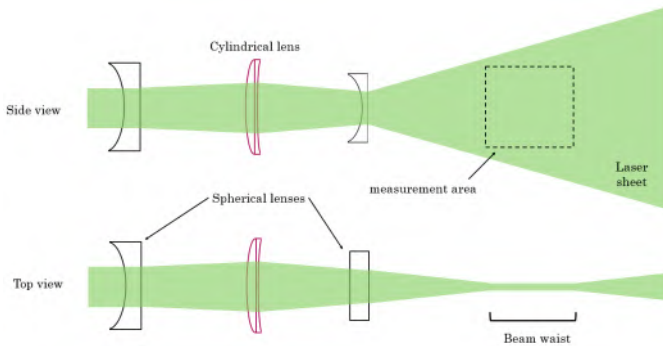


Figure 1-14: Light sheet formation with two spherical lenses and one cylindrical lens.

1.2.4 Imaging and processing

Nowadays, the particle images are recorded with digital cameras with CCD (Charge Coupled Device) or CMOS (Complementary Metal-Oxide Semiconductor) sensors. For imaging purposes, the particle image diameter should be small in order to minimize the uncertainty in the displacement. Contrarily, small particle image can lead to a bias effect towards integer pixel values, called in literature as peak-locking [30]. The particle image diameter depends on the particle size and lens parameters (focal length and aperture diameter).

The recorded images are divided in small areas called interrogation window. Subsequently, a velocity vector is determined for each interrogation window by using statistical methods (cross-correlation in case of multi-frame/single exposure (the

images are singly exposed) [31]) (**Figure 1.15**). The two velocity components (V_x, V_y) in the object plane are estimated from the measurements of the particle image displacements ($\Delta x, \Delta y$) in the recorded image according to relation (1),

$$\begin{pmatrix} V_x \\ V_y \end{pmatrix} = \frac{M_0}{\Delta t} \begin{pmatrix} \Delta x \\ \Delta y \end{pmatrix} \quad (1)$$

Δt is the time separation between the two frames and M_0 is the magnification factor, defined as the ratio of the lens-sensor distance z_0 and the lens-object distance Z_0 (**Figure 1.15a**).

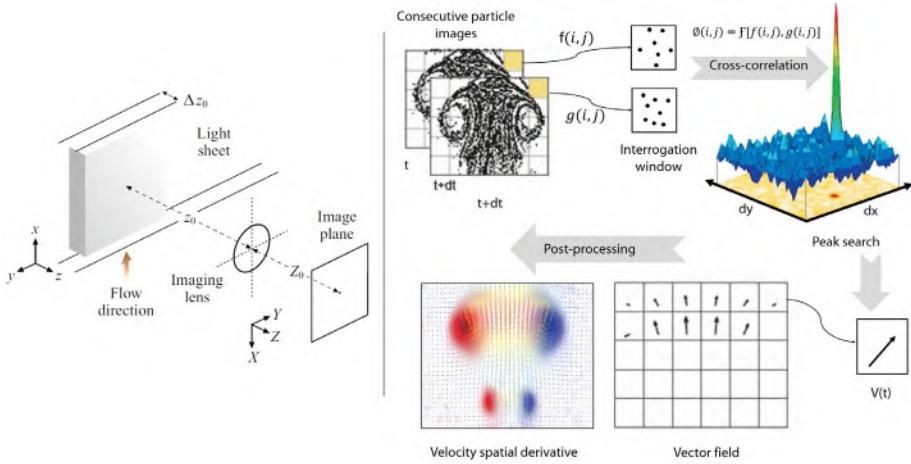


Figure 1-15: *Left:* Optical configuration of PIV imaging. (Adapted from Panton et al. chapter 5). *Right:* Processing of two single exposure frames and consecutive steps for vector calculation. Cross-correlation analysis: sub-samples, $f(i,j)$ and $g(i,j)$, are extracted at the same location within the two frames using an interrogation window. Then, an FFT cross-correlation is performed on these two sub-samples. This procedure results in a cross-correlation distribution with the pixel domain with a dominant peak corresponding to the shift of the particles labelled by (dx, dy) . Finally, the calibration parameters are used to convert the pixel displacement (dx, dy) into a velocity (adapted from LaVision and [32])

One important step during PIV measurement is the calibration procedure, which determines the relation between the particle image displacement in the camera plane and the particle displacement in the laser sheet plane. The calibration step becomes crucial when the viewing direction (of the camera) is not perpendicular to the laser sheet plane, which would lead to a systematic error. Thus, a correction procedure is needed to recover the true velocity components in the illuminated laser sheet plane. Section 1.3.1 describes in detail the PIV calibration for stereoscopic arrangement.

In PIV the Lagrangian motion of particles is used to approximate the instantaneous Eulerian flow velocity. Thus, the particles constitute a pattern that is used to evaluate the flow motion. In order to detect the displacement of the particles between two

consecutive frames a spatial correlation analysis is performed. The probability to detect valid displacement depends on several experimental parameters:

Image density: Keeping constant the in-plane and out-plane displacements the amplitude of the displacement-correlation peak (signal strength) of the spatial correlation increases with the number of particle images in the interrogation window. However, also the random correlations (noise) increases with image density.

Flow motion: Firstly, the loss of correlation due to the out-of-plane displacement is the major limiting factor of the conventional PIV. Increasing out-of-plane motion decreases the peak amplitude of the correlation peak. Secondly, the peak of the displacement-correlation is inversely proportional to the in-plane displacement. Finally, also the local velocity gradient (due to in-plane or out-of-plane motion) influences the peak amplitude.

Keane & Adrian have studied the performances of auto- and cross-correlation on particle images in different conditions [33]. **Figure 1.16** represents the valid detection probability as a function of a dimensionless parameter. The parameter is the product of the mean number of particles (N_1) per interrogation window and loss of pairs due to out-of-plane F_1 and the mean number of particle pairs in each interrogation spot F_0 .

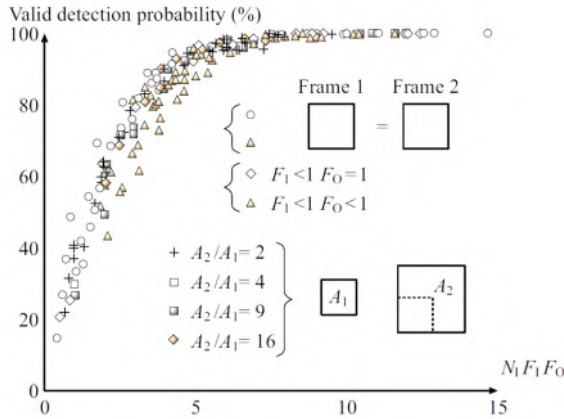


Figure 1-16: Vector detection probability for the displacement-correlation peak as a function of the product of image density N_1 , the in-plane and out-of-plane loss of correlation, F_0 and F_1 , respectively (adopted from [33], [34]). $F_0 = \exp(-8 \Delta z / \Delta z_0)$ and $F_1 = (1 - |\Delta x| / D_I)(1 - |\Delta y| / D_I)$ where Δz_0 is the light-sheet thickness and D_I the size of the interrogation area.

In general, the design rules for planar PIV measurements are fulfilled if:

- The interrogation domain contains at least 10 particle-image pairs.

- The in-plane and out-of-plane motion should be less than about one-quarter of the interrogation window size and light-sheet thickness, respectively. The velocity range and the spatial resolution are limited by the choice of the interrogation window. Considering an interrogation window size of 64, this means that the maximum particle displacement cannot be more than 16 pixels (1/4 of 64). Combined with a maximum frame rate of the camera and laser it will dictate the upper limit velocity. The final spatial resolution can be increased though, by using different processing techniques such as multi-pass and window shifting.
- Local variations (effect of velocity gradient) of the displacement within the interrogation domain should be less than the particle-image diameter.

1.3 STEREOSCOPIC PIV (3C-2D PIV)

Conventional 2C-2D PIV uses a single camera and provides in-plane velocity components only. Another disadvantage of this technique is that the out-of-plane velocity components (that are not captured) at the same time affect the measured in-plane components due to the perspective transformation (**Figure 1.17**). This unrecoverable error becomes a source of error in 2C-2D PIV.

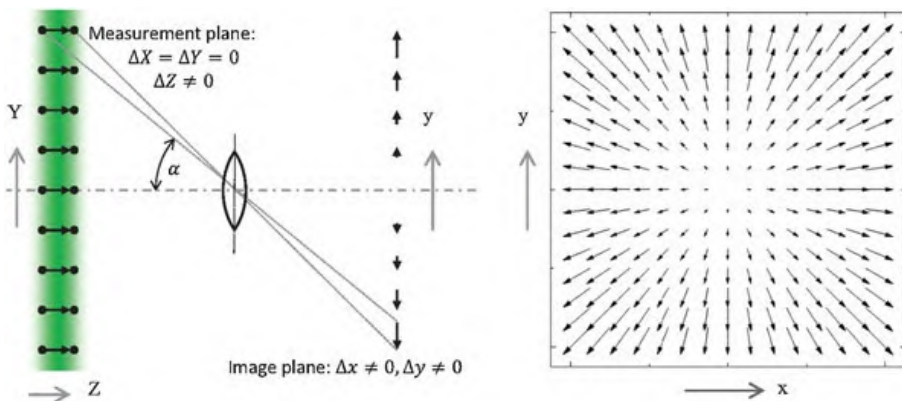


Figure 1-17: Illustration of the perspective error in 2C-2D PIV setup. Left: Constant out-of-plane motion in the laser sheet and zero in-plane motion. The particle displacement recorded by the camera is biased and the magnitude depends on the observation angle with respect to the optical axis. (Adopted from chapter 6 [35])

The stereoscopic PIV (3C-2D PIV) technique is an upgrade of the 2C-2D PIV by allowing simultaneous measurement of all three components of velocity vector (3C) in a two-dimensional domain (2D) [36], [35]. The most adopted stereoscopic

configuration is the angular one (**Figure 1.18a**), which permits large viewing angles and an overlapped view region. In the angular arrangement the two cameras are arranged so that the total opening angle between them is approximately 90° (**Figure 1.18b**). This configuration minimizes the measurement uncertainty such that the uncertainty of the in-plane and out-of-plane components are of the same order [37].

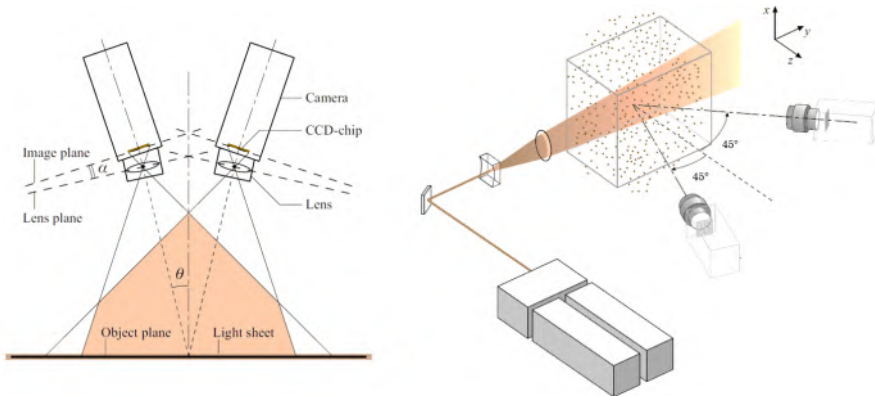


Figure 1-18: *left:* top view of stereoscopic angular arrangement. *Right:* 3D view of a stereoscopic PIV setup (adapted from [34]).

The described stereoscopic configuration leads, however, to a perspective deformation of the image because the magnification factor is not constant. The consequence is that the plane with best focus is not parallel to the illuminated laser plane. A practical approach to circumvent this problem is to tilt the camera plane with respect to the optical axis of the lens (see **Figure 1.16** and **Figure 1.18**), which allows to meet the so-called Scheimpflug condition [38].

1.3.1 Calibration and self-calibration

Considering that the image planes of the two cameras and the principal planes of the camera lenses are rotated with respect to the laser illuminating plane, perspective distortions will be introduced in the recorded images. To correct the perspective distortions, a stereoscopic PIV calibration procedure is required to determine the mapping function between the physical space and the image planes (sensor) of the cameras. In practice this is done by performing an in situ physical calibration based on the recording of images of a calibration plate (**Figure 1.19**) placed first in the centre of the laser sheet, then across the depth in a few other parallel planes. Based upon the acquired calibration target images, the markers are identified by cross-correlating the images and searching the local maxima of the cross-correlation map. Subsequently, a third-order polynomial fitting function [39] is applied to establish the relationship (F^c) between the coordinate system of the measurement domain (x, y, z) and the

coordinate system of the camera plane (X, Y) . The resulting mapping function is used to de-warp raw particles images.

$$X^c = F^c x_i, \quad i = 1, 2, 3 \text{ for } x, y, z. \quad c = 1, 2 \text{ for right and left camera}$$

Tracer particles at the position x_i in the first frame move to the new position $x_i + \Delta x_i$. The displacement in the camera coordinate can be expressed as $\Delta X^c = F^c(x_i + \Delta x_i) - F^c(x_i)$. The displacement ΔX in the location x is obtained by performing a first order Taylor expansion: $\Delta X \cong (\nabla F) \cdot \Delta x$, the following equation provides a set of equations of each component that are generally solved by means of a least-squares method.

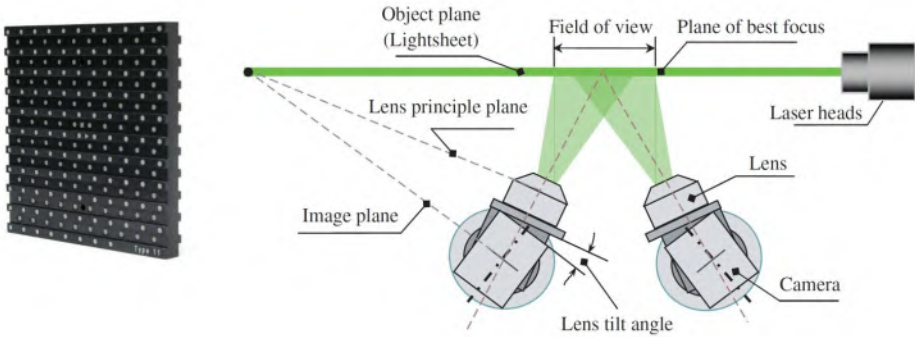


Figure 1-19: *Left:* Calibration plate with highly-contrasted circular markers (adapted from LaVision). *Right:* top view of stereoscopic angular arrangement with Scheimpflug (adapted from [40])

The stereoscopic PIV calibration assumes that the calibration target coincides with the laser sheet plane and that the calibration conditions stay constant during the experiment. In practice, to further improve the physical calibration for the misalignment between the target and laser sheet (**Figure 1.20**) an off-line calibration is performed, referred in literature as self-calibration [41]. In order to correct the discrepancies between de-warped particle images recorded by the two cameras, a cross-correlation is performed between the particle images generating a disparity map. The calibration coefficients (in the third-order polynomial function) calculated based on the physical calibration will be updated after self-calibration iterations such that the length of the disparity vectors will be minimized.

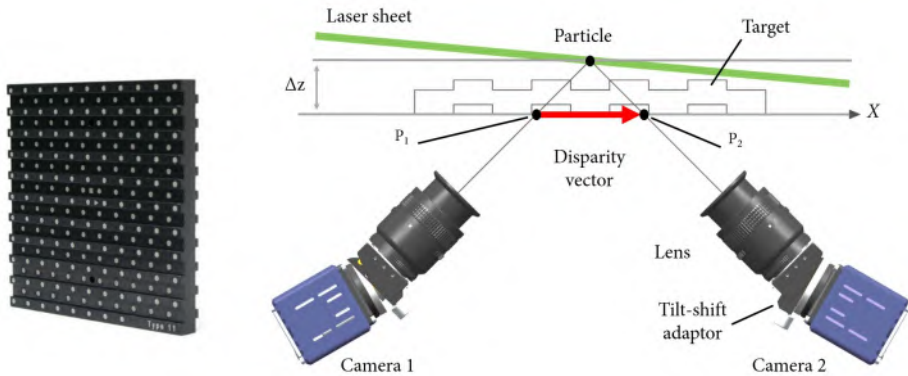


Figure 1-20: Concept of disparity vector due to misalignment between calibration target and laser sheet. P_1 and P_2 are the particle in the de-warped image of camera 1 and camera 2, respectively (adapted from LaVision).

1.4 3C-3D PIV TECHNIQUES

1.4.1 Reconstructive techniques: Scanning and multiplane PIV

In cardiovascular fluid mechanics, the range of problems addressed by engineers has grown considerably. Most of the flow problems of interest are of 3D nature, which require more advanced flow velocity techniques. As mentioned in the previous section, 2C-2D PIV provides four components of the velocity gradient tensor by measuring in-plane velocity components. Instead, the 3C-2D PIV adds two components to the velocity gradient tensor by recovering the third velocity component in the 2D plane.

In view of these limitations, much effort has been dedicated to the development of PIV to several dimensions to be able to estimate the spatial distribution and the derivatives of the velocity field. For this purpose, conventional and stereoscopic PIV measurement can be performed at several positions (at high velocity if needed) to reconstruct the volumetric velocity field. In the chapter 2 we will describe in detail a multi-plane PIV setup that has been designed during the PhD course.

There are also several variants and extensions of stereoscopic PIV method that allow to estimate the whole velocity gradient tensor. Here we will briefly describe the dual-plane system [42]–[44] and scanning PIV [45][46], [47]. The first one consists basically of two synchronized stereoscopic PIV setups to measure the velocity in two parallel laser sheets orthogonally polarized. The illumination consists of four-pulse laser systems and polarizing beam-splitter cubes, to separate the light sheet (**Figure 1.21a**). The dual-plane resolves the velocity gradient tensor and it allows high density seeding, since it

uses stereoscopic PIV concepts. However, it is limited to a planar section and requires meticulous adjustment of the laser sheet and optics positions.

The second approach consists of using a planar laser sheet to scan the measurement domain at high speed to ensure the reconstruction of the quasi-instantaneous velocity field. For this purpose, a rotating/oscillating component is added to the PIV system to reflect the laser beam (Figure 1.21b). High-speed scanning PIV has the advantage to reconstruct the whole 3D domain. However, only slowly evolving flows can be investigated, as the parallel planes within the volume must be recorded sequentially at different time instants. Therefore, the volume must be scanned in a time interval smaller than the timescale of the flow. Additionally, the dimension of the investigated volume is limited by the depth of focus of the cameras.

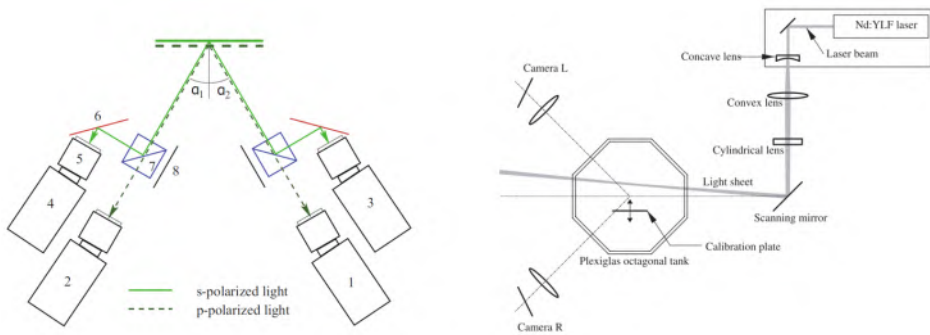


Figure 1-21: Dual-plane stereoscopic PIV and scanning PIV adapted from [42] and [45], respectively.

1.4.2 Tomographic PIV

The interest to visualize the 3D flow field has stimulated the rapid development of different PIV techniques, requiring advanced hardware components, more complex optical configurations, improved image processing algorithms, and innovative ways to graphically represent the complex flow data [48]. Tomo-PIV [49], [50] is a multi-camera system that provides instantaneous 3D information, where the reconstruction of the volumetric flow field is achieved by taking simultaneously two-dimensional images of the particles from several views. Other truly volumetric PIV-based techniques are 3D particle tracking velocimetry (3D-PTV [51], Shake-The-Box [52], digital holographic [53], defocusing PIV [54] [55], and light field imaging [56].

We dedicated this section to briefly describe the working principle of the method of choice for volumetric velocity measurement. Tomographic PIV (briefly 3C-3D-PIV or

Tomo-PIV) achieves the information in depth of the illuminated volume via simultaneous recording with several cameras (typically 3 to 6 cameras) from different viewpoints (**Figure 1.22**). As in conventional PIV, the images are recorded as double frames. The particle images are used to reconstruct the 3D intensity distribution. To build the 3D particle distribution an iterative reconstruction that adapts the intensity in each voxel in such way that the back-projection of the voxels in the camera direction match the actual particle image. Subsequently, a 3D cross-correlation is performed to detect the particle displacement in the space and extract the velocity field of the reconstructed volume of two time instances (**Figure 1.22**).

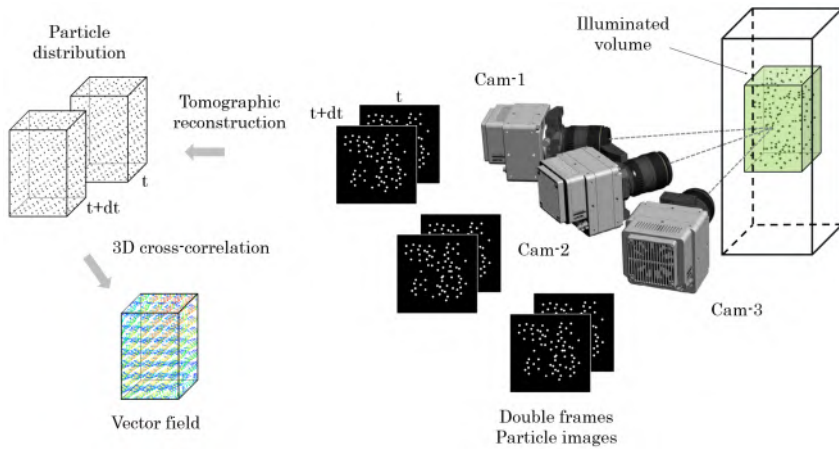


Figure 1-22: Working principle of tomographic PIV.

Volume illumination: As with planar PIV, the tracers are illuminated by a pulsed laser to freeze the particles at two time instants. Practically, setting up a volume illumination is simpler than generating a thin laser sheet. Diverging lenses are used to generate volume illumination. However, one of the limiting factor in Tomo-PIV experiments is the illumination volume since the pulse energy decreases with increasing the measurement volume. One solution to increase illumination intensity is to recycle the light by placing a mirror for double [57] or multiple light passes [58]. The idea consists of placing a mirror is placed in the opposite side of the region of interest to double the light intensity (**Figure 1.23a**). A second approach to maximize the light intensity deals with complex system for multi-pass illumination, where the laser beam is expanded and sent towards the region of interest (**Figure 1.23b**). The laser reflects multiple times and overlap inside two mirrors increases the amount of light scattered up to a factor of 7. A secondary effect of illuminating the particles from both sides is that the cameras can receive light in forward scattering direction.

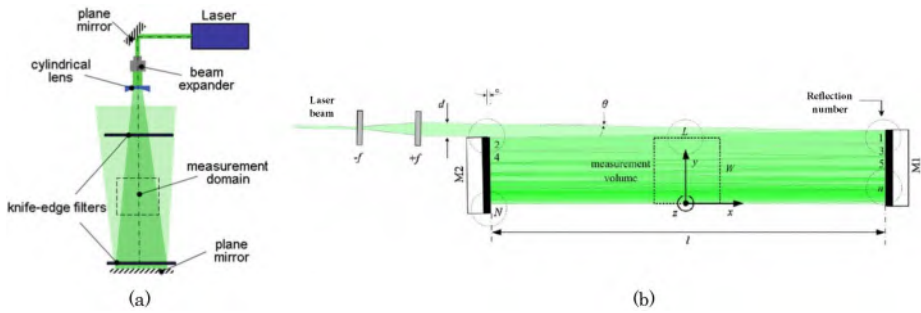


Figure 1-23: Strategies for laser light amplification. A) double-pass. B) Multi-pass

Seeding: The seeding density determines the spatial resolution of the measurement. In Tomo-PIV the quality of the reconstruction and consequently the velocity vector field, decreases with the seeding density. A second metric to estimate the seeding density is the source density (N_s) (Keane and Adrian 1992) defined as the fraction of image occupied by the particle images. Elsinga showed that a Tomo-PIV setup with four camera system can accurately reconstruct particle images with a seeding density of 0.05 particle per pixel ($N_s = 0.16$) (**Figure 1.24**). The performance of the algorithm for the tomographic PIV reconstruction is seeding dependant. The particle identification scheme suffers in case of overlapping particles. As shown in **Figure 1.24**, the quality of the reconstruction drops down as the source density reaches values higher than 0.09. Denser particle reconstruction is possible by increasing the number of cameras, performing accurate calibration and using advanced reconstruction methods.

Volume reconstruction and 3D calibration: Tomo-PIV relies on the reconstruction of the 3D distribution of scattering objects into the measurement volume using multiple projections of it. The reconstruction is based on analysing the light intensity scattered by the tracer particles recorded in 2D images. Since we have limited projections of the object, the reconstruction is an underdetermined system solved by mathematical algebraic techniques. As Tomo-PIV does not rely on single particle identification the number of imaged particles is limited by the large diameter and possibility of overlapping, which leads to speckles phenomena. Therefore, the reconstruction of the 3D particle distribution depends strongly on the seeding density.

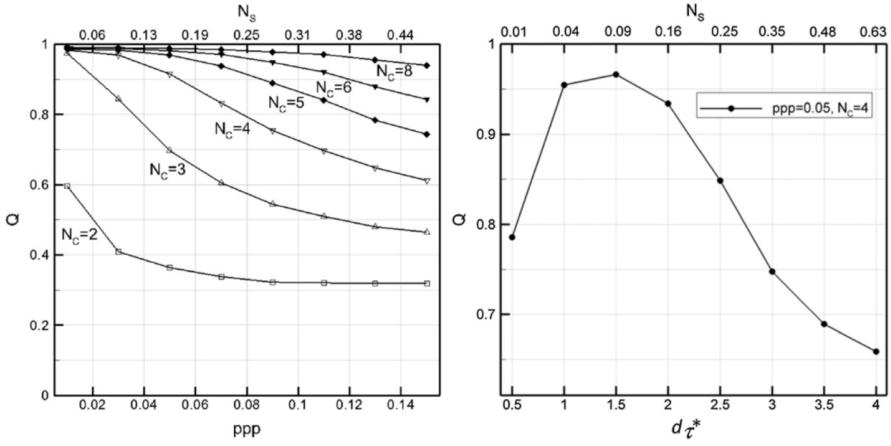


Figure 1-24: The source density defined as $N_s = ppp \pi/4 (d_\tau^*)^2$, where $d_\tau^* = d_\tau/\Delta_{pix}$ is the pixel normalized particle image diameter and ppp is particle per pixel. Q is a normalized cross-correlation coefficient (or named quality factor). *Left:* Q as a function of image source density parametrized as function of the number of the cameras. *Right:* Q as a function of particle image diameter d_τ^* at a chosen particle image density ppp . (Adapted from [50])

The intensity recorded by each pixel of the camera represents the integration of the intensity along a view direction through the volume **Figure 1-24**. The reconstructed intensity light $f(x_j, y_j, z_j)$ scattered by the particles in the volume of interest is projected onto camera sensor $PI(X_i, Y_i)$. The algebraic method iteratively solves a set of linear equations linking the $PI(X_i, Y_i)$ in the image space to the 3D object.

$$PI(X_i, Y_i) = \sum_{j=1}^{N_{vox}} w_{i,j} f(x_j, y_j, z_j), \quad i = 1, \dots, N_{pix} \quad (2)$$

The subscripts i and j represent the i^{th} pixel and j^{th} the voxel, respectively. N_{vox} indicates the total number of voxels along the line of sight. N_{pix} is the Number of pixels. The weighting coefficient $w_{i,j}$ defines the contribution of the intensity of the j^{th} voxel on the intensity recorded on the i^{th} pixel.

Elsinga has proposed an exciting iterative algebraic reconstruction technique as the most suitable for Tomo-PIV signal reconstruction [59]. Due to the limited number of views (number of cameras) of the imaging, a multiplicative algebraic reconstruction technique (MART) is used to solve the system (2) to iteratively update an initial guess for the intensity distribution $f(x_j, y_j, z_j)$. MART in the framework of Tomo-PIV behaves as a logic AND operator, thus each voxel carries a non-zero intensity only if the signal is present on every projection. Consequently, the zero-intensity projection are set to zero. The MART technique assumes that the object to be reconstructed is a densely populated volume with bright spots on a dark background.

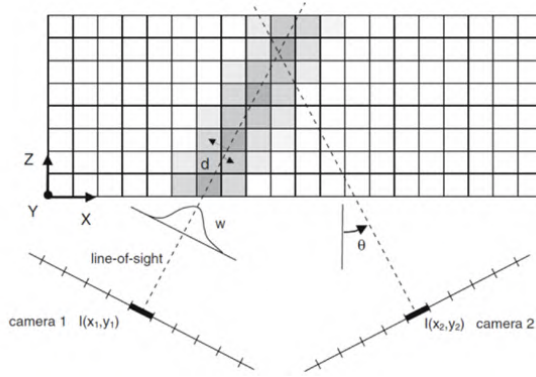


Figure 1-25: Sketch of a simplified (two cameras) projection model for tomographic reconstruction. The grey scale values of the voxels is function of the distance between the line of sight and the voxel (adapted from [60])

The relation between the physical coordinate system (x, y, z) and the image space (X_i, Y_i) is established by a volume calibration. As with stereoscopic PIV, a set of images of the calibration plate are recorded at several parallel planes. The calibration contains high-contrasted markers with known (x, y) in the plane. The position of the markers is identified by cross-correlating the images. Subsequently, a third-order polynomial fitting function [39] is applied to establish the relationship between the measurement domain and the camera plane coordinates for all markers to obtain the mapping function, expressed as

$$\begin{aligned} x &= a_0 + a_1X + a_2X^2 + a_3X^3 + a_4Y + a_5Y^2 + a_6Y^3 + a_7XY + a_8X^2Y + a_9XY^2 \\ y &= b_0 + b_1X + b_2X^2 + b_3X^3 + b_4Y + b_5Y^2 + b_6Y^3 + b_7XY + b_8X^2Y + b_9XY^2 \end{aligned}$$

The coefficients (a, b) depend on the position z of the calibration plate. The mapping function is calculated at each z position and interpolated at intermediate z positions. A good tomographic reconstruction requires that each voxel position in space is mapped into a camera pixel position with an error preferably lower than 0.1 pixel. The requirements on the physical calibration errors due to inaccuracies in the detection of the spots in the calibration images or vibration of the experimental arrangement are stricter than stereoscopic PIV. The calibration correction method, proposed by Wieneke [61], is based on the evaluation of the disparity vector field that is used to minimize the remaining errors in the mapping function. The correction is based on the particle images recorded from each camera. The registration error is corrected by modifying the coefficients of the polynomial fit used for the physical calibration.

The intensity field reconstructed is normally affected by two artefacts due to the ambiguity in estimation of the correct position of the particles along the line of sight.

The artefacts can be grouped in two categories:

Ghost particles [51]: due to the limited views of the volume of interest, the solution of the projection equation is ill-posed (non-uniqueness). Ghost particles consist of spurious intensity spots at the intersection of the line of sight that does not correspond to the position of actual particles (**Figure 1.26**). The number of ghost particles depends on the seeding density, thickness of the illumination volume and the number of cameras. Ghost particles can lead to velocity bias errors under some circumstances [62] (**Figure 1.26**). Normally, the ghost particles artefact has a smoothing effect on the velocity which results in an underestimation of the velocity gradients.

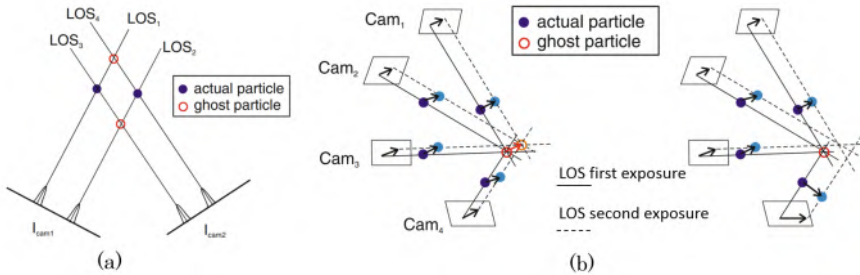


Figure 1-26: (a) Formation of ghost particles in a two-camera setup. (b) An example of a ghost particle formation in both exposures from 4 actual particles. In this case the particle will appear as an actual particle and affect the correlation map. In the second case the ghost particle appears in the first exposure in all cameras, but not in the camera number 4 due to different velocity gradient. In this case the does not contribute to build the correlation map. (Adapted from [62])

Several groups have proposed different approaches to reduce the computational time of MART and to enhance the reconstruction accuracy by means of ghost particle reduction and increasing the seeding density, for example [63], a technique named multiplicative line of sight (MLOS) that takes advantage of the sparseness of the reconstructed domain. In fact, at least 90% of the reconstructed domain has intensity that could be excluded from the reconstruction procedure. Thus, non-zero projections on each camera are multiplied to estimate a first 3D particle intensity distribution. In order to reduce the ghost particles, the MLOS is successively followed by a MART variant (SMART) which refines the reconstruction. A second approach, motion tracking enhancement (MTE) that exploits the time information to reduce the ghost particles artefact was proposed by Novara et al. [64].

Shape errors: The spatial arrangement of the imaging system is an important parameter to optimize during the experimental setup (**Figure 1.27a**). A typical Tomo-PIV setup is formed from a small number of cameras, at least 3. The angular aperture, defined as the angle between the cameras, influences the resolution in the depth

direction. The influence of the angular aperture on the accuracy of the particle field reconstruction has been studied by Elsinga et al [49], who reported an optimum angular aperture β ranging approximately between 40° and 80° in two possible camera configurations (**Figure 1.27a**). A small angular aperture leads to elongation of the reconstructed particles in the depth direction (**Figure 1.27**). Conversely, higher values of the angular aperture imply longer intersection of the line of sight within the reconstructed domain, which results in a higher number of ghost particles.

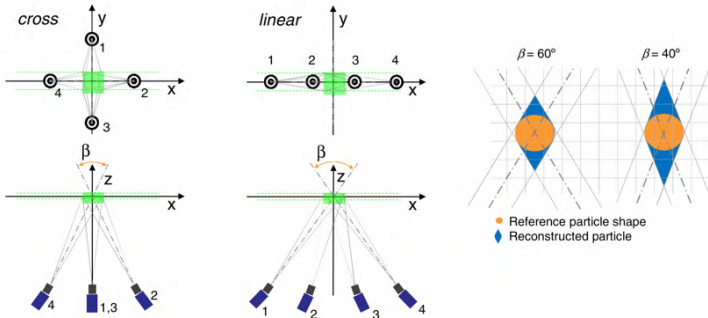


Figure 1-27: *Left:* front and top view of two possible imaging system arrangement. Cross-like and linear configuration. *Right:* Schematic sketch of the effect of the angular aperture for a two-camera system. (After [50])

Single-calibration Multiplane PIV within an Idealized Pulsatile Left Ventricle Model

*The contents of this chapter were published in
Experiments in Fluids
(2018) 59:49 (3)*

**Single calibration multiplane stereo-PIV: the effect of mitral valve orientation on
three-dimensional flow in a left ventricle model**

H. Saaid, P. Segers, M. Novara, T. Claessens, P. Verdonck

Abstract: *The characterization of flow patterns in the left ventricle may help the development and interpretation of flow-based parameters of cardiac function and (patho) physiology. Yet, in vivo visualization of highly dynamic three-dimensional flow patterns in an opaque and moving chamber is a challenging task. This has been shown in several recent multidisciplinary studies where in vivo imaging methods are often complemented by in silico solutions, or by in vitro methods. Because of its distinctive features, Particle Image Velocimetry (PIV) has been extensively used to investigate flow dynamics in the cardiovascular field. However, full volumetric PIV data in a dynamically changing geometry such as the left ventricle remains extremely scarce. We describe an innovative experimental setup, which allows for an efficient multiplane scanning stereoscopic PIV measurements in independent planes. The peculiarity of the present setup is that it permits volume reconstruction, performing only one single calibration. We present an application on left ventricle flow, adopting a customized cardiovascular simulator. The instantaneous and ensemble averaged velocity vector field maps are acquired, as well as the reconstructed three-dimensional flow structures downstream of a mechanical prosthetic heart valve.*

2.1 INTRODUCTION

An example of 3D swirling flow can be found in the biomedical engineering field, in particular the flow within the human LV. The LV supplies oxygenated blood to the circulatory system, and it is the most muscular, energetic and largest chamber of the heart. Numerous studies and topical review papers have shown that specific LV flow patterns are of physiological, clinical and pathological interest [2], [18], [65]. The evaluation of the LV in terms of flow properties provides a different insight into the LV hemodynamics, beyond pressure and flow rates, and reflects cardiac abnormalities before structural changes appear [66], [67]. The passage of the blood flow from the left atrium to the LV, for example, was found to generate vortices that play an active role in cardiac function, avoiding kinetic energy dissipation by reorganizing the incoming blood in a compact structure and preventing thrombus formation [11], [24], [68]–[70]. A vast number of PIV studies have also been performed to identify how the orientation of the prosthetic aortic valve affects the flow distribution in the sinuses of Valsalva region [71]. Less attention has been given to the effect of mitral valve implant orientations on the LV fluid mechanics. Pierrakos et al. (2004) and Akutsu and Fukuda (2005) have performed a comparative time-resolved 2D PIV study to investigate the evolution of the flow in LV model in different mitral valve orientations [72], [73]. In recent work, Westerdale et al. (2015) evaluate the effects of three different angular valve

positions, by comparing 2D PIV data and ultrasound images. As concluded by the authors, due to the multidirectional flow phenomena on the LV model, a 3D flow measurement is a prerequisite to examine the flow evolution.

The objective of this work is to further contribute to the field of LV flow quantification by exposing the potential of an alternative multiplane stereoscopic PIV setup to reconstruct the 3D flow field in a compliant silicon LV phantom in different controllable and repeatable conditions. The effects of the angular orientation of a mechanical bileaflet valve on the flow topology in LV model are investigated through reconstruction of the flow field during early filling and diastasis. The study shows that the scanning stereo-PIV setup allows for the accurate reconstruction of the complex 3D flow within the ventricle model, without having to resort to full tomographic illumination and imaging systems, typically characterized by higher setup complexity (i.e. distortion-free optical access to the investigated volume, lower illumination energy within the volume), costs and computational time for the evaluation of the particle images. The present technique takes advantage of the periodic nature of the flow, as phased-locked scanning stereo PIV measurements were carried out at several parallel planes.

2.2 METHODS

2.2.1 Optical configuration

The setup was primarily designed and developed to facilitate consecutive stereoscopic measurements without repeating the elaborate and time-consuming calibration procedure (see section 1.2.4). The scanning system (**Figure 2.1**) enables the acquisition of particle images from two cameras at several parallel planes along the viewing direction of the imaging system covering a volume of $80 \times 70 \times 80 \text{ mm}^3$; the 2D-3C velocity fields obtained by the stereoscopic analysis (stereo-PIV) of the camera images can be used to reconstruct the volumetric flow field. The key features of the present setup are the two hexagonal tanks (**Figure 2.2**), made from PMMA material with a refractive index close to 1.49 to match the working fluid. The 10 mm thick PMMA plates were machined and then glued together using reaction adhesives (Acrifix 192, Evonic Industries). The shape of the two tanks was chosen such that the optical access can be established orthogonally through the walls. The LV phantom was immersed in the inner tank that is connected to the pulsatile pump via a rigid tube (**Figure 2.1**). The outer tank is open and can translate relatively with respect to the inner one together with the traversing system. The PIV apparatus was built on a rigid aluminium modular scaffolding system (**Figure 2.1**). The two cameras, external tank and optical lenses were mounted on a slide rail stage, which is connected to a motorized linear transverse with

an accuracy of ± 0.02 mm (LES4, Isel Germany AG, Eichenzell, Germany). A computer interface allows to control the position of the PIV apparatus and thus to determine the scan planes where stereoscopic PIV measurements are performed.

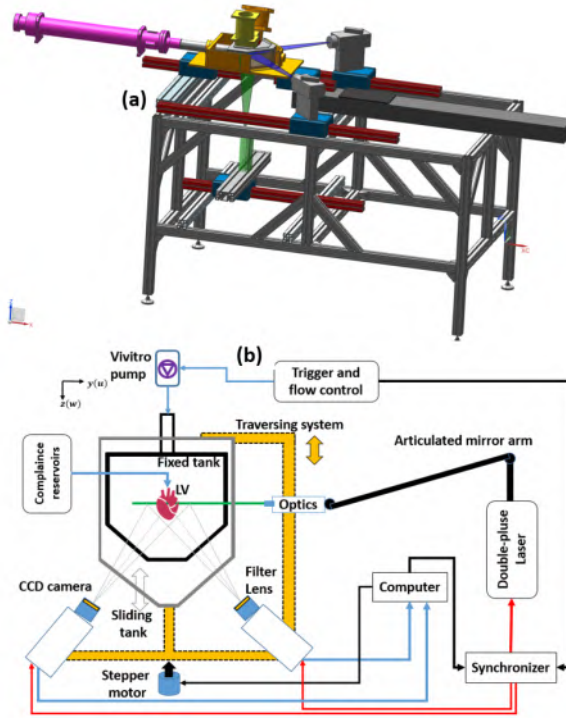


Figure 2-1: (a) 3D CAD view of the experimental apparatus (b) Basic layout of the setup: CCD cameras, laser sheet, optical lenses, hydraulic components and the control system components.

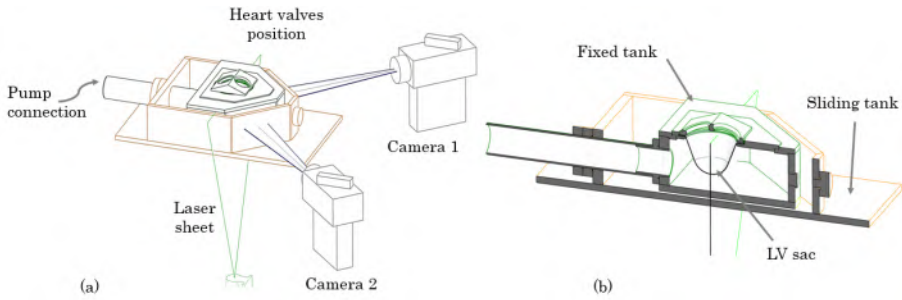


Figure 2-2: 3D sketch of the imaging system cross-section of the double-tank assembly, showing the LV membrane.

2.2.2 Imaging system

The recording system consists of two CCD sensor cameras (PCO.2000, PCO, Germany) with a maximum resolution of 2048×2048 pixels, 14 bits dynamic range and a maximum image rate of 14.6 frames per second (fps). To minimize the out-of-plane velocity component measurement error, the angle between the two camera bodies was set at 90° (**Figure 2.1.**). Each camera was equipped with a prime lens with a focal length of 100 mm (Canon EF 100mm f / 2.8 Macro USM) and mounted on tilt adapters which allows fine adjustment of the Scheimpflug angle. An aperture with an f stop of 5.6 has been used. A double-cavity pulsed Nd: YAG laser (Twins BSL 140, Quantel, USA) delivering 140 mJ/pulse with a repetition rate of 15-30 Hz was used as an illumination source. A compound of spherical and cylindrical lenses was adopted to shape the laser beam in a uniform laser light sheet (thickness ~ 1.5 -2 mm), measured using photosensitive paper (Brovira-Speed, Agfa-Gevaert, Leverkusen, Germany). Due to the fact that the optical lenses translate during the measurement session, the laser beam had to be guided via an articulated arm (ILA, GmbH, Juelich, Germany), which translates along the camera system.

2.2.3 Hydraulic circuit

Cardiovascular fluid experiments require a specific hydraulic facility to imitate in vivo flow conditions. A commercially available cardiovascular simulator (Vivitro Systems, Inc., Victoria, BC, Canada) that can impose different physiological flow conditions was adopted. The hydraulic piston pump was connected to the inner tank (**Figure 2.2**). To reproduce normal cardiac flow curves, the pulsatile pump was velocity-controlled and driven with a (FDA approved) waveform able to reproduce physiological flow pattern, with a frequency of 70 cycles/min and a duty cycle of 35%, resulting in a 300 ms systolic period. The pulsatile pump generates volumetric changes in the inner tank, which

produce inflow and outflow in the LV phantom. The end systolic and stroke volume were set to 55 and 50 ml, respectively. Compliance and resistance elements were fine-tuned to achieve a desired physiological pressure wave form. To monitor the pressure in the aortic, atrial, and ventricular site, pressure transducers (6069, Utah Medical Products, Inc., Athlone, Ireland) were placed in the respective positions in the hydraulic setup. Two standard mechanical bileaflet valves of 25 mm and 19 mm (Carbomedics) were mounted in the mitral and aortic position, respectively. The setup also allows mounting the flowmeter downstream as well as upstream the aortic and mitral valve, respectively. The measurements were carried out in a thin-wall silicone LV model with symmetric elongated spheroid geometry (Vivitro Systems, Inc., Victoria, BC, Canada). The thickness of the LV model wall was 0.58 mm. The silicon has a refractive index of about 1.4.

To evaluate the effects of the orientation of the prosthetic mitral valves on the LV flow structures, a 25 mm bileaflet valve (Carbomedics) has been tested in two different angular positions. Two series of experiments have been conducted: (i) with the mitral valve oriented perpendicular to the laser sheet plane (anatomical orientation, AO) (**Figure 2.3a**), and (ii) with the mitral valve oriented parallel to the laser sheet plane (anti-anatomical orientation, AAO) (**Figure 2.3b**).

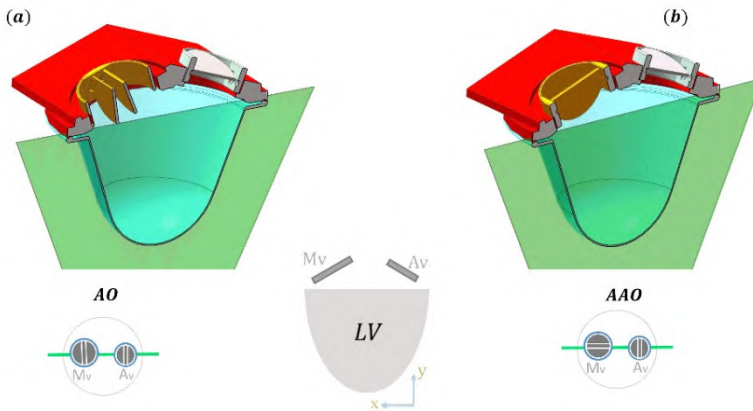


Figure 2-3: Sketch of the LV assembly in two different configurations; (a) anatomical and (b) anti-anatomical orientation.

2.2.4 Test fluid and tracer particles

To mimic the rheological properties of blood and to avoid optical distortions during the measurements, a three component mixture was used as working fluid [74] to fill both Plexiglas tanks. The solution consists of sodium iodide, glycerol and distilled water mixture at volume fraction of 79:20:1, respectively. The kinematic viscosity and density

of the working fluid was equal to $3.3 \cdot 10^{-6} \text{ m}^2/\text{s}$ and 1750 kg/m^3 [75], at room temperature. The hydraulic parameters of the setup have been set that dynamic similarity is fulfilled. The corresponding dimensionless parameters, the Reynolds (R) and Womersley (α) numbers, were equal to 4090 and 7 respectively. The Reynolds and Womersley numbers were calculated using the following formulas: $R = \frac{\rho V D}{\mu}$; $\alpha = D \sqrt{f \rho / \mu}$; where V is the peak velocity, D the valve diameter and f the frequency (1.16 Hz). To overcome the problem of the laser light reflections in the LV model, fluorescent Rhodamine-B coated particles with an average diameter of $10 \text{ }\mu\text{m}$ and density of $1,100 \text{ kg/m}^3$ were used as tracer in the intraventricular test fluid. To selectively capture the scattered particle light, a long-pass filter at 550 nm (Thorlabs, Inc., Newton, NJ, USA) was mounted in front of each camera. The suitability of the particles was evaluated by calculating the settling velocity (Prasad et al. 2000b) given by the following formula, $v_{\infty} = gd^2/18\mu (\rho_p - \rho_f)$ where d and ρ_p are the particle diameter and density, respectively, and μ and ρ_f are dynamic viscosity and density of the fluid. The settling velocity (in this case rise velocity) was $6 \cdot 10^{-6} \text{ m/s}$ and the relaxation time in the order of microseconds. Thus, the effect of the density mismatch between the particle and working fluid can be considered negligible.

2.2.5 Calibration

Stereoscopic PIV (SPIV) allows for the reconstruction of all three velocity components within a two-dimensional domain. Planar velocity fields from two cameras, acquired at the same time instant, are combined to obtain the out-of-plane velocity component. A calibration of the imaging system is required to combine the planar information in stereoscopic fashion [37]. The term multiplane Particle Image Velocimetry is used when SPIV is performed in a series of neighbouring parallel planes, and allows for a 3D reconstruction of the flow field. In case of a glass-air interface (such as with liquid flows), calibration must be repeated at every plane of the scanning sequence, unless telecentric lenses are used. Yagi et al. (2006; 2011); and Buchmann et al. (2011) have adopted sophisticated traversing and moving prisms systems, respectively, that required only one set of calibration data [77]–[79]. Due to the simultaneous traversing of the complete PIV system and of the outer tank, the camera viewing direction is maintained normal to the interfaces and the calibration procedure can be carried out at a single traversing position, which allows for a reduction of the set-up time.

The calibration images from the two cameras were taken at mid-plane of the volume of interest. A multilevel target of $120 \text{ mm} \times 120 \text{ mm}$ with cross markers distributed uniformly with an interval of 10 mm was placed in the measurement location. During the calibration and the recording of the particle images, both tanks were filled with the same index-matching solution, to ensure analogous optical conditions during the

measurements. The calibration was performed by replacing the LV model with the calibration target. A pair of images of the calibration plate was recorded by each camera and used to reconstruct the mapping function using commercial software (PIVTEC, Gottingen, Germany). To map the 3D space object onto the two-dimensional camera sensor plane, a pinhole Tsai model was applied (Tsai et al. 1986); this calibration method does not require any physical information of the experimental arrangement. To eliminate the need to perform calibration in each measurement plane individually, the external tank, CCD cameras and the optical lenses have been rigidly connected to a traversing mechanism equipped with a stepper motor (see above). Throughout the scanning sequence, the whole PIV system translates simultaneously with the external tank, while the internal tank (which encloses the LV replica) is kept fixed on the structure setup. Hence, the relative optical positions between the cameras and the measurement plane are secured and the light path remains unaffected, as the distance between the image plane and the laser sheet plane is constant (**Figure 2.4**). In other words, the magnification factor is constant during measurements series, yielding an identical mapping function in each measurement plane. Special care has been taken to ensure optimal mechanical alignment of the slide rail on which the stereo-PIV components have been mounted. Systematic errors due to the misalignment between the cameras and tanks slide rails were kept to less than ± 0.1 mm along the scanning length (dial indicator with a graduation of 0.01 mm, Mitutoyo Corporation, Japan).

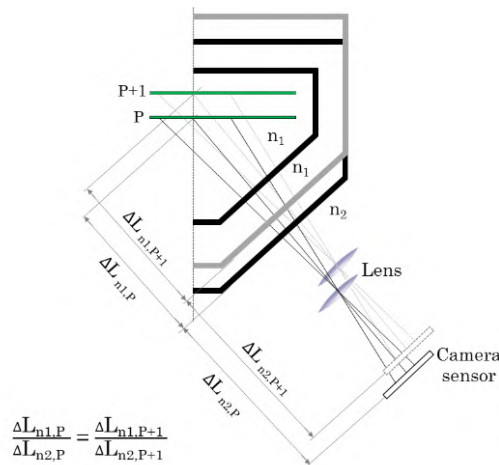


Figure 2-4: Schema of double-tank system

The self-calibration technique proposed by Wieneke [41] is applied here to correct for the possible misalignments of the target with respect to the illumination sheet. Particle

images acquired at the same time from the two cameras are cross-correlated to evaluate the disparity map on the XY plane; the disparity vectors are used to modify and correct the camera mapping functions obtained by the physical target calibration. Results show that the residual disparity after correction is significantly smaller than the laser sheet thickness, which ensures the accuracy of the three velocity components by means of the stereoscopic technique. Furthermore, as the self-calibration procedure is applied for each measurement plane using the mapping functions obtained from the target calibration performed at the mid-plane location, the successful reduction of the disparity errors confirms that no major change of the relative position between the imaging system and the measurement region takes place during the traversing of the system.

2.2.6 Validation

Regarding the imaging system calibration, we followed a well assessed procedure for stereo-PIV measurements consisting in the physical calibration followed by the correction of the camera mapping functions performed with the aid of particle images. A target with markers positioned at known locations is placed at the location of the laser sheet and imaged by the cameras; the mapping functions between the measurement plane and the camera sensor plane are obtained by identifying the same markers on the two images. Subsequently, the self-calibration approach is followed; a cross-correlation approach is performed between the images of the two cameras (dewarped onto the physical space using the mapping functions obtained by the target calibration) in order to estimate the disparity error map. The disparity map is then used to correct the cameras mapping functions. This procedure ensures that the calibration errors arising from the misalignment between the target and the illuminated plane are compensated for, and that the stereo approach can be used to accurately combine the 2D-2D information provided by the single cameras into the final 2D-3C velocity fields. Moreover, a successful self-calibration (indicated by robust disparity correlation maps) proves that the physical target calibration was carried out accurately enough for the misalignment to be compensated for. In fact, in case of major errors in the calibration target positioning, the dewarped particle images from the two views would not correlate.

In the present study the physical target calibration is performed only at the central Z plane of the scanned volume (reference plane); the mapping functions obtained at this location are used, for each measurement location along Z, as the starting point for the self-calibration correction.

The correlation of the dewarped images from the two cameras results in the disparity map shown in (**Figure 2.5**). As expected, given that cameras are imaging the domain from two different locations along the X axis, the X component of the disparity is much

larger than the Y component. De-calibration errors up to approximately 60 pixels are found, which are representative of the misalignment errors typically encountered in several stereo-PIV experiments.

The disparity map is used to correct the system calibration; then, the residual disparity error is evaluated performing the same cross-correlation operation between the two particle images where the dewarping is carried out using the corrected cameras mapping functions.

The residual error is shown in (**Figure 2.5**); the effectiveness of the self-calibration procedure is demonstrated by the significant reduction of the calibration error, confirming that the single target calibration performed at the reference plane can be corrected also at different planes along the Z axis across the measurement volume. The residual disparity values are well below the thickness of the laser sheet (~ 70 -80 px), ensuring an accurate reconstruction of the three velocity components by means of stereo combination of the 2D-2C fields.

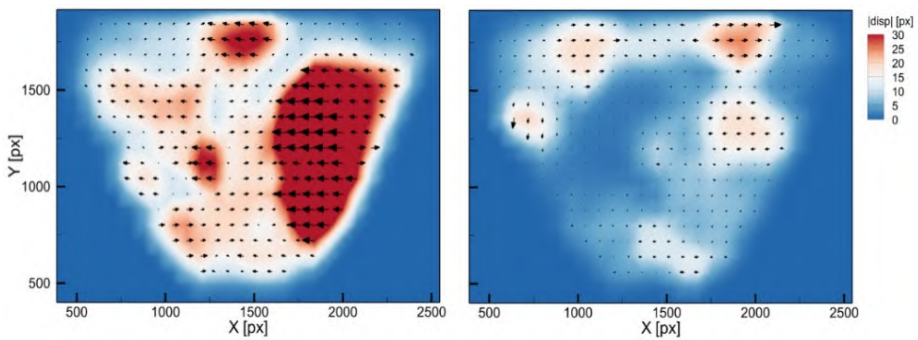


Figure 2-5: Contours of disparity error magnitude at $Z = 18\text{ mm}$; vectors show the two disparity components. *Left:* disparity error after physical target calibration. *Right:* residual error after self-calibration correction.

Nevertheless, in order to dispel any doubt about the accuracy of the correction procedure followed in the present investigation, we add here a comparison between the two approaches. For this purpose, we have compared the velocity fields obtained through the classical calibration approach (blue line in **Figure 2.6**) with the ones obtained with the single calibration technique (red line in **Figure 2.6**). The comparison is carried out at two Z locations, 5 and 10 mm away from the reference plane (**Figure 2.6** top and bottom, respectively). Both the velocity vector magnitude and its components showed an excellent qualitative and quantitative agreement.

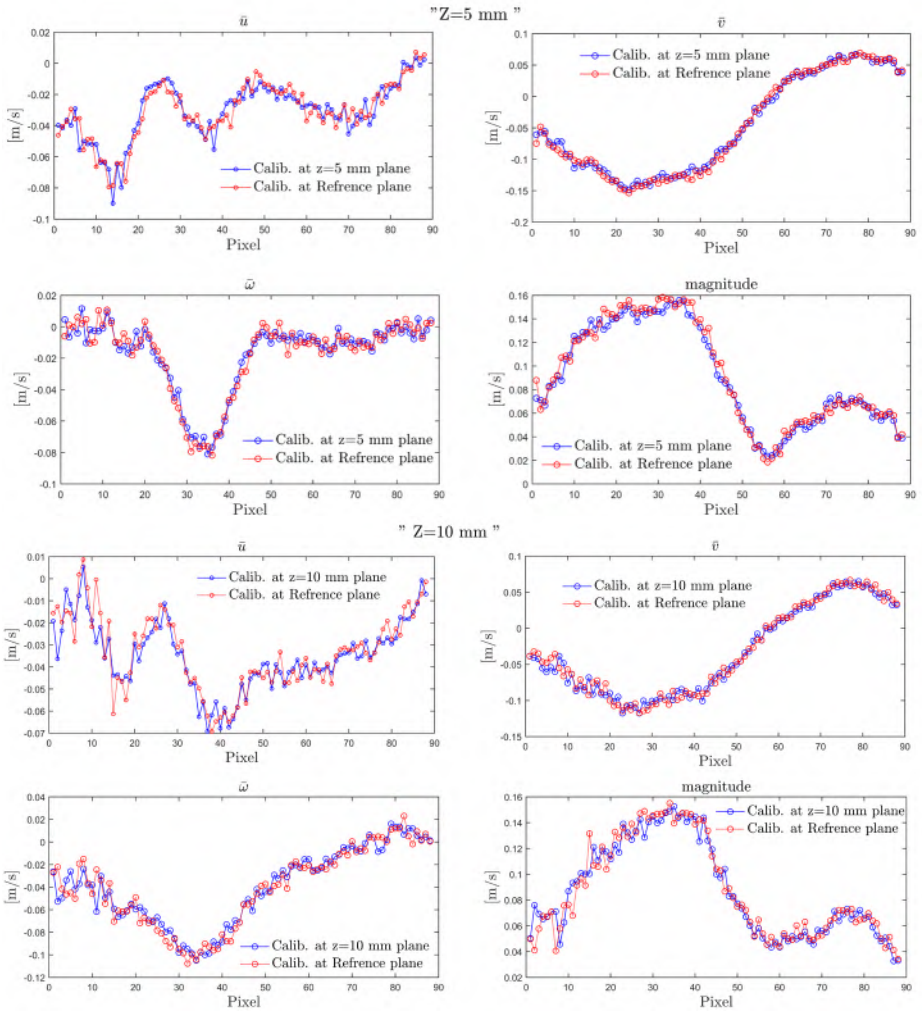


Figure 2-6: Comparison of the velocity components (u, v, w) and magnitude of the velocity vector obtained with classical calibration and single calibration methods. *Top:* $Z = 5 \text{ mm}$. *Bottom:* $Z = 10 \text{ mm}$.

2.3 RESULTS

All flow measurements were carried out under pulsatile flow conditions. In order to perform PIV measurements in a phase locked manner, the PIV acquisition system was triggered by a 5V signal generated by the pulsatile pump. To replicate realistic flow conditions (i.e. early and late LV filling, separated by a diastasis) a customized cardiovascular simulator has been used. The PIV acquisitions were started a few minutes after particles seeding and pump initialization. The main PIV processing parameters are summarized in **Table 2-1**. The time separation between two subsequent frames was set to of 950 μs , which results in a suitable particle displacement (8-10 pixels) in the range of flow velocities considered here. The choice of the cross-correlation window size has been optimized based on the robustness of the cross-correlation, namely the signal-to-noise ratio. The percentage of outlier identified by the universal outlier detection [80] gives an indication of the quality of the cross-correlation; for the results presented here, approximately 0.6% outliers were found in the instantaneous results. Moreover, the phase-locked acquisition strategy offers the possibility to further reduce the measurement errors by means of averaging velocity fields obtained with different distributions of the particle images within the cross-correlation regions. For the calibration of the imaging system and data processing a commercial software package was used (PIVview - PIV TEC GmbH, Göttingen, Germany). Matlab (MathWorks, Natick, MA) and Tecplot (Tecplot Inc, Bellevue, WA, USA) were mainly used for data analysis and visualization.

Table 2-1: Pre and post-processing PIV images parameters

Image pre-processing	<ul style="list-style-type: none">• Manual masking of non-flow regions• Background subtraction
Image sampling	<ul style="list-style-type: none">• Window size: 32x32 [px]• Step size 16 [px]• N° of vectors: 16129
Algorithm	<ul style="list-style-type: none">• Multi-grid interrogation (Grid refinement) 2 passes• Initial and final sampling: 128 px² \rightarrow 32 px²• Interpolation: B-spline 3rd order

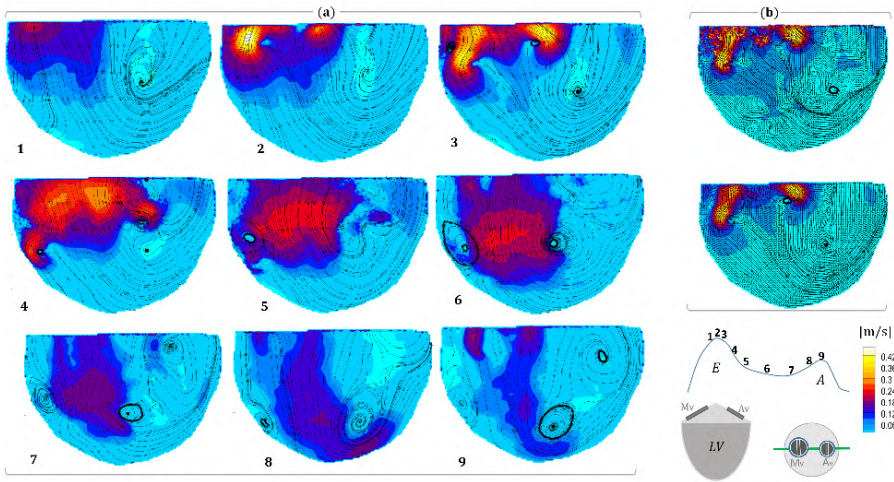


Figure 2-7: LV mid-plane measurements with the valve positioned in AO. **A** Sequence of nine phase-averaged velocity flow field during different diastolic time points at the mid-plane. **B** Instantaneous (top) and averaged (bottom) velocity vector field map at E-wave peak downstream mitral valve. The streamlines are superimposed on contours of the velocity magnitude

For each angular position, a full volumetric scanning measurement was performed at two key time instants, namely the early filling (E-wave peak) and the diastasis phase. To minimize the partial volume averaging due to the laser sheet thickness and volume oversampling, a spacing between consecutive planes equal to the illumination thickness (approximately 2 mm) was imposed.

The flow downstream the mitral was measured in the central plane of the LV at 19 time instants, distributed over the diastolic filling phase. *Supplemental movie 1 (Supplemental data for this article may be found on the Journal of experimental in Fluids: Springer website.) shows an animation of the velocity field.* **Figure 2.7a** presents a sequence of nine selected velocity maps which show the passage of the flow through the mitral valve, starting at the onset of the diastolic phase. The formation of transmitral jets through the bileaflet valve- with a stronger lateral jet toward the LV wall and aortic valve- is observed; this is due to the opening of the valve from outside. Then, the jets merge, occupying a large portion of the LV and travel towards the apical region. Consequently, the two generated jets induce two counter clockwise vortices within the LV before the start of the late filling phase. **Figure 2.7b** shows the comparison between the instantaneous velocity field and the time-averaged result obtained at the mid-plane during the E-wave peak. The phase-averaged velocity field shows the predominant flow structures that persist during the cardiac cycle as well as the smaller flow features that

survive the averaging of the instantaneous velocity fields recorded in phase-averaged fashion.

The full volumetric flow field in the two angular configurations of the mitral valve, relative to two instants in time (at E-wave and diastasis phase), are presented here. The multiplane measurements were performed at 30 parallel planes within the LV with a stroke volume of 50 ml. The 3D flow streamlines have been visualized using the Tecplot software by interpolating the data from neighbouring parallel velocity maps (using an inverse distance weighted interpolation method). The ensemble-averaged velocity field have been calculated, for each plane, from 30 instantaneous vector fields. **Figure 2.8a** depicts a side-by-side comparison between the 3D streamlines downstream the mitral valve at early filling. The 3D topology reveals the asymmetrical flow passing the mitral valve, providing additional information to the 2D 3C velocity maps shown in **Figure 2.7**. In **Figure 2.8b**, the 3D streamlines in the AO are closer to the LV wall and directed to the apex. As can be seen, the flow streamlines are more compact and occupy a smaller region in the AO.

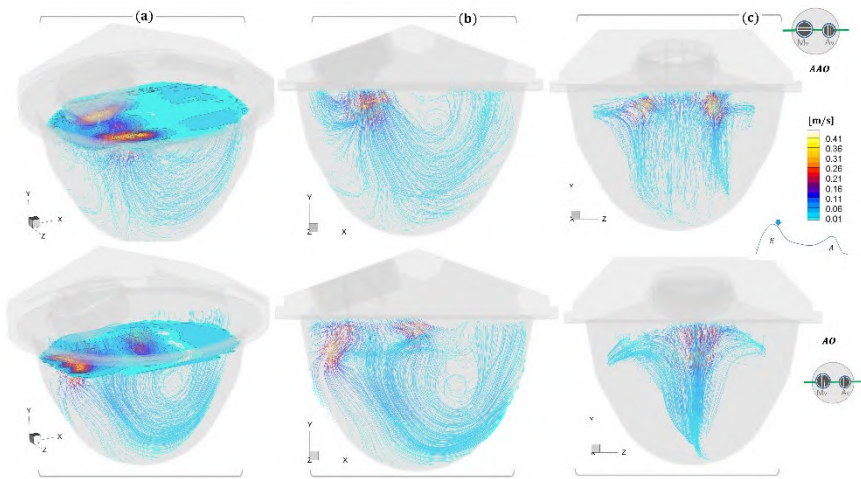


Figure 2-8: Comparison of the flow streamlines in the LV model in AO and AAO during E-wave peak. **a** Streamlines within the LV with a cross-plane section that show the jet positions; The 3D streamlines depicted in two different views, **b** YZ and **c** XY plane. Streamlines are colour coded based on velocity magnitude.

Figure 2.9 clearly illustrates the difference in vortex formation in mid region of the LV between the two angular orientations. In the AAO position the jets merge together before reaching the apex, peeling into two distinct counter-rotating vortices. In the AO, the flow is more elongated towards the apex and exhibits a less-defined vortical pattern. Nevertheless, in the out-of-plane direction, the 3D streamlines show a more compact

and organized flow in the AO. To better identify the intraventricular vortical structures, a Lambda-2 vortex detection method based on the velocity gradient tensor has been used (Jeong and Hussain 1995). The vortex is identified as a connected region with real negative eigenvalue λ_2 the decomposed velocity gradient tensor $S_{ij} + \Omega_{ij}$ (in which the strain tensor S_{ij} and vorticity part Ω_{ij} represent the symmetric and anti-symmetric part, respectively). Further insight of the flow dynamics was obtained by calculating the turbulent kinetic energy (TKE) and vorticity magnitude $\|\omega\|$, during the vortex formation. The vorticity vector ω is defined as the curl of the velocity vector; $\omega = \nabla \times \mathbf{V}$. The TKE is estimated as $TKE = 0.5 (\overline{u'^2} + \overline{v'^2} + \overline{w'^2})$, where $\overline{u'^2}, \overline{v'^2}, \overline{w'^2}$ are the averaged squared velocity fluctuation components.

Figure 2-10 compares the intraventricular TKE in several cross-planes during the diastasis phase. It can be observed that the level of TKE is similar in both orientations, with a wider distribution in the AO. This discrepancy may be due the opening of the mitral prosthesis toward the aortic valve. The vorticity magnitude map, highlights the difference in the vortex formation: the AO presents small vortices under the aortic valve and a wider vortex that is located closer to the apex when compared to the vortex generated in the AAO (**Figure 2.10b**). An iso-surface of λ_2 is shown in **Figure 2.10c**; both configurations present a vortex ring and, as mentioned above, the vortex generated in the AO is closer to the apical region than in the other configuration.

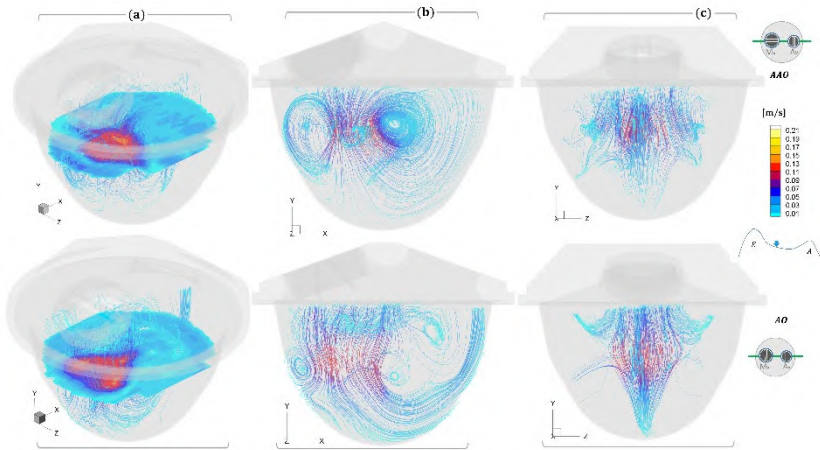


Figure 2-9: Comparison of flow streamlines in the LV model, in AO and AAO during diastasis. **a** Streamlines within the LV with a cross-plane section that show the jets positions **b, c:** different views of the 3D streamlines (YZ and XY planes respectively). Streamlines are colour coded based on velocity magnitude.

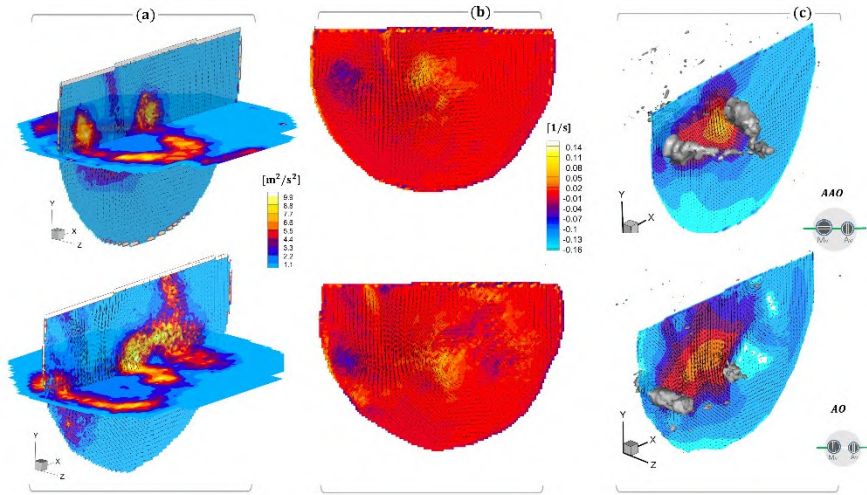


Figure 2-10: (a) Cross-plane sections within the LV; contours show the TKE values. (b) Vorticity magnitude in the mid-plane. (c) Contours of velocity magnitude in a cross-plane superimposed to the λ_2 iso-surface ($\lambda_2 = -0.0018$).

2.4 DISCUSSION

To illustrate the potential of the study, the aim was also to compare the flow downstream of a bileaflet mechanical valve mounted in two different angular positions. The setup is partly based on a previous works of Yagi and co-workers [77], [78] who developed a setup consisting of a single octagonal tank, open to the atmosphere and filled with sodium iodide, with movable window attached to the tank via flexible bellows. Scanning PIV was performed by translating the two cameras, the movable windows and the laser. A significant advantage of the present system is the additional possibility to enclose compliant models in a pressurized box. It ensures that the volume changes imposed by the piston pump only affect the geometry changes of the LV phantom. In case of flexible bellows, part of the volume change would also cause volume changes with the deformable bellows, thereby significantly altering the pump function of the LV.

The results from this study, supported by time-averaged velocity fields and vorticity maps, along with 3D streamlines and turbulent kinetic energy maps, revealed how the angular position of the bileaflet valve affect the multidirectional flow structure and turbulence statistics in a flexible LV model. The main findings of the present study agree with previous works, [70], [72], [82]–[85]. The evolution of the incoming jet in AO, confirms the finding of [70] and [86] where the septal jet generates a vortical

structure in mid region before reaching the LV apex. The lateral jets are stronger than the jet arising from the centre orifice, then the two jets generate vortices during deceleration phase of E-wave curve. The vorticity distribution in the AO shown in (Figure 2-10b) with a larger anterior expansion near the aortic valve has been also observed in [72], which may be explained by the opening from outside of the bileaflet valve that induce jet dispersion. The volumetric data extend our understanding of the effect of mitral valve orientation. In the out-of-plane direction the AO produced a more organized flow pattern and presented a vortex core closer to the LV apex. However, the AO yielded a larger TKE map compared with the AAO, which produces a smaller vortex ring and presents less vorticity under the aortic valve during the diastasis phase. From in vivo and in vitro, as well as computational simulations studies, it is well agreed that the orientation of the mitral valve is a significant determinant of the intraventricular flow pattern. However, is it not clear which is the optimal valve configuration yet. This is also shown in a number of contrasting opinions about the mitral valve performance in the different positions. Van Rijk-Zwikker et al have conducted a comparative ultrasound study and have indicated that the mitral valve in AO may lead to an abnormal intraventricular flow pattern [82]). Pierrakos et al have concluded that the AAO leads to a more favourable LV flow and presents a faster filling process compared to the AO [72]. In a numerical study, Choi et al have reported that the bileaflet valve in AO has superior performance in terms of leaflet motion [87]. On the other hand, the AAO produces lower regurgitation during the systole phase. The transvalvular mechanical energy loss was similar in both orientations. In a comparative (ultrasound versus 2D PIV) study, Westerdale et al have analysed three different orientations of a bileaflet valve, but could also not deduce an optimal configuration [88].

2.4.1 Setup limitations and future perspective

A number of practical limitations of the current setup can be identified and taken into account to improve the accuracy and impact of the results for future investigations. The silicon LV model has a slightly different (1.4) refractive index than the working fluid (1.49), which may affect the light path. Nevertheless, the relatively small thickness of the membrane (0.58 mm) reduces the impact of the refractive index difference.

Assuming a constant density of the working medium (incompressible fluid), the consistency of the PIV measurements has been evaluated computing the continuity equation $\nabla \cdot \mathbf{u} = 0$ (the centred difference scheme from Tecplot is used to estimate the velocity gradients). Figure 2.11 shows the contours of velocity divergence for an instantaneous measurement (Figure 2.11a) and for the result from the phase-locked sequence ensemble-averaging (Figure 2.11). Besides the expected border effects related

to both the cross-correlation analysis and the calculation of the spatial gradients, the largest values of divergence are located in the high vorticity regions, where stronger velocity gradients represent a challenge for the resolution of the PIV analysis. The beneficial effect of adopting an ensemble-averaging approach (enabled by the phase-locked strategy) is demonstrated by the reduction of the divergence error in the averaged result. A detailed analysis of a divergence-based correction scheme for Tomo-PIV data was presented [89]; the correction of the experimental results by means of enforcing a physical constraint (such as incompressibility) goes beyond the purpose of the present work and will be considered for future investigations. Due to optical requirements (refractive index matching) the resulting working fluid has a density (1750 kg/m^3) higher than blood. Hence, may have consequences on the leaflet dynamics of the mitral valve.

The intraventricular flow patterns and velocity magnitudes are influenced by the highly simplified geometry of the phantom. Moreover, the LV base diameter is approximately 1.5 times greater than an actual LV [90]. This explains the relatively low velocity values (approximately 0.3 m/s) within the LV. The fabrication of a more representative LV replica (with independent inlet and outlet tracts) based on medical images can be foreseen. Twisting motion (torsion) of the LV apex with respect to the base could not be achieved. However, in order for twisting to have an effect on LV flow, trabeculae (irregularly shaped muscular columns at the inner side of the LV wall) should be integrated into the LV wall. Due to the RI mismatch between the liquid and the LV membrane, the added material could significantly distort light paths and hence, the particle images. Furthermore, the region of $1 - 1.5 \text{ cm}$ downstream of the prosthetic valves was optically obscured (**Figure 2.3**), hampering the visualisation and analysis of valve leaflet kinematics and its relation with intraventricular flow.

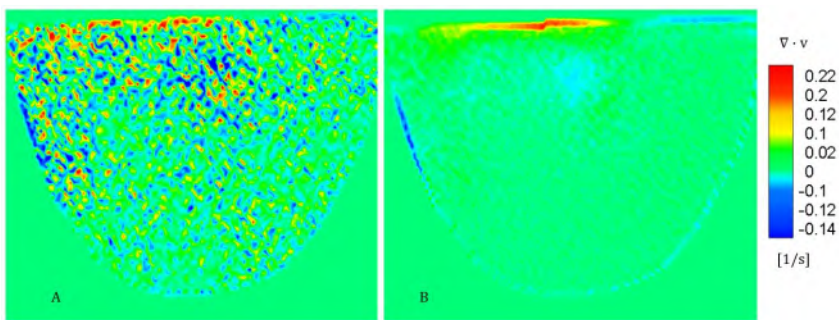


Figure 2-11: Color map of the velocity divergence of instantaneous (a) and ensemble-averaged (b) measurements.

The three components mixture that was used as index-matching fluid contains sodium iodide, which is not tolerated by biological valves. They experience dehydration leading to shrinkage of the valve leaflets. In addition, the fluid manifests a discoloration over time, which can be limited by adding sodium thiosulfate 0.1% (w/w) to the solution [91].

A complete volumetric flow analysis (with 30 planes) at a given time instant (averaging 30 cardiac cycle per plane) takes approximately 1 hour for the acquisition, of which 30 minutes PIV acquisitions and 30 minutes transfer of data on a workstation equipped with an Intel (R) core (TM) i7 CPU and 12 GB of RAM. Typically, each measurement was about 50 Gigabytes of raw data. The PIV images post-processing and 3D reconstruction phase require about 1 hour. Technically, the present setup can be easily converted to a time resolved system by replacing the camera and laser with high repetition counterparts providing an opportunity to obtain time varying flow velocities during an averaged cardiac cycle [92], and facilitating the reconstruction of the whole evolution of the vortices during the cardiac cycle.

2.4.2 Conclusions and outlook

The capability of an efficient scanning-stereo-PIV setup, composed of relatively low-end hardware and software when compared to truly instantaneous volumetric PIV techniques such as Tomo-PIV and 3D particle tracking, has been illustrated. The mechanical arrangement of the stereoscopic PIV apparatus leads to an alternative and robust system for high resolution velocity measurements, and proves its ability to reconstruct the 3D flow patterns in a deformable LV model in different physiological simulated conditions. The PIV system, cardiovascular simulator components and processing parameters have been described in detail. Also, the main limitations imposed by the current experimental conditions have been stated, together with possible solutions and improvements to be adopted in future investigations. We demonstrated its usefulness for reconstructing the volumetric LV flow field with different mitral valve angular configurations during the diastolic filling phase. Results obtained with the experimental setup presented here contribute to facilitate the interpretation of the complex LV flow dynamics and could be used as a reference for cardiovascular in vivo and numerical studies.

Tomographic PIV in a Model of the Left Ventricle: 3D flow Past Biological and Mechanical Heart Valves

*The contents of this chapter were published in
Journal of Biomechanics
(2019), vol. 90, pp. 40–49*

**Tomographic PIV in a model of the left ventricle: 3D flow past biological and
mechanical heart valves**

*H. Saaid, J. Voorneveld, C. Schinkel, J. Westenberg, F. Gijzen, P. Segers, P. Verdonck, N.
de Jong, J. Bosch, S. Kenjeres, T. Claessens*

Abstract: *To improve our understanding of intraventricular fluid mechanics and the impact of various types of prosthetic valves thereon, we have developed a custom-designed versatile left ventricular phantom with anatomically realistic moving left ventricular membrane. A biological, a tilting disc and a bileaflet valve (in two different orientations) were mounted in the mitral position and tested under the same settings. To investigate 3D flow within the phantom, a four-view tomographic Particle Image Velocimetry setup has been implemented. The results compare side-by-side the evolution of the 3D flow topology, vortical structures and kinetic energy in the left ventricle domain during the cardiac cycle. Except for the tilting disc valve, all tested prosthetic valves induced a crossed flow path, where the outflow crosses the inflow path, passing under the mitral valve. The biological valve shows a strong jet with a peak velocity about twice as high compared to all mechanical heart valves, which makes it easier to penetrate deeply into the cavity. Accordingly, the peak kinetic energy in the left ventricle in case of the biological valve is about four times higher than the mechanical heart valves. We conclude that the tomographic Particle Imaging Velocimetry setup provides a useful ground truth measurement of flow features.*

3.1 INTRODUCTION

The LV is believed to preserve the momentum of blood-flow from diastole into systole by keeping it in motion during diastasis, while smoothly redirecting blood towards the outflow tract during for ejection during systole [24], [25]. The filling phase is characterized by the formation of asymmetrical vortical structures induced by the interaction between the blood passing through the mitral valve and residual end-systolic blood flow [18]. The topology of these flow structures is determined by the geometry of the LV cavity, the morphology of the mitral valve and the electrical conduction system [2], [93].

The last twenty years have witnessed a growing interest in visualizing and quantifying LV flow dynamics in (patho-) physiological conditions using medical image techniques (MRI and ultrasound) [94], numerical simulations [16] and in vitro experiments [95]. Usually, the ultimate purpose of these multidisciplinary studies is to better understand the pathophysiology of heart disease, to define clinically useful indicators of cardiac function [25], [96] and/or to understand the effect of mitral valve repair or replacement by a prosthetic device on the LV flow [70], [72], [97], [98]. The choice of a biological vs. mechanical prosthesis for instance is still an open debate [99] as shown in a recent observational study by [100].

A well-established technique to study fluid dynamics problems in cardiovascular in vitro models is Particle Image Velocimetry (PIV). Specifically, planar PIV two-

dimensional (2D)-PIV has been extensively used to study the effect of different prosthetic valves on the LV flow pattern [72], [83], [92], [101]–[103]. A common limitation of these PIV studies is their 2D approach, yielding an incomplete view of the inherently 3D flow structures in the LV and the inability to calculate all nine components of the velocity gradient tensor. There have been various attempts to overcome this limitation by reconstructing the 3D velocity vector field in the whole LV from velocity data obtained from separate measurement planes. The latter are either two-component velocity [92],[104] or three-component velocity data, obtained by the stereoscopic PIV technique [108],[109]. Both reconstructive methods take advantage of the periodicity of the cardiac cycle but require complex setups to translate or rotate the PIV system as well as time-consuming calibration and/or post processing procedures.

Tomo-PIV is considered the first “true” volumetric PIV technique [49]. In contrast to traditional planar PIV techniques, Tomo-PIV allows instantaneous extraction of all three velocity components over the entire region of interest. To achieve this, the imaging system requires at least three simultaneous views of the volume-illuminated region. The particles are then reconstructed in 3D via mathematical algorithms [107] and the velocity vector field can subsequently be obtained via 3D cross-correlation [50]. To date, Tomo-PIV has been used for studying the blood flow in the aortic root [108], [109], the carotid artery [79] and the intracranial aneurysm [110].

Considering the above, the goal of the following work is twofold. First, we aim to demonstrate the feasibility of a tomographic, full-volumetric PIV technique to dynamically capture the 3D flow in a realistic and compliant LV model. Additionally, this phantom is compatible with 3D ultrasound and MRI imaging, such that 3D flow measurements acquired by these in-vivo medical imaging approaches can be compared to the optical ground truth in the future. Second, we compare the flow field generated by three structurally different prosthetic heart valves (biological, tilting disc and bileaflet) under the same running conditions. For this purpose, a LV shaped deformable membrane has been manufactured and immersed in an in house made plexiglas tank. The motion to the membrane was imposed by a commercial programmable pulsatile pump.

3.2 MATERIALS AND METHODS

3.2.1 Left ventricle membrane and tank

An optically transparent compliant silicone LV replica (**Figure 3.1b**) was manufactured by painting four layers of silicone (HT 33 Transparent LT, Zhermack SpA, Rome, Italy)

onto a 3D printed LV mould (**Figure 3.1a**). The shape of the LV mould was extracted from the statistical mean of a dataset of segmented 4D computed tomography images of 150 patients [111]–[113]. The segmented model represents the endocardial shape at end systole and is fitted with a mitral inflow and aortic outflow tract. The outflow tract is tilted about 40° with respect to the mitral valve axis. The thickness of the LV membrane is approximately 0.5 mm. The silicone has a refractive index of 1.413, measured by an Abbe refractometer (Bleeker, Zeist Holland).

The LV membrane was connected to the valve holders (**Figure 3.2**) using cable ties (**Figure 3.1c**), and immersed (**Figure 3.1d**) in a Plexiglas nine-sided polygon tank (Fig 2a). The Plexiglas plates were machined and then glued together using a two-component reaction adhesive (Acrifix 192, Evonic Industries). The shape of the tank was designed to provide undistorted optical access to the domain of interest from different angles. Fig. 2a depicts the LV flow loop, which consists of a pressurized aortic chamber and an atrial chamber kept at atmospheric pressure. The outlet from the aortic chamber is connected to the left atrial chamber via an adjustable peripheral resistance valve (Vivitro Labs Inc., Victoria, BC, Canada) with a short length of silicone rubber hose. **Appendix 1** provides some of the technical drawings of the LV phantom.

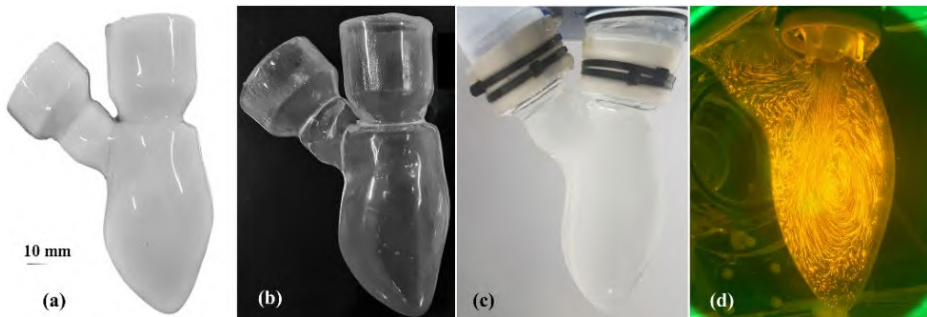


Figure 3-1: (a) and (b): 3D-printed mould and LV membrane. (c): LV model attached to valve holders. (d): A long exposure picture of fluorescent particles within the LV.

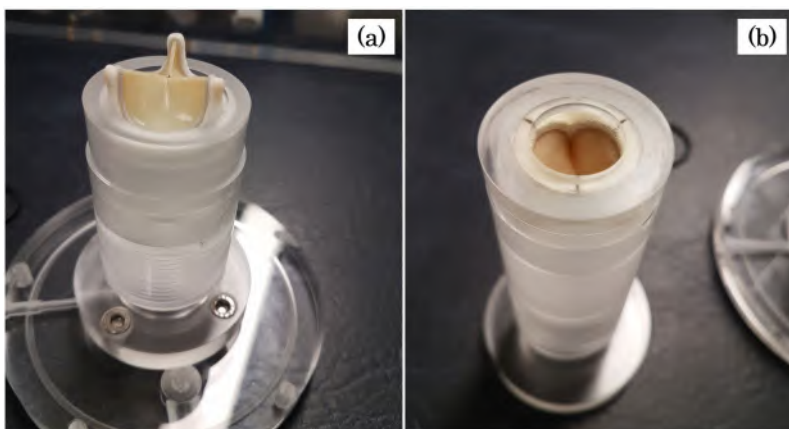


Figure 3-2: (a) Mitral and (b) aortic valve holders. Example with biological valves.

3.2.2 Hydraulic circuit

A commercially available pulsatile pump (Vivitro Labs Inc.) was used to drive and monitor the pumping action of the LV. The hydraulic piston pump was connected to the acrylic tank (**Figure 3.3a**) with semi-rigid tubing. The pump was velocity-controlled and set to generate a sinusoidal-like waveform with a frequency of 70 beats per minute and a duty cycle of 35%, resulting in a 300 ms systolic period and a stroke volume of 50 ml. Pressure transducers (6069, Utah Medical Products, Inc., Athlone, Ireland) were used to monitor the pressure in the aorta and inside the tank.

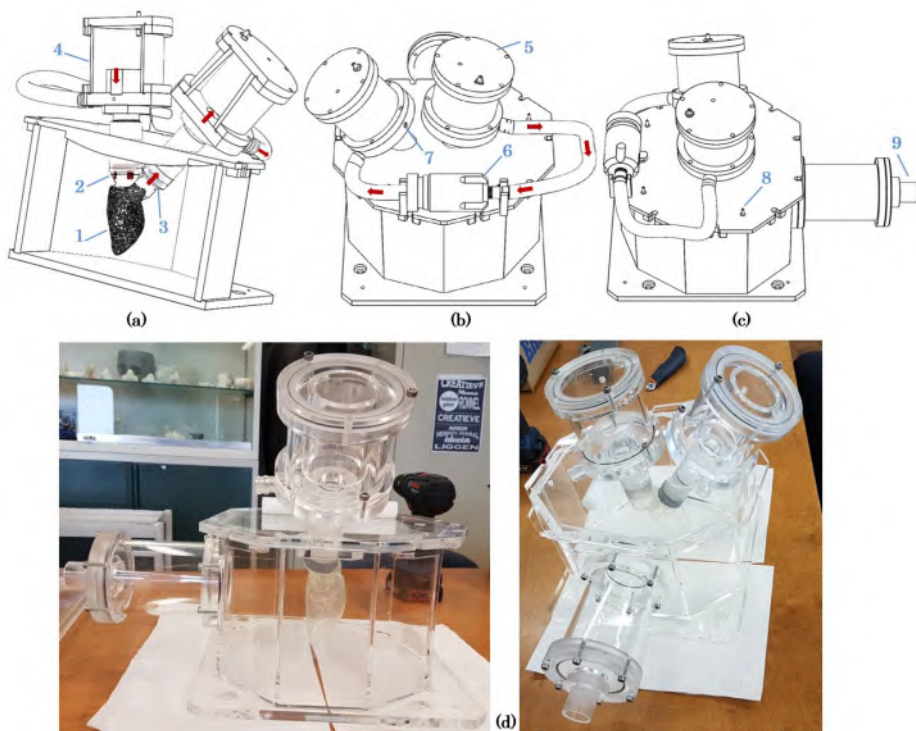


Figure 3-3: (a) CAD view of the nine-sided tank. *W* indicates the four windows used for optical access. The red arrows depict the LV flow loop. 1: LV model, 2-3: mitral and aortic valve holders, 4-5: atrium and aortic blocks, 6: Resistance, 7: aortic pressure catheter, 8: multiple hose connectors for air removal and ventricular pressure monitoring, 9: pump connector. (b) Representative samples of ventricular pressure recorded during the PIV experiments and flow waveforms imposed at the pump. (d) Photos of the phantom.

3.2.3 Imaging system and illumination volume

The imaging system consists of two high-speed CMOS cameras (Imager Pro HS 4M, PCO, Kelheim, Germany) with 4 megapixels sensor, set to record at 2000 fps (reached by cropping the sensor to the region of interest). The setup was primarily designed to perform Tomo-PIV from four different viewing angles using two cameras (Figure 3.4a). For this purpose, a custom-made image splitter (consisting of 8 first surface mirrors approximately $60 \times 120 \text{ mm}^2$) has been placed in front of each camera (Figure 3.4a-d). The mirrors have been placed between the camera and the tank, and manually adjusted in order to set the desired field of view and the optimal focus. To minimize the vibrations transmitted to the imaging system, the cameras were mounted on a tripod head with a load capacity of 12 kg (3D Super Pro 3-way, Manfrotto, Italy) and fixed on

rigid optical rails screwed to an optical table (Thorlabs, Inc., Newton, NJ, USA). Macro prime lenses with a focal length of 100 mm and maximum aperture of T3.1 (Samyang Optics co Ltd., Korea) were mounted on tilt adapters, which allows to meet the Scheimpflug criterion [114]. To be able to cover the whole measurement domain and to avoid the particle blurring effects due to limited depth of field, an aperture of $f/16$ has been set. A long-pass filter at 540 nm (Thorlabs, Inc., Newton, NJ, USA) was mounted in front of each lens to selectively capture the scattered fluorescent particle light.

Considering that the tomographic reconstruction accuracy is known to be affected by the imaging configuration [49], the cameras were arranged systematically in a linear composition with a tomographic angular aperture of 108° (angle between the outer cameras **Figure 3.4a**).

A volume of approximately $80 \times 110 \times 70 \text{ mm}^3$ was illuminated by a double-cavity pulsed Nd:YLF laser (527 nm Litron Laser, England) delivering 30 mJ/pulse (per cavity) with a repetition rate of 0.2-20 kHz. A combination of spherical and cylindrical lenses was used to shape the laser beam into a full-volume illumination. To create homogeneous illumination, a mechanical mask has been placed in front of the laser arm (**Figure 3.4c**). With the aim to increase the light intensity, the laser light was recycled by placing a mirror on the opposite side of the column.

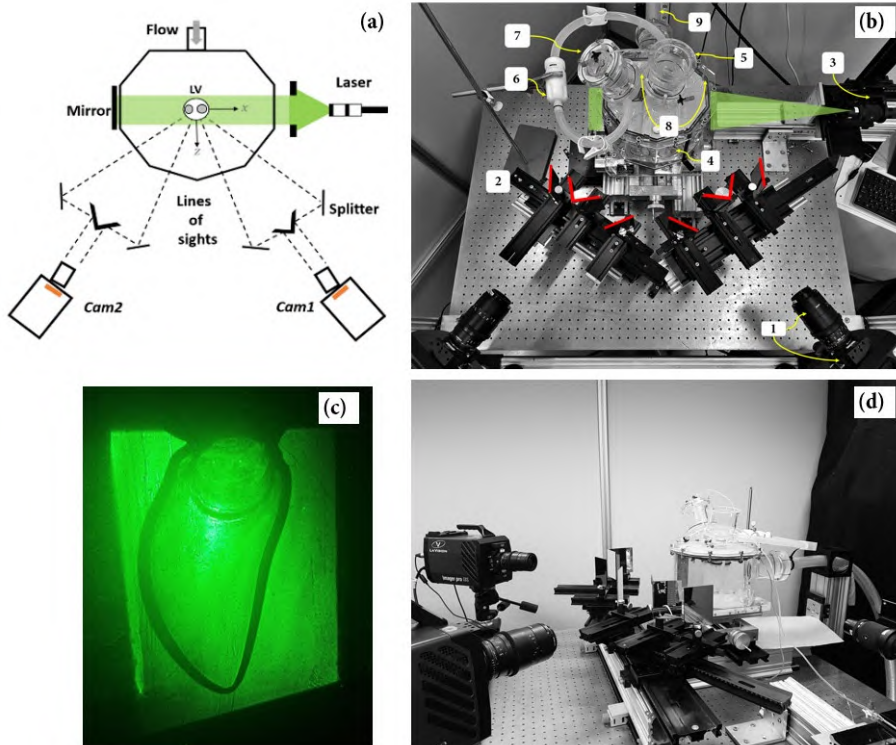


Figure 3-4: (a) Schematic sketch (top view) of the Tomo-PIV setup. (b): Picture of Tomo-PIV setup in linear configuration with two high-speed cameras equipped with prime lenses and filter (1), two mirror splitter system (2) and laser arm with telescopic head and optics compound (3). The ten-sided tank (4), with atrium (5) and aortic blocks (6), connected with peripheral resistance tube (7). Pressure transducer tubes (8). The tank is connected to the pulsatile pump via semi-flexible tube (9). (c): Projection of LV illumination (d): Lateral view of the setup.

3.2.4 Working fluid and tracer particles

A two-component mixture was used inside the LV loop and the acrylic tank. The working fluid was chosen to match the measured refractive index (1.4130) of the LV silicone membrane, thereby minimizing optical distortion (**Figure 3.5**). The ratio of the components in the fluid mixture (60% glycerol and 40% distilled water) was adjusted until its measured refractive index (1.4140) very closely matched that of the silicone. The dynamic viscosity and density of the working fluid were 17.7 mPa·s and 1160 kg/m³, respectively. Fluorescent Rhodamine-B coated particles with a diameter of 20-50 μm and density of 1100 kg/m³ were used as tracers.

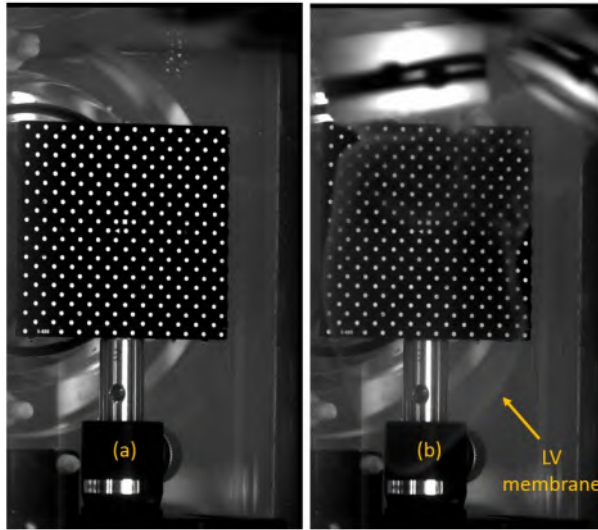


Figure 3-5: a) Calibration plate placed within the tank. b) LV membrane positioned in front of the target.

3.2.5 Calibration and volume self-calibration

The Tomo-PIV reconstruction required a very precise physical calibration: ideally the error of calibration should be less than 0.1 pixel. To this purpose, a two-level calibration plate with circular markers distributed uniformly with an interval of 10 mm has been used. To ensure equidistant and coplanar views, the calibration target was placed with a micrometre stage in nine positions equally spaced over 40 mm in the tank (**Figure 3.6**). To map the 3D space object onto the 2D camera sensor plane, a third-order polynomial fitting method was applied. The geometrical calibration yielded an average error for all cameras and views of approximately 0.2 pixel. Due to the physical constraints, the calibration has been performed outside the LV membrane. Yet more importantly, the volume self-calibration became a crucial step to correct the mapping function. An ensemble of 200 particle images has been acquired to perform the iterative volume self-calibration procedure [61]. Prior to the self-calibration, the images were pre-processed by a history-minimum-background subtraction [50] and intensity normalization. The volume domain has been subdivided in $8 \times 8 \times 5$ sub-volumes. At the first step, the averaged disparity vector magnitude was about 0.5 pixel. After four iterations, the volume self-calibration was able to reduce the disparity to less than 0.02 pixels for all cameras.

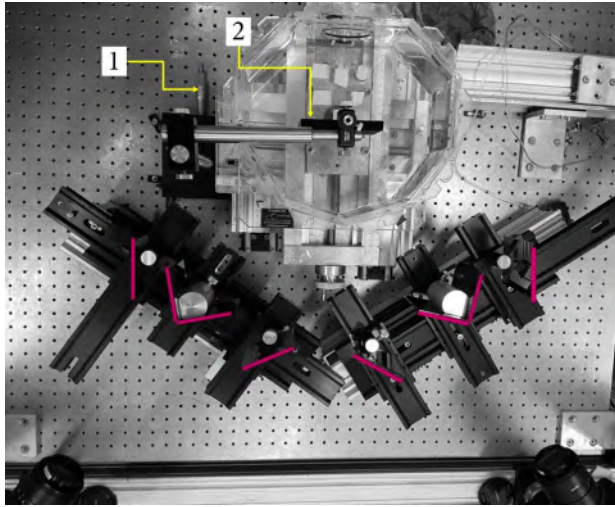


Figure 3-6: Top view of the setup during calibration procedure. (1) Micrometre stage (2) Calibration plate.

3.2.6 Tomographic analysis

All particle images were pre-processed to remove background intensity with a 7×7 sliding minimum kernel. Due to the Gaussian laser illumination shape, an intensity normalization filter was applied. Subsequent image processing involves 3×3 Gaussian smoothing, successive sharpening and manually masking out the non-flow regions. The concentration of the particles within the domain has a direct effect on the ability to reconstruct correctly the 3D particle distribution and to perform a robust cross-correlation analysis. Following the suggested particle concentration from literature [50], and considering that the present tomographic setup is a linear arrangement with four camera views, for all measurements, a concentration of 0.04 particles per pixel (PPP) has been reached as an optimal measurement condition. The time separation Δt of $500 \mu\text{s}$ between image-pairs was optimized to ensure that maximum particle displacement is about 6-10 pixels. All data post-processing, calibration, self-calibration steps and tomographic analyses have been performed using Davis 10 (LaVision, Göttingen, Germany).

3.2.7 Measurement protocol

In this paper, the volumetric PIV measurements have been performed within the LV with three different heart valves mounted in the mitral position (**Figure 3.7a**): a 25 mm tricuspid biological Perimount 2900 (Edwards Lifesciences, Irvine, USA), a 24 mm

tilting disc (Björk-Shiley) and a 25 mm Bicarbon bileaflet valve (Sorin Biomedica, Saluggia, Italy) which was mounted in two different orientations (anatomic and anti-anatomic). In all series a 19 mm Perimount Magna Ease (Edwards Lifesciences, Irvine, USA) tricuspid biological valve was used as an aortic valve. The particle images were reconstructed at 61 time points over the cardiac cycle (temporal resolution of 14 ms). The data from ten cardiac cycles were phase-averaged for each heart valve configuration. **Table 3-1**, summarizing the relevant setup and processing parameters.

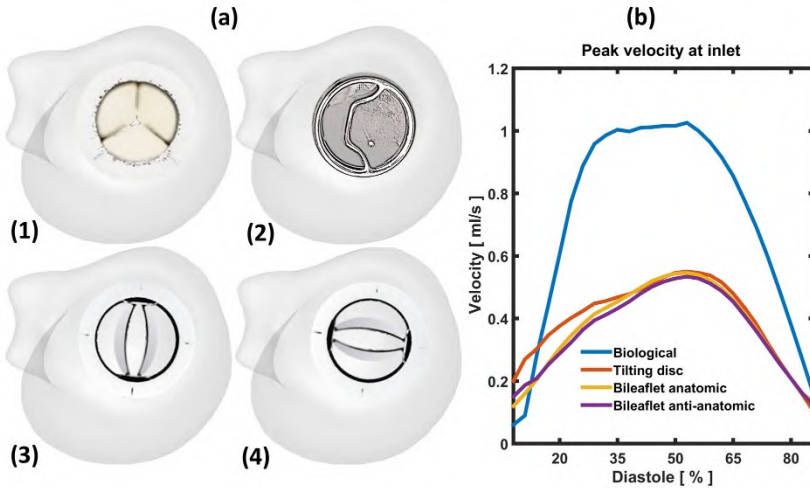


Figure 3-7: (a) Snapshots of the LV model and heart valves in the mitral position: (1) biological; (2) tilting disk; (3-4) bileaflet in anatomic and anti-anatomic orientation, respectively. (b): peak velocity of the inflow jet during the diastolic phase.

Table 3-1: An overview on the most important parameters for the PIV system, hydraulic setup and Tomo-PIV analysis

Imaging	Sensor	CMOS
	Resolution & dynamic range	2016x2016 pixel, 12bit
	Pixel size	11 μm
	Acquisition rate	2 kHz
	Exposure time	20 μs
	Lens focal length	100 mm
	Lens aperture	16
	Field of view	90*50*40 mm ³
	Max. Particle displacement	6-10 pixel
	Digital image resolution	12.4 pixel/mm
Type	Nd:YLF	
Pulse width	~100 to 150 ns 200 μs	
Pulse distance	200 μs	

Laser	Volume illumination	80*110*70 mm ³
	Total laser energy	44 mJ at 2 KHz 90*110*65
	Illuminated volume	90*110*65
Seeding	Type	Rhodamine-B
	Diameter	20-50 um
	Density	1100 Kg/m ³
Fluid	Mixture	60% Glycerine, 40% Water
	Refractive index	1.413
	Density	1160 kg/m ³
	Dynamic viscosity	17.7 mPa·s
Prosthetic valves	Aortic	Biological tricuspid 19 mm
	Mitral	Biological tricuspid 25 mm
		Bileaflet curved leaflet 25 mm
		Tilting disc 24 mm
Flow parameters	Heart frequency	70 BPM
	Stroke volume	50 ml
	Peak LV pressure	150 mmHg
	Peak Aortic pressure	150 mmHg
Tomo-PIV	Volume size	62*100*57 mm (x,y,z) 760*1226*699 voxels
	Particle density	0.04 PPP
	N° of iterations	8
	Correlation	96-48 voxels
	N° of passes	4
	Overlap factor	75%
	Spatial resolution	0.98 mm
	N° of vectors	63*102*58

3.3 RESULTS AND DISCUSSION

In the following, the Tomo-PIV phase-averaged velocity data are presented. The first subsection illustrates the mean flow velocity field downstream of the four prosthetic valves. Further, we focus on the inflow characteristics by comparing the flow rate through transversal slices over time. In the last two subsections, we present the vortical structures and kinetic energy computed in the entire LV domain. The figures have been produced using Tecplot 360 (Tecplot, Inc., Bellevue, WA), DaVis 10 (LaVision, Göttingen, Germany) and Matlab (MathWorks, Natick, MA).

Figure 3.7 compares the maximum inlet flow velocity between the four valves. The

biological valve (BHV) opens slightly later than the mechanical valves (MHVs) and the transmitral flow velocity increases more rapidly for the BHV, reaching a peak value of up to 1 m/s - twice the magnitude of the MHVs. At the onset of the diastole, the tilting disc produces slightly higher velocities than the two bileaflet configurations. The two orientations of the bileaflet valve yielded virtually identical inlet velocities throughout diastole.

3.3.1 Flow Velocity field

A note of caution is necessary, because of the large difference in the flow velocity range between the biological and mechanical valves (**Figure 3.7b**), different colour scales were used for the iso-surfaces and velocity maps (**Figure 3.8**). **Figure 3.8** shows the mean flow topology of the tested heart valves (indicated with letters) at four characteristic phases (indicated with Roman numerals) during the cardiac cycle. The flow topology is represented by means of iso-surfaces based on the velocity magnitude and cross-sectional slices coloured with axial velocity.

Biological valve: Initially, a strong transmitral jet is directed towards the anterior LV wall (time steps I-II). By the end of diastole (time step III), the inner core of the inflow starts disappearing (high velocity isosurface). Further, the inflow swirls towards the posterior wall, forming a counter-rotating flow pattern occupying the entire LV cavity. This flow feature is believed to prevent blood stasis by washing-out the apical region. The outgoing flow slides along the posterior wall of the LV crossing the inflow tract (time step IV). The crossed flow path shown here with the BHV (dashed line **Figure 3.8**) agrees with previous *in vivo* studies [70], [97], [98], where the flow passing the BHV was shown to generate a strong jet towards the intraventricular septum and then to cross the inflow path (i.e. passing under the mitral valve) during systole (**Figure 3.8a**).

Monoleaflet valve: At the onset of the filling phase (time step I) the valve induces a primary jet passing the main orifice. The primary jet advances along the posterior wall, while a secondary jet passes from the anterior orifice towards the anterior wall (time step II). At the end of diastole, the incoming flow forms a clockwise large-scale vortex (time step III) that is smoothly redirected towards the LV outflow tract. This looped flow path is in concordance with previous 2D-PIV investigations [113], [115]–[117].

Bileaflet valve: The two valve orientations exhibit minor differences in flow topology at the onset of the filling phase (**Figure 3.8****Figure 3.8c-d**): in both cases the jet emanating from the outer orifices is significantly stronger than in the central orifice (time steps I-II). In the anatomic configuration (**Figure 3.8c**), the jet on the anterior wall septum rolls off under the aortic valve, whereas due to the “Coandă effect” the opposite jet tends to realign with the central inflow jet (time steps II-III). In the anti-

anatomic orientation (d), on the other hand, the flow pattern through the outer orifices appears to be nearly symmetric (time steps II-III). In both configurations, at mid diastole the strong central jet merges with the outer jets towards the apex. The iso-velocity surface emanating from the mitral valve dissipates before reaching the apex (**Figure 3.8c-d**), as previously described in [72]. Additionally, our results indicate that in both configurations the bileaflet valve gives rise to a crossed flow path. This confirms the findings from a prior in vivo study from [70]. Conversely, [118], using an ultrasound based vector flow mapping technique, showed that only the anti-anatomical orientation is associated with a crossed flow path. In our previous chapter 2, we even observed that both orientations lead to a looped flow path. Some of the discrepancies may be due to the highly simplified LV shape and the different LV diameter/valve ratio [106] or a limitation of two-dimensional echocardiography in case of [118]. *Movie 1 (as online supplement on the journal of Biomechanics) depicts the flow field throughout one cardiac cycle for each valve model.*

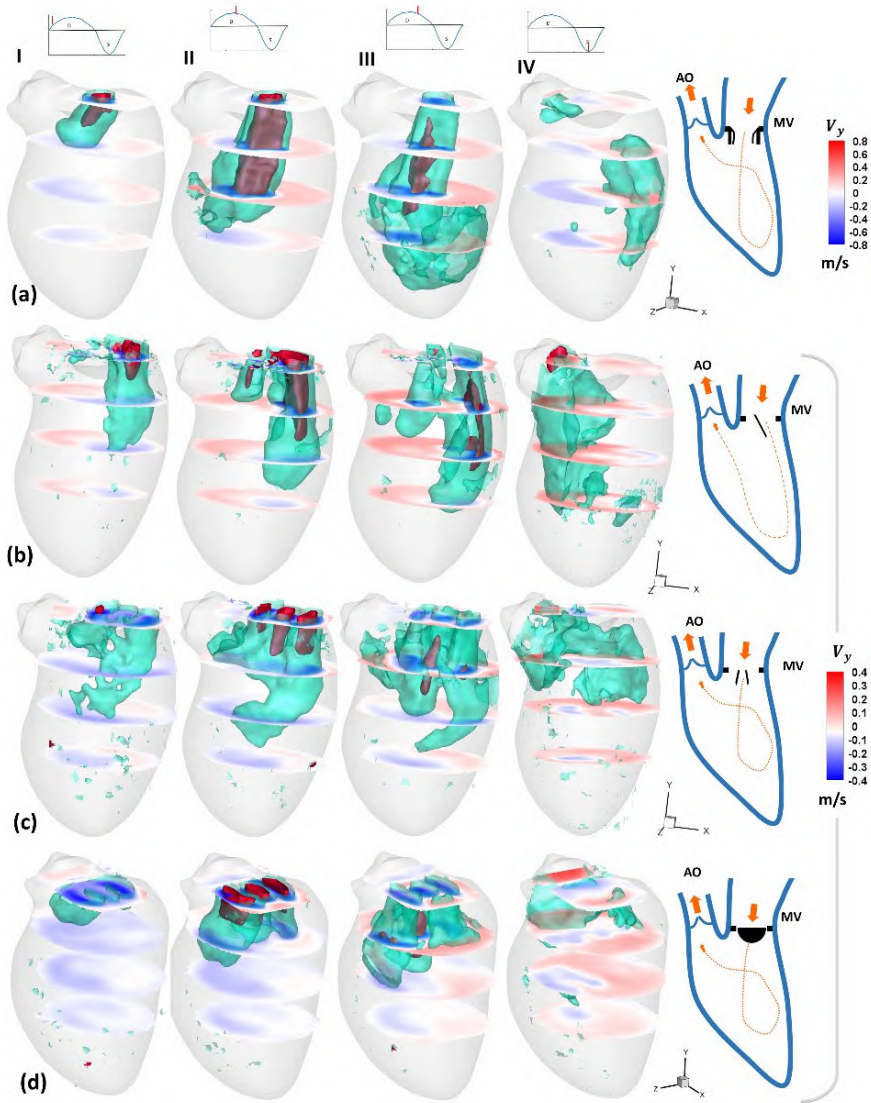


Figure 3-8: Time-sequence of the mean flow structures downstream of the mitral valves: (a) biological, (b) tilting disc, and bileaflet in (c) anatomic and (d) anti-anatomic orientation. Note that (d) is slightly rotated about the y -axis to improve visibility of the flow structures. Two isovelocity surfaces are shown for each valve (at 0.35 m/s and 0.75 m/s in case of the BHV and at 0.15 m/s and 0.35 m/s in case of the MHVs). On the right, a simple sketch of the LV and prosthetic valve showing the flow path (looped or crossed) with a dashed line. The cross-sections are colour-coded based on the axial velocity (v_y). Roman numerals indicate the time steps (I=0.35s, II=0.55s, III=0.8s, IV=0.2s).

3.3.2 Inflow characteristics

For a more quantitative comparison between the BHV and the MHVs, the volume flow rate has been calculated through four cross-sections (**Figure 3.9**) over one cardiac cycle. The flow rate was computed as numerical integration of the velocity vector field over transversal cross-sections, and only the downward flow (y -axis) was considered. As shown in **Figure 3.9** (cross-section 1), the three mechanical valves open simultaneously, in agreement with the information deduced from **Figure 3.7**. The two bileaflet orientations behave similarly in the first slices with a slightly higher flow rate than the biological and the tilting disc valves during the diastole. Moving towards the apex, in cross-sections 3 and 4, the penetration depth of the jet decreases drastically in the MHVs. In fact, the BHV exhibits a much higher downward flow over the filling phase compared to the bileaflet valve in anatomic configuration (cross-section 4). The stagnation phenomena in a LV have also been reported in a 2D-PIV investigation by Faludi and co-workers [70], showing that the jet entering the LV cavity collides more closely to the apex with a biological valve than with a bileaflet valve. Compared to the MHVs, the inflow jet through the BHV is more likely to reach and wash out the LV apical region. This potentially avoids stagnation zones and reduces the risk for thrombosis formation. In patients with dilated cardiomyopathy or myocardial infarction, where abnormal flow patterns are known to promote blood stasis between the apex and outflow tract [119]–[121], we would expect the BHV to perform better than the MHVs.

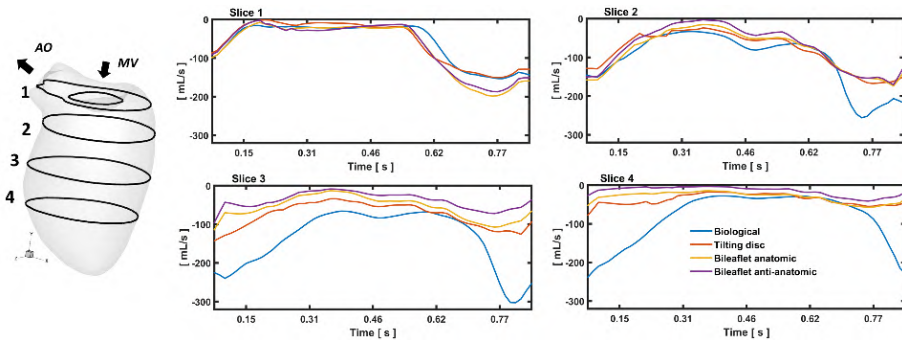


Figure 3-9: Left: Four equidistant (20 mm) cross-sections within the LV model. The first slice is positioned approximately 5 mm below the mitral valve. Right: Volume flow rate computed through four cross-sections for each valve. Only the downward flow was considered; velocities with a positive sign (v_y) were blanked. The MHVs open approximately at 0.54s and the biological at 0.58s instead.

3.3.3 Vortical structures

The lambda-2 (λ_2) method has been used to identify the 3D vortical flow features over the cardiac cycle [81]. Briefly, the λ_2 enables vortex structures to be recognized in the flow field by decomposing the velocity gradient tensor into its symmetric (\mathbf{S} : rate-of-strain tensor) and anti-symmetric ($\mathbf{\Omega}$: vorticity tensor) components. The $(\mathbf{S}^2 + \mathbf{\Omega}^2)$ entity has three eigenvalues in the following order ($\lambda_1 > \lambda_2 > \lambda_3$). The vortex structure is defined as the connected regions in the flow field where λ_2 is negative.

In **Figure 3.10**, one can clearly see the formation of the vortex rings (time step I) and observe how they elongate, propagate and then dissipate during diastole. The strong inflow through the biological valve develops as a single vortex ring in the shear layer around the incoming jet (time steps I-II-III). The primary vortex ring is connected to a secondary vortex via branched tubes (trailing vortex tubes). The two vortices travel towards the mid-ventricle and start to break down in small structures before reaching the LV apex. The described vortex ring formation downstream the BHV is somewhat similar to the vortices generated from a cylinder with an inclined exit [122]. Comparable flow structures have also been described in previous LV fluid dynamic simulations [123]–[125] and *in vivo* studies [126].

The three MHVs exhibited different vortical flow features compared with the BHV. In case of the tilting disc, the flow through the posterior orifice yields a strong shear layer and interacted with the boundary layer along the lateral wall generating a curved vortex ring (**Figure 3.10b**). The vortical structures then shed from the valve leaflets, progress toward the mid regions, and finally dissipate by the end of the diastole due to viscous interaction with the ventricular wall.

Due to the leaflet geometry of the bileaflet valve, the inflow is spread over multiple orifices, rendering the formation of a single vortex impossible. Thus, the bileaflet valve induces incomplete vortex rings through the three orifices (**Figure 3.10c-d**). At the onset of the filling phase, the flow is dominated by tubular structures generated from the outer orifices. Further into diastole (time step IV), a jet is formed from the central orifice with higher propagation velocity, forming a concentric coherent structure. The latter interact rapidly with each other and with the surrounding LV wall, disintegrating into smaller flow structures. Additionally, the so-called vortex ring was observed only downstream the biological valve with the formation of multiple vortex rings. *The complete evolution of the vortical flow structures past the prosthetic heart valves over the cardiac cycle is provided as a supplementary material (video 2).*

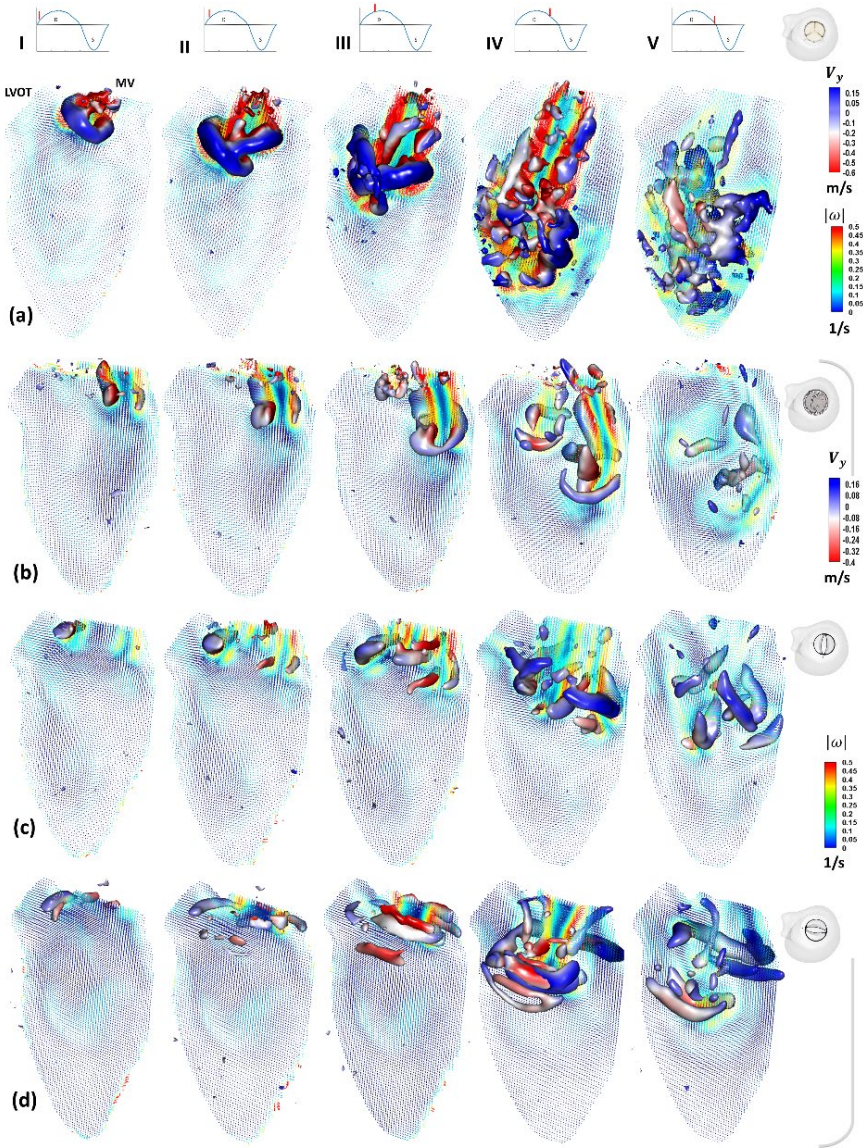


Figure 3-10: 3D vortical structures recognized by lambda-2 method are visualized as iso-surface ($\lambda_2 = -0.015$) and colour-coded with the axial velocity component. The 2D velocity vector field maps are coloured based on vorticity magnitude. (a) Biological, (b) tilting disc, and bileaflet in anatomic (c) and anti-anatomic (d) orientation. Roman numerals indicate the time steps (I=0.35s, II=0.45s, III=0.55s, IV=0.65s, V=0.85s).

3.3.4 Kinetic energy

The time course of integral kinetic energy (KE) computed for the entire LV domain is shown in **Figure 3.11**. The peak value of the kinetic energy passing the BHV is approximately four times higher than for the MHVs, as could be expected from the two-fold difference in the velocity magnitude profile during the cardiac cycle (**Figure 3.7**). A significant difference in terms of KE between BHV and bileaflet valve has been also reported in a recent numerical study by [127]. All mechanical valves exhibit a similarly shaped KE profile throughout the cardiac cycle. The tilting disc leads to higher KE levels during mid diastole and systole than did the bileaflet valve. In case of the bileaflet valve, the anatomic orientation yielded a slightly higher KE than the anti-anatomic configuration.

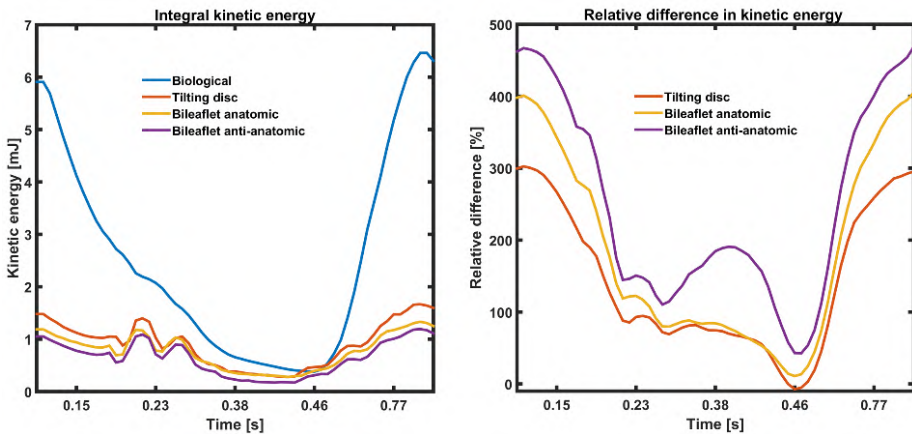


Figure 3-11: Left: the evolution of the kinetic energy within the LV domain, computed over the cardiac cycle as: $KE = 0.5\rho \int V^2 dv$, where $\rho = 1060 \text{ kg/m}^3$ and V is velocity magnitude. Right: The difference of KE in the biological valve relative to each of the mechanical valves, calculated as: $100\% * (BHV - MHV_i) / MHV_i$.

3.3.5 Limitations

Despite the aforementioned advantages of the employed technique, some limitations are worthwhile mentioning. Tomo-PIV hardware and software are generally more complex and expensive than 2D PIV or multiplane scanning setups. However, in order to reduce the cost of the PIV apparatus, a four-view Tomo-PIV imaging system has been implemented using a combination of only two cameras (instead of four) and a mirror system. Also, while Tomo-PIV does not require physical alignment between illumination and the calibration target, it is more sensitive to vibrations compared to

stereoscopic PIV, which may lead to camera misalignment during the acquisition. To overcome this, we followed a well-established procedure for physical calibration, followed by the correction of the camera's mapping functions which has been performed before and after each measurement (volume-self calibration). Due to computational cost and amount of data storage, we have presented only the averaged flow field data based on 10 cycles. A semi-quantitative convergence analysis (consisting of a comparison between the phase averaged data obtained from 10, 20 and 30 cycles) showed no discernible difference between 20 and 30 cycles. Only at peak early inflow a 7% difference in flow velocity was found between the results obtained with 10 cycles and the converged flow velocity data using 30 cycles (**Figure 3.12**). Moreover, we would like to mention that more advanced Lagrangian software algorithms, such as Shake-The-Box (Schanz et al. 2016), may be more appropriate to analyse the time-resolved data in the near future. Furthermore, the piston pump was driven by a sinusoidal-like wave form that does not represent diastasis and the late filling (A-wave). Due to the absence of this A-wave, it was not possible to investigate the interaction between the flow structures induced at the early filling and the fresh fluid entering during the late filling wave, as described in vivo [126] and in a recent numerical simulation study [117], using a similar LV geometry and a more realistic flow waveform. Also, the working fluid mixture has a dynamic viscosity four times higher than blood, which may have affected the flow resistance and consequently the formation and viscous dissipation rate of the vortical structures. Additional features that may affect the intraventricular flow include the inability to replicate the twisting/torsion movement of the LV chamber during contraction and the absence of anatomical elements such as the papillary muscles and the endocardial trabeculae. The latter had to be omitted in this study for optical purposes.

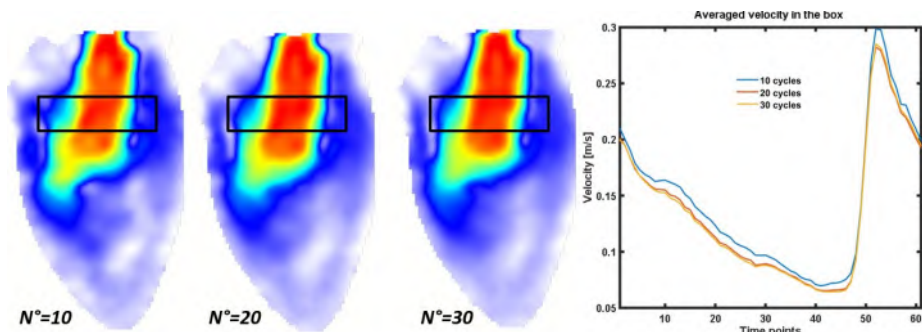


Figure 3-12: Left: cross-section of velocity vector field averaging 10, 20 and 30 cardiac cycles. Right: Comparison of the temporal evolution of the averaged velocity calculated in the black box.

3.3.6 Conclusion

This work demonstrated the feasibility and usefulness of Tomo-PIV, a full-volumetric optical flow measurement technique, to study flow dynamics in a compliant model of the LV. To the best of our knowledge, this study provides the first Tomo-PIV study of the 3D flow pattern in a flexible LV shape membrane, downstream of biological and mechanical valves. The proposed experimental setup serves as a suitable validation tool for emerging medical techniques and numerical simulations.

We have analysed the effect of three types of prosthetic mitral heart valves on intraventricular flow under the same hydraulic conditions. The qualitative and quantitative flow analyses suggest that the biological valve generates flow patterns similar to those observed *in vivo* after a BHV valve replacement. Except for the tilting disc, all tested prosthetic valves induced a crossed flow path, where the outflow crosses the inflow path, passing under the mitral valve. Further, the inflow jet in the BHV penetrated deeper into the LV cavity compared to the MHVs. The lambda-2 method for vortex identification showed the formation of multiple vortex rings in the presence of the BHV. The kinetic energy level associated with the BHV during diastole is approximately four times higher than the MHVs. Finally, we showed that the anatomic orientation of the bileaflet valve yields an overall slightly higher kinetic energy than the anti-anatomic configuration. Yet, none of our performed analyses reveal that one orientation of the bileaflet valve is to be preferred over the other.

4D Echo-Particle Image Velocimetry in a Left Ventricular Phantom

*The contents of this chapter were submitted to
Ultrasound in Medicine and Biology*

4D Echo-particle image velocimetry in a left ventricular phantom
*J. Voorneveld, H. Saaid, C. Schinkel, N. Radeljic, B. Lippe, F. J. H. Gijzen, A. F.W. van
der Steen, N. de Jong, T. Claessens, H. J. Vos, S. Kenjeres and J. G. Bosch*

Abstract: Left ventricular (LV) blood flow is an inherently complex time-varying 3D phenomenon, where 2D quantification often ignores the effect of out-of-plane motion. In this study we describe high frame rate (HFR) 4D echo-Particle Image Velocimetry (Echo-PIV) using a prototype matrix transesophageal transducer and a dynamic LV phantom for testing the accuracy of Echo-PIV in the presence of complex flow patterns. Optical time-resolved tomographic PIV (Tomo-PIV) was used as a reference standard for comparison. EchoPIV and tomoPIV agreed on the general profile of the LV flow patterns but Echo-PIV smoothed-out the smaller flow structures. Echo-PIV also underestimated the flow rates at greater imaging depths, where the PIV kernel size and transducer point-spread-function were large relative to the velocity gradients. We demonstrate that 4D Echo-PIV could be performed in just four heart cycles, which would require only a short breath-hold, providing promising results. However, methods for resolving high velocity gradients in regions of poor spatial resolution are required before clinical translation.

4.1 INTRODUCTION

Left ventricular (LV) blood flow patterns are of increasing interest in the study and early diagnosis of LV dysfunction, with particular focus on the trans-mitral jet and its resulting intra-ventricular vortex dynamics [9], [128]–[132]. Currently, the primary *in vivo* techniques used for studying LV flow dynamics are phase-contrast magnetic resonance imaging (PC-MRI) and echocardiography.

PC-MRI has the advantage of being able to measure flow patterns in 3D (often called 4D-Flow MRI) and not requiring contrast agent injection, but requires long acquisition times (averaging over hundreds of cardiac cycles), expensive infrastructure and equipment and suffers from low temporal resolution (only acquiring 20-30 phases per cardiac cycle) [8].

Alternatively, clinically available echocardiographic blood flow imaging techniques are bed-side and can be acquired at 15-100 frames per second; but are currently limited in the flow components that can be measured. Pulsed-wave Doppler can accurately measure blood velocities, but only the velocity component parallel to the ultrasound beam (axial) and in a small interrogation-region at a time. Alternatively, color Doppler can visualize blood flow over a region in 2D, but again only the axial velocity component. Also, aliasing is common when high velocities are present. As LV blood flow patterns are inherently 4D (time-varying 3D), echocardiographic techniques that can estimate 4D blood flow patterns, resolving all 3 spatial components, are required.

Some experimental ultrasound techniques have emerged to address the need for 4D blood flow measurement. For instance, vector Doppler, estimates the lateral velocity components by using multiple angled Doppler acquisitions [133]. Similarly, transverse oscillation estimates lateral displacement by introducing a lateral modulation into the received signal [134], [135]. However, transverse oscillation and vector Doppler require larger apertures for greater depths of interest, which is difficult with cardiac imaging due to the small intercostal windows available.

Alternatively, vector flow mapping calculates lateral velocity components from color Doppler acquisitions and segmentations of the LV wall using a model based approach [136], [137]. Gomez et al. (2015) demonstrated a 4D implementation of this technique in pediatric patients using multi-beat acquisitions of color Doppler and B-Mode imaging sequences [138]. Grønli et al. (2018) expanded this method to adults with the addition of a hybrid blood-speckle tracking and Doppler estimator to circumvent aliasing [139]. Whether VFM over-simplifies complex *in vivo* flows remains to be tested. However, Grønli et al. state in the same work that the effect of measurement precision of boundary conditions should be investigated further, and the technique should undergo thorough *in vivo* validation.

Blood-speckle tracking estimates the displacement of blood-speckle patterns [140]. For the blood velocities expected in the LV (~1 m/s, higher for regurgitation jets) very high frame rates are required to limit the inter-frame speckle displacement so that tracking is still possible. Wigen et al. (2018) demonstrated 3D blood speckle tracking in healthy adult volunteers, using multi-beat (7 heartbeats total) 3D volumes and multi-beat 10° wide ‘thin-slice’ acquisitions. Both methods compared well with PC-MRI but mentioned signal-to-noise ratio (SNR) and clutter as significant challenges going forward. Here ultrasound contrast agents (UCA) microbubbles are useful as they provide large SNR improvements over native blood backscatter. The tracking of microbubbles instead of native blood-speckle is called echo-Particle Image Velocimetry (Echo-PIV).

Like speckle tracking, Echo-PIV also requires high-frame-rate (HFR) echocardiography to accurately track the high velocities present in the LV [142]–[144]. We have previously demonstrated that HFR Echo-PIV can accurately estimate the high velocities present in the LV *in vitro* [145] and *in vivo* (Voorneveld et al. "in press") in 2D. Translation to 3D requires HFR 3D echocardiography.

Translation from 2D to 3D HFR echocardiography requires development of new matrix transducers. Here we investigate the capabilities of a prototype matrix transesophageal probe which employs micro-beamforming to reduce the number of channels requiring direct connections to the ultrasound system. The architecture of the probe permits volumetric imaging in a 20° x 20° field of view at the pulse repetition frequency (PRF, 4 kHz in this study). In order to image the whole LV (60° x 60°) a multi-beat acquisition

scheme of just 4 cycles was used with 4 beams per cycle, allowing for a frame rate of 1 kHz. The presented technique would allow for 4D flow-pattern estimation over the whole LV in just 4 heart beats. The accuracy of HFR Echo-PIV using this acquisition scheme is assessed by comparison with time-resolved Tomo-PIV. Tomo-PIV provides high spatial and temporal resolution 4D velocity data in a single cycle but requires optical access. For this purpose, we have designed a dynamic LV phantom that can be imaged with Echo-PIV, Tomo-PIV and (additionally) 4D-flow MRI. In this study we assess the accuracy of 4D Echo-PIV using this prototype matrix transesophageal probe.

4.2 METHODS

4.2.1 Left Ventricular Phantom

A detailed explanation of the LV phantom used in this study is provided in the previous chapter, but a brief overview will be provided here. An optically and acoustically transparent silicone LV shell ($\sim 0.5\text{mm}$ thick) was modelled on the mean shape of a set of 150 computed tomography patient LV segmentations [111], [147]. The LV was fitted with bio-prosthetic mitral (25mm, Perimount, Edwards Lifesciences Corp., Irvine, CA, USA) and aortic (19mm, Perimount Magna Ease, Edwards Lifesciences Corp.) valves and contained in a rigid acrylic pressure chamber with 9 faces to allow for optical access (excluding lid and base, see **Figure 4.1a**). The mitral and aortic tracts of the LV were connected to atrial and compliance chambers (transparent acrylic, built in-house), which were connected via a tube with an adjustable resistance valve (ViVitro Labs Inc., Victoria, BC, Canada), forming the LV flow circuit. The rigid pressure chamber was connected to a programmable piston pump (SuperPump, ViVitro Labs), forming the hydraulic circuit. The hydraulic circuit varied the volume in the rigid chamber, causing the ventricle to expand and contract pumping fluid through the flow circuit. Both the hydraulic and LV flow circuit were filled with a glycerol in water mixture (60:40 by volume, density = 1160 kg/m^3 , dynamic viscosity = $17.7\text{ mPa}\cdot\text{s}$, sound speed = 1790 m/s) to match the refractive index of the silicone LV (1.413). The piston pump oscillated in a sinusoidal pattern (70 beats per minute, 50ml stroke volume) causing the LV to pump the fluid through the flow circuit (red arrows –**Figure 4.1a**). The pump provided an electronic trigger signal for synchronizing acquisitions to a specific phase of the cycle.

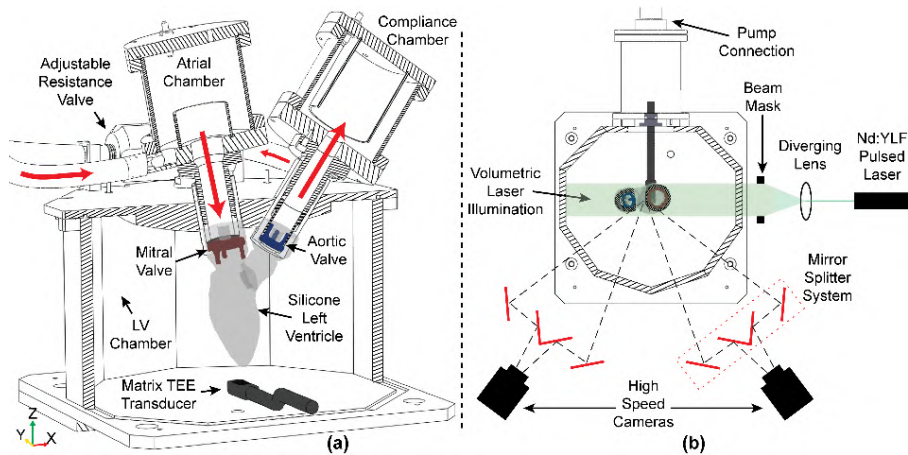


Figure 4-1: a) Partial section view of LV phantom with the matrix TEE transducer shown in its approximate location. Bio-prosthetic mitral (red) and aortic (blue) valves are shown in their position. Red arrows indicate direction of flow circuit. Atrial and compliance chambers are connected by a tube with an adjustable resistance valve. b) Schematic top view of LV phantom showing Tomo-PIV setup, see text for details.

4.2.2 Tomographic Particle Image Velocimetry (Tomo-PIV)

A brief overview of the tomographic Particle Image Velocimetry (Tomo-PIV) setup is provided here, for a detailed description see [148]. Two high-speed CMOS cameras (Imager Pro HS 4M, PCO, Kelheim, Germany), recording at 2000 frames per second, were placed behind two sets of custom-built image mirror-splitter systems, to effectively create four independent views of the LV (**Figure 4.1b**). The whole LV volume was then illuminated using a pulsed Nd:YLF laser (527 nm, Litron Laser, Warwickshire, England) passing through a diverging lens system (**Figure 4.1b**) pulsing at 2 kHz (synchronized with the cameras). Fluorescent Rhodamine-B coated particles (diameter = 20-50 μm , density = 1100 kg/m^3) were used as tracer particles and long-pass 540 nm filters (Thorlabs Inc., Newton, NJ, USA) were used to selectively capture the fluorescent signals from the particles. A single pump cycle was captured (857 ms) and processed with Davis 10 software (LaVision, Göttingen, Germany). An iterative window refinement scheme was used, starting with a kernel size of 7.84³ mm³ for two iterations, reducing to 5.23³ mm³ and finally 3.84³ mm³, all with an overlap of 75%. The final spatial grid resolution was 0.96³ mm³ and the temporal resolution was 0.5 ms. The measured point-spread-function of a single tracer particle was ~ 0.3 mm isotropic.

4.2.3 Ultrasound

A prototype matrix transesophageal (TEE) probe (Oldelft, Delft, the Netherlands) was used for imaging (central frequency 5 MHz). It had separated transmit (128 elements, $5.76 \times 0.9 \text{ mm}^2$) and receive (2048 elements, $8.7 \times 8.7 \text{ mm}^2$) apertures of piezoelectric elements mounted on top of a front-end application-specific integrated circuit (ASIC). The receive aperture is grouped into 128 groups of 4×4 elements, where micro-beamforming is performed on the ASIC for each group, thereby reducing the channel count to 128 in receive (**Figure 4.2**). A detailed explanation of the probe is provided in [149]. The reduced channel count allowed for the probe to be used with a single Vantage 256 ultrasound system (Verasonics Inc., Kirkland, WA, USA). The probe was positioned below the ventricle, typical of an apical view. The probe was placed approximately 5 mm below and 10 mm septal of the ventricle's apex.

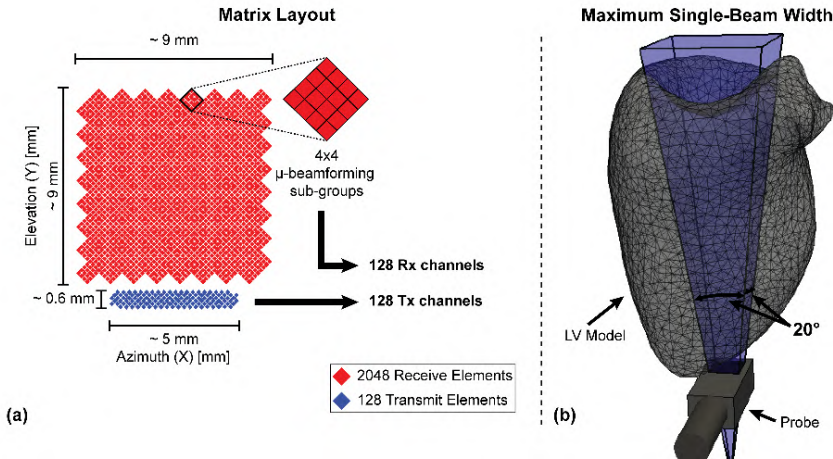


Figure 4-2: a) Schematic layout of matrix elements, note the separated transmit (Tx) and receive (Rx) apertures. The channel requirements in receive are reduced from 2048 to 128 by micro-beamforming in local 4×4 sub-arrays. b) The probe architecture imposes a maximum single-beam opening angle of $20^\circ \times 20^\circ$ in receive. This is insufficient to image the entire LV, thus multiple steered-beams are required to image the required field of view.

A maximum beam width of $20^\circ \times 20^\circ$ was possible while suppressing grating lobes in receive to -20 dB (which appeared diagonally at 21° from the main-lobe due to the slanted receive aperture). However, this was not sufficient for imaging the full LV volume (**Figure 4.2b**). Thus, in order to cover the whole LV ($60^\circ \times 60^\circ$), a rectangular grid of four beam steering angles was used in both the elevational and azimuthal directions ($-20^\circ, -5^\circ, 5^\circ$ and 20°) resulting in $4 \times 4 = 16$ beam angles (**Figure 4.3**). An

additional constraint was that a PRF limit of 4 kHz, to prevent reflection artifacts occurring at higher PRFs (from the LV chamber lid – despite the use of acoustic dampening material on the inside of the lid). Consequently, the use of 16 sequential beams would have resulted in a frame rate of 250 Hz which was not sufficient for high-velocity particle tracking. Therefore, we used a gated sequence of 4 beams per pump cycle over 4 cycles to adequately sample the spatial field of view required, while maintaining a frame rate of 1 kHz (see **Figure 4.3**). Note that this gated sequence is not suited for B-mode imaging of the bubbles as their position is not cyclical. However, for velocity mapping this scheme is acceptable in the case that flow patterns are repeated each cycle and that cycle periods are consistent, so that the motion of the bubbles is cyclical. In the case of this experiment these assumptions were reasonable.

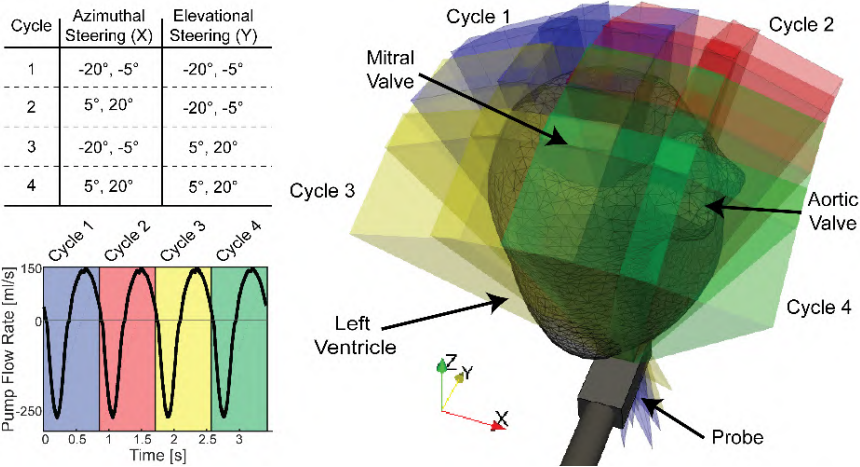


Figure 4-3: Spatial sampling of the full LV volume is gated over 4 pump cycles, with 4 different beams being acquired successively each cycle (16 total). Thus, a region of 60°x60° can be sampled while maintaining a frame rate of 1 kHz, but requiring 4 cycles to acquire.

It was our intention to use diluted ultrasound contrast agent as ultrasound tracer particles. However, the operation of the phantom setup spontaneously generated small air bubbles in the flow circuit with sizes expected to be between 10 and 100 μm which already provided an acceptable concentration of tracer particles. Therefore, no ultrasound contrast agent was added.

A diverging wave transmission was performed using a 3-cycle, 5 MHz tone-burst with a PRF of 4 kHz. Peak-negative pressure was measured to be between 260 kPa at 20mm depth from the probe to 60 kPa at 80mm depth. Details of the transmit and receive

scheme are provided in **Table 4-1**.

Table 4-1: Ultrasound Parameters

Transmit	
Center Frequency	5 MHz
Pulse Repetition Frequency	4 kHz
Virtual Focus Depth	-21 mm
Apodization	Rectangular
Receive	
Field of View (per beam)	120 mm x 20° x 20°
Field of View (total)	120 mm x 60° x 60°
Apodization	Rectangular
Sample Spacing	180 μm x 0.6° x 0.6°
Number of Gated Cycles	4
Frame Rate (per Cycle)	1 kHz

4.2.4 Beamforming and EchoPIV

Acquired RF data were first clutter filtered (**Table 4-2**) and then beamformed using Verasonics software (v3.0.10) in Cartesian coordinate space and envelope detected before inverse-scan conversion to spherical coordinate space. The conversion to spherical space was performed to keep the point-spread-function consistent over depth (**Figure 4-4**). The speed of sound (1790 m/s) of the phantom fluid was adjusted on the Verasonics software for delay computation in both transmit and receive.

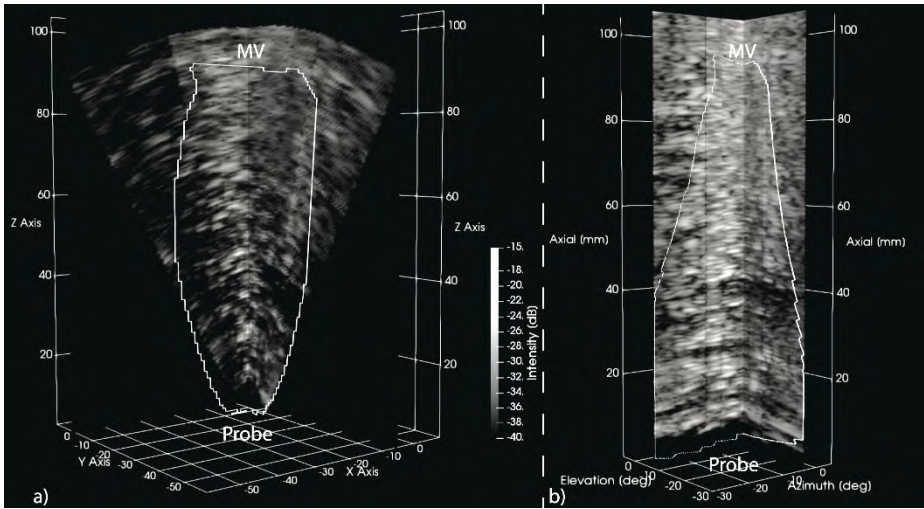


Figure 4-4: Cross-plane B-Mode images of a single sequential set of 4 beams (out of 4 beam-groups). The left image (a) is displayed in the Cartesian coordinate system with the approximate LV cavity borders marked with a white line. Right image (b) shows the same time frame in the spherical coordinate system with the spherically converted LV cavity borders shown. Note how the PSF increases with depth for the Cartesian image (a) but stays approximately constant with depth in the spherical coordinate system (b). Also note that the number of voxels describing the MV region in the spherical coordinate system is greatly reduced compared with the Cartesian image. MV: Mitral valve.

Custom PIV software written in Python (v3.6) was used to perform PIV analysis (**Table 4-2** and **Figure 4-5**) between successive acquisitions with the same beam angle. Ensemble averaging of 5 successive correlation volumes (averaging of the 3D normalized cross-correlation functions for successive frames) was used, producing a vector frame rate of 200 Hz. An iterative window deformation algorithm was used where the second image volume was iteratively deformed using the previous iteration's displacement estimates as a deformation field [150]. Before Echo-PIV analysis the Tomo-PIV data were used to derive a static mask of the LV. For each beam this mask defined where displacement estimation should be performed. After displacements had been estimated for all 16 beams they were combined, averaging overlapping vectors where applicable. Vector data were then scan converted onto a regular Cartesian grid, using the grid spacing at 50mm depth as the cross-beam grid spacing (~1.4 mm). Finally, outlier removal and replacement were performed and vectors were regularized on the Cartesian grid using separate temporal and spatial Gaussian convolution filters.

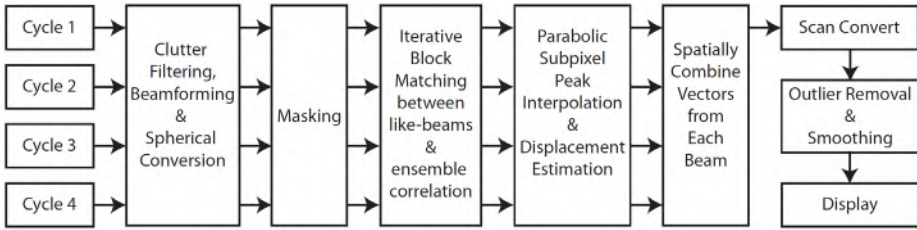


Figure 4-5: High level processing chain utilized in this study. The four sets of beams acquired each cycle are processed individually and combined spatially and scan-converted before outlier replacement and smoothing.

4.3 VISUALIZATION AND COMPARISON

4.3.1 Vector Comparison

Vector data were visualized and flow rates computed using ParaView (v5.6, Ahrens et al. 2005). Before comparison the Tomo-PIV data was down-sampled to match the grid spacing of the Echo-PIV data using a local mean both spatially and temporally. Flow rate through three XY planes (25mm, 50mm and 75mm deep from the probe) as well as a plane intersecting the outflow tract were computed and compared for both Echo-PIV and Tomo-PIV. The average velocity magnitude in a 4 mm section in the center of the jet (at the same plane depths as the flow calculations) was computed too.

4.3.2 Signal-to-Noise Ratio (SNR)

To estimate the noise reference signal a no-transmit acquisition was recorded with all other receive parameters held constant. The SNR could then be calculated using the formula: $= 20 \log_{10} (A_{transmit} / A_{no_transmit})$, where $A_{transmit}$ and $A_{no_transmit}$ are the average signal amplitudes for recordings with transmit on and off, respectively.

4.3.3 Point-spread-function (PSF)

PSF was measured at different depths by measuring the full-width-half-maximum envelope signals of isolated bubbles along the three Cartesian axes.

Table 4-2: EchoPIV Parameters

EchoPIV	
Clutter Filter	55 Hz High Pass 8 th order Butterworth
Similarity Metric	Normalized Cross-Correlation (FFT)
Kernel Size	6mm x 5° x 5°
Iterations	4
Window Deformation	Bi-cubic Interpolation
Overlap	50% x 75% x 75%
Particles	10-100 μ m Air-bubbles
Final Grid (Spherical)	3 mm x 1.25° x 1.25°
Final Grid (Cartesian)	3 x 1.4 x 1.4 mm ³
Correlation Averages	5 frames (5 ms)
Vector Frame Rate	200 Hz
Subpixel Estimator	3x1D Gaussian Peak Fit
Regularization	
Outlier Detection	Universal Outlier Detector [80]
Gaussian Temporal Moving Average	Standard Dev. (σ) = 5 ms Truncation = 3σ
Gaussian Spatial Convolution	$\sigma = 1.6 \times 0.9 \times 0.9 \text{ mm}^3$ Truncation = 1.6σ

4.4 RESULTS

4.4.1 Description of flow field

Shortly after mitral valve opening, a high-velocity jet forms which is angled towards the septal LV wall (**Figure 4-6b** and **j**). Initially a vortex ring develops at the head of the jet, but the septal side of the ring is diminished when it collides with the septal wall (**Figure 4-6d**). From this moment the posterior side of the vortex ring expands, redirecting flow along the posterior-inferior side of the LV towards the base (**Figure 4-6d** and **l**). Once the mitral valve closes the fluid swirls in a general clockwise manner along both the

Azimuthal and Elevational (X and Y) axis, with many smaller vortices appearing along the jet's primary flow path (**Figure 4-6f** and **n**). Once the aortic valve opens, flow travels upwards along the posterior-inferior wall of the LV and up along the base, passing under the mitral valve, before exiting the LV through the outflow tract in a helical pattern (with higher velocities at the top of the outflow tract than at the bottom - **Figure 4-6h**).

4.4.2 Quantitative comparison

During the initial stages of filling, when the jet is beginning to form, Echo-PIV grossly underestimates the velocity and volume of the jet (**Figure 4-6 a** vs **b** and **Figure 4-6 i** vs **j**). Once the jet has progressed deeper into the LV (closer to the probe) Echo-PIV estimates similar velocity magnitudes to Tomo-PIV but still estimates the jet to be thinner in volume (**Figure 4-6c** vs **d** and **Figure 4-6 k** vs **l**). Also, during this phase, Echo-PIV and Tomo-PIV observe similar shapes and positions of the vortex rings, but the magnitudes are larger in Tomo-PIV. During diastasis, Echo-PIV and Tomo-PIV agree in the general swirling of the flow but a more detailed (winding) flow pattern is observed in the Tomo-PIV (**Figure 4-6 e** vs **f** and **Figure 4-6 m** vs **n**). During ejection, Echo-PIV observes similar flow to the Tomo-PIV, moving up the posterior wall turning to travel along the base, but no ejection is detected in the region of the outflow tract.

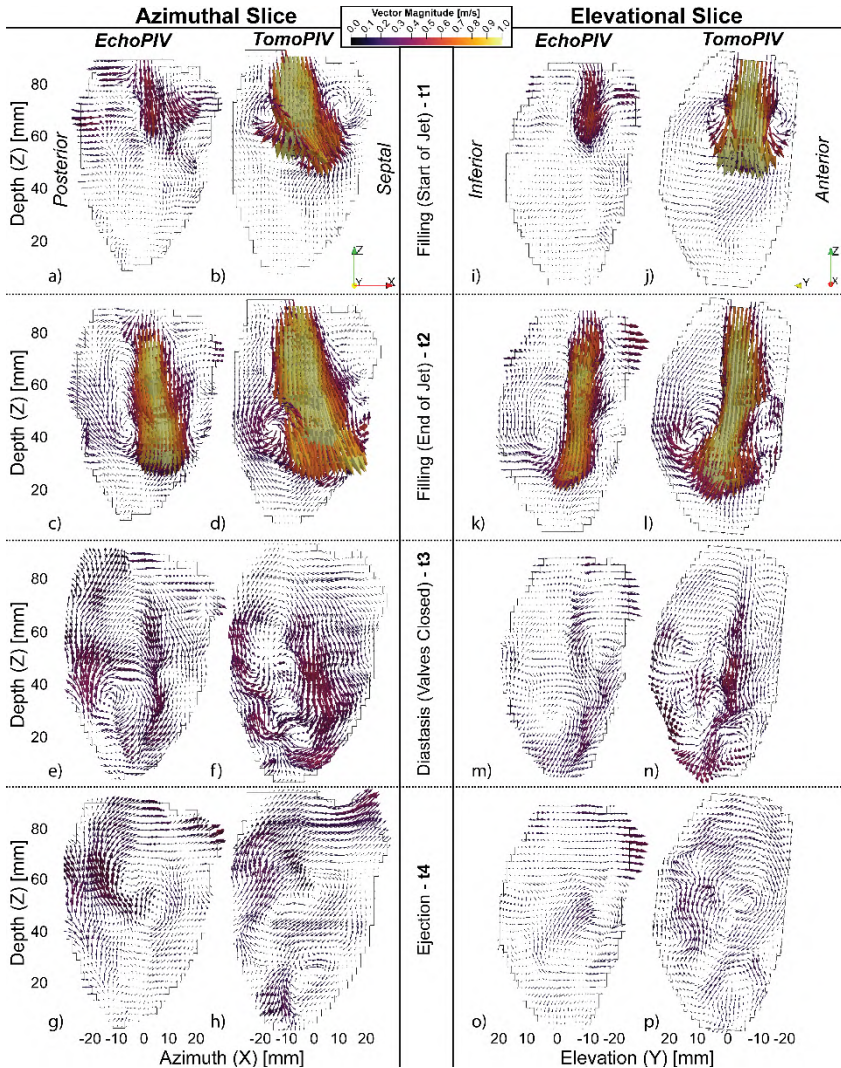


Figure 4-6: a-h) Azimuthal and (i-p) elevational slices through the center of the mitral valve at different phases of the pump cycle (t1 – t4, see **Figure 4.5b**). See text for details. Supplementary videos available online.

4.4.3 Volume flow rate

In order to quantitatively assess the accuracy of Echo-PIV we calculated the flow rate through various planes (**Figure 4-7a**), including: flow through the aortic outflow tract (**Figure 4-7c**); filling flow rates (only flow with negative Z velocity components)

calculated through horizontal (XY) planes at depths of 25 mm (Figure 4.5d), 50 mm (Figure 4-7e) and 75 mm (Figure 4-7f) from the probe.

EchoPIV severely underestimates the flow rate through the outflow tract during ejection (Figure 4-7c - †), with a maximum flow rate of 54 ml/s compared with 145 ml/s for Tomo-PIV. An increase in flow through the plane is detected compared to the rest of the cycle, but the magnitude is severely underestimated.

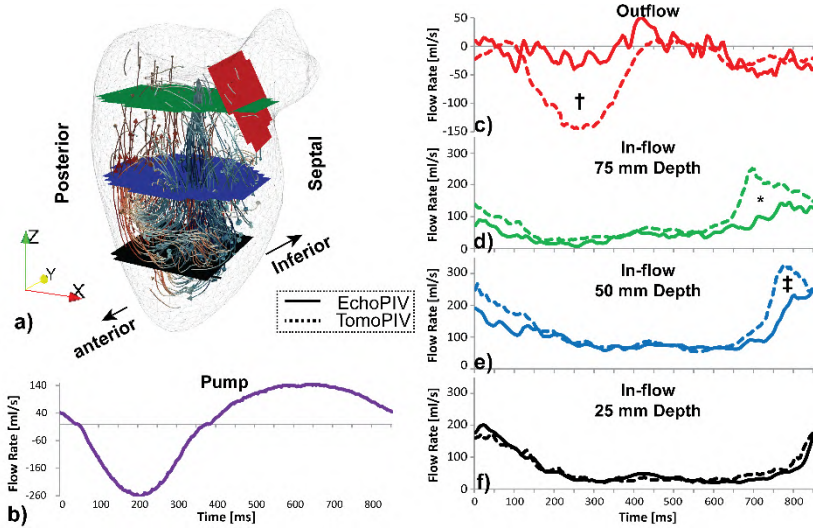


Figure 4-7: a) 3D path-line visualization of Tomo-PIV data at $\sim t_2$, with colored slices corresponding to the through-plane flow rate curves shown in c-f). b) Pump flow rate curve with t_1 to t_4 indicating the time points shown in Figure 4-7.c) Flow rate comparison through the outflow tract and (d-f) through horizontal planes at 75 mm (c), 50 mm (d) and 25 mm (e) depth from the transducer, limited to flow moving in the $-Z$ direction only (inflow). Symbols *, † and ‡ refer to notable flow differences discussed in the text.

During filling, a large underestimation is also observed at the 75mm depth plane (Figure 4-7.d - *) with a difference in maxima of 94 ml/s at the time of jet formation, and a mean underestimation of 34 ml/s over the whole cycle. For the 50mm depth plane the underestimation of peak flow rate reduces to 75 ml/s (Figure 4-7.e - ‡), with a mean underestimation of 31 ml/s over the whole cycle. In the 25mm plane, Echo-PIV overestimates the peak velocity by 21 ml/s with a mean difference of 4 ml/s less than Tomo-PIV over the whole cycle (Figure 4-7.f). Figure 4-7 shows also the discrepancy between the pump flow rate Figure 4-7b and the PIV flow rate estimated at the outflow tract of the LV model (Figure 4-7c - †). This difference may be due to technical issues

like the calibration of the pump or the presence of air bubbles in the hydraulic system (in the long tube or the tank).

4.4.4 Velocity magnitude

Velocity magnitudes at the same depths as depicted in (Figure 4-7a) are shown in Figure 4-8 (average velocity in a 4 mm sphere in the center of the jet). Similarly, we see that Echo-PIV underestimated the high velocities more in the planes further away from the probe. At 75 mm depth the RMSE of Echo-PIV's velocity magnitude was 18 cm/s (17%). This underestimation reduced to 12 cm/s (12%) at 50mm depth and 8 cm/s (12%) at 25 mm depth. RMS error for outflow was 15 cm/s (40%).

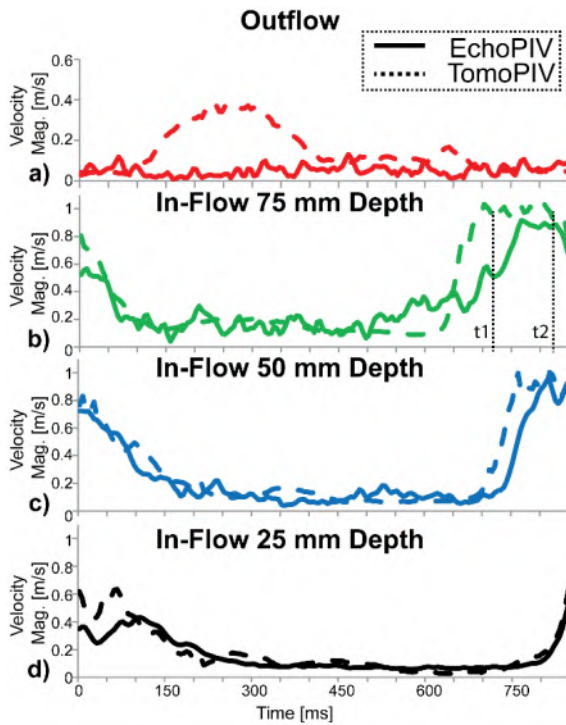


Figure 4-8: Velocity magnitude comparison through a 4mm diameter sphere in the center of the jet at different depths (the same depths as indicated in Figure 4.5a). Solid / dashed lines represent the average velocity magnitude for Echo-PIV and Tomo-PIV. Note that Echo-PIV underestimates velocities more at farther distances from the probe. Time points t1 and t2 shown again for clarity, see Figure 4.7 for velocity profiles these times.

Velocity profiles, measured at the 75 mm plane (Figure 4-7.a – green), during jet

formation and after the jet had fully formed (t1 and t2, **Figure 4-8.b**) are shown in **Figure 4-9**. Note that Echo-PIV highly underestimated the velocity profile during the early stages of filling (t1, **Figure 4-9.a & b**); but correctly measured the profile a short time later (t2, **Figure 4-9.c & d**). Although, while the velocity magnitude was correctly measured at t2, the width of the profile is still underestimated.

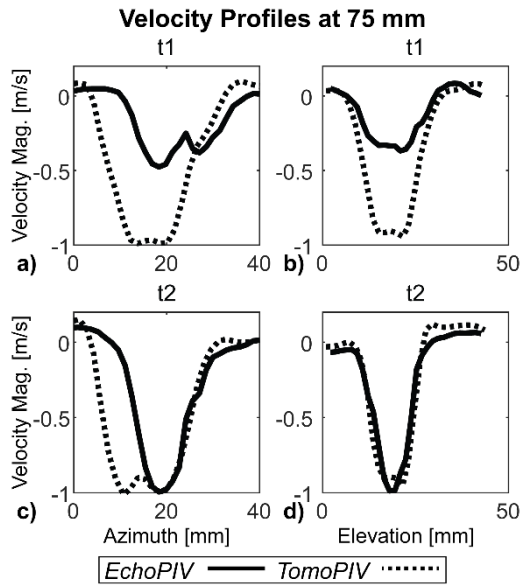


Figure 4-9: Instantaneous velocity profiles, through the 75 mm plane (see **Figure 4.5.a**), at time points t1 (top row: a, b - jet formation) and t2 (bottom row: c, d - jet formed, see **Figure 4.6.b**) along azimuthal (left column: a, c) and elevational (right column: b, d) axes. Note that Echo-PIV underestimates the peak velocity profile magnitude at t1 but not at t2.

4.4.5 SNR and PSF

Calculated SNR and PSF values are shown in Table 3. Between 25 mm and 75 mm depth SNR decreased by 10 dB and the lateral PSF (X and Y) increased 4-fold. The PSF measured from the reconstructed Tomo-PIV volumes was 0.3 mm isotropic.

4.5 DISCUSSION

Flow structures imitating the trans-mitral filling jet were produced by the LV phantom and measured in 4D by both Tomo-PIV and Echo-PIV at high temporal resolution (1 kHz for imaging, 200 Hz for velocity vectors – due to correlation averaging of 5 frames). Both techniques agreed on the general flow patterns observed, but Echo-PIV

underestimated the velocity magnitudes and flow rates in the deeper regions, i.e. close to the mitral and aortic valves.

The two modalities agreed on the development of the central vortex on the posterior/inferior side of the LV. The part of the vortex ring on the septal and anterior side of the LV was less defined in Echo-PIV than Tomo-PIV. This could be due to the lateral width of the vortex on the septal/anterior side, where the lower lateral resolution of Echo-PIV was not able to resolve the flow gradients.

4.5.1 Underestimation in jet

EchoPIV estimated the trans-mitral jet to be of similar shape and follow the same path as Tomo-PIV. However, Echo-PIV largely underestimated the volume flow rate and velocity magnitudes of the jet at the start of filling (**Figure 4-6a** versus b, and i versus j). The Echo-PIV estimate was more accurate closer to the probe (**Figure 4-6c** versus d, k versus l), but the width of the jet was still estimated to be thinner than with Tomo-PIV. Note that Echo-PIV was able to measure similar velocity magnitudes as Tomo-PIV (**Figure 4-9c** & d) but estimated a thinner profile spatially and a delayed temporal response.

The increasing flow rate underestimation with distance from the probe suggests that the PSF, kernel size, SNR and/or clutter are responsible, as discussed further below.

4.5.2 PSF & Kernel Size

The kernel size used ($6 \text{ mm} \times 5^\circ \times 5^\circ$) corresponds to approximately $6 \times 6.5 \times 6.5 \text{ mm}^3$ at a distance of 75 mm from the probe, which is large relative to the final Tomo-PIV kernel size (3.84^3 mm^3). The jet diameter was roughly 15 mm, and the relatively large lateral kernel size of 6.5 mm may cause averaging of the jet edges with the surrounding slow flow regions, resulting in underestimation of the jet profile that we see in **Figure 4-9.c**). Note that the kernel size could not be reduced further as the lateral PSF width at that depth was $\sim 4 \text{ mm}$ after scan-conversion. In our experience, reducing the kernel size to smaller than the PSF has led to a large increase in erroneous vectors. Note that Echo-PIV's lateral PSF was ~ 13 times larger than Tomo-PIV's at 75 mm distance from the probe. We found that using a window-refinement scheme (decreasing window size between iterations of block-matching) resulted in increased underestimation and number of spurious vectors.

A similar interaction between velocity gradient and spatial resolution was found almost 30 years ago, where Foster et al. (1990) found (using pulsed wave Doppler) that longer range-gates underestimated more than shorter range-gates and larger beam-widths increased underestimation of flow profiles in flow profiles with steep velocity gradients [152].

Wigen et al. (2018), using their 3D hybrid autocorrelation / blood-speckle tracking estimator, reported an increasing underestimation of faster lateral velocities, but not for fast axial velocities, which were calculated using a de-aliased autocorrelation estimator [141]. Whether the different trend in results compared to ours is caused by their larger probe aperture or by the different tracking techniques requires further studies.

4.5.3 SNR

In the case of SNR, we calculated that SNR decreased by 10 dB from 25 mm to 75 mm (Table 3). A study by Ekroll et al. (2018) showed that reducing SNR caused increased lateral bias in 2D speckle tracking. However the bias in this work was primarily axial, whereas Ekroll et al. only showed appreciable increases in axial bias at 0 dB SNR [153]. Thus, we do not expect that SNR is the primary source of underestimation seen in the trans-mitral jet. However, SNR may play a significant role in the underestimation seen during ejection, where displacement is primarily lateral.

4.5.4 Clutter

Holbek et al. when using 3D transverse oscillation, observed a similar underestimation in flow rate and even an overestimation of peak-velocity magnitude compared with PC-MRI [135]. They attributed the flow rate underestimation to underestimation of the velocities close to the vessel wall, where the clutter filter removed the moving blood signal. This caused ‘leakage’ of low velocities into the blood flow profile, reducing the overall flow rate.

In this study we tested three different Butterworth high-pass filter cut-offs (27 Hz, 55 Hz and 110 Hz) as well as a Singular Value Decomposition (SVD) based clutter filter with automatic low-rank truncation with the method described in [154], [155]. The 55 Hz high-pass Butterworth filter was used in this study as it resulted in the least amount of clutter remaining in the valve region and the least amount of underestimation in the resulting flow profiles. An adaptive clutter filter may improve the velocity results but was outside the scope of this study.

4.6 LIMITATIONS

4.6.1 LV phantom

The flow patterns generated by the LV phantom share some key aspects with physiological LV flows. For example, the high velocity trans-mitral jet with its

accompanying vortex ring structure (**Figure 4-6.b & j**), and the dominant central vortex structure (**Figure 4-6.d & l**) which redirects the jet upwards towards the base of the LV. Note that flow is not split into an early and late filling phase, as is the case physiologically. This is because the piston-pump moved in a sinusoidal pattern (**Figure 4-7.b**). Interpretation of the physiological consequences of flow patterns observed in this study should take this temporal profile into consideration. Additionally, the LV shell does not include trabecular structures, nor does it contract and relax with a twisting action that is observed in the human LV [156]. However, the purpose of this phantom was to create reproducible flow patterns on a scale like those observed *in vivo*, with less simplistic flow patterns than other common validation phantoms, such as straight tube (laminar flow experiments) [157], [158] or the spinning disk phantom [158]–[160]. This was accomplished in a setup which can be imaged optically, acoustically and by magnetic resonance imaging.

4.6.2 Imaging View

The probe used in this experiment was a TEE probe, but the imaging angle chosen is an apical transthoracic view. An apical view was used because a typical TEE view would have required the probe to be mounted on one of the walls of the LV chamber, but the walls needed to be kept clean for tomographic PIV imaging. If a more typical TEE view were used the distance to the mitral valve area would be reduced to less than 70 mm, by viewing the LV parallel to its long axis. This shorter imaging depth would allow for a higher PRF. On the other hand, viewing the LV perpendicular to its long axis would mandate a larger lateral field of view, possibly requiring more gated acquisitions to fully sample the LV spatially.

4.6.3 Contrast Agent

In this study we used air-bubbles as a contrast medium; *in vivo* ultrasound contrast agent microbubbles would be used instead. Air-bubbles were used as they already appeared spontaneously in the phantom's operation, and earlier iterations of the experiment indicated that addition of microbubbles did not improve the tracking result over the spontaneous air-bubbles. Translation to *in vivo* applications would require the use of ultrasound contrast agent microbubbles where studies would need to be performed to optimize microbubble concentration and acoustic pressures.

4.6.4 Analyses

As the Tomo-PIV and Echo-PIV datasets were not co-registered in space, a pair-wise analysis was not performed, thus comparison between the flow patterns in each dataset

was largely qualitative. A reliable means of registering the two datasets would allow for more accurate quantitative analyses to be performed.

4.7 FUTURE PERSPECTIVES

4.7.1 Resolution

Improving lateral resolution is expected to reduce the spatial smoothing of the jet velocity profile and allow for smaller flow structures to be resolved. Increasing aperture size is difficult for TEE probes due to power dissipation and spatial constraints. However, transthoracic probes have slightly more manageable power dissipation constraints, but the aperture still has to fit between the ribs $\sim 15\text{-}20$ mm.

Alternatively using plane-waves or multi-line transmit sequences may allow for better resolution at depth, which may improve accuracy. However, these imaging schemes will incur a cost in frame-rate, which may complicate the clutter filtering and/or block-matching processes.

4.7.2 SNR

SNR at depth can be improved by transmitting at a lower frequency; however, this will result in significantly lower lateral resolution. Using pulse inversion and second harmonic filtering may help, by transmitting at 2-3 MHz and receiving at 4-6 MHz, thereby increasing penetration depth and reducing tissue clutter simultaneously.

4.7.3 Frame Rate

The proposed acquisition sequence of 4 gated cycles of 4 beams per cycle allowed for a frame rate of 1 kHz while still scanning a field-of-view of $60^\circ \times 60^\circ$. The goal, of course, is for fully time-resolved 4D velocity estimation in a single heart-beat. However, this work serves as an intermediate step; where the requirement for multiple beams was mandated by the probes micro-beamforming architecture. The PRF was limited to 4 kHz to avoid reflection artifacts from the phantom lid, which appeared in the middle of the LV at higher PRF (> 5 kHz PRF should have been possible at 120 mm depth). A higher PRF would have permitted more beams per cycle, while keeping the frame rate constant; thereby reducing the number of gated cycles required for imaging the required field of view. Another method to reduce the number of gated cycles would be to reduce the number of elements grouped together for channel reduction; as this would effectively reduce the pitch in receive so a wider beam could be formed without grating lobes.

In order to reduce spurious vector results we used a correlation ensemble of 5 frames. Increasing the correlation ensemble length will further improve SNR in the case of low velocity gradients, but will be susceptible to correlation peak broadening in the presence of high velocity gradients. Our choice to ensemble average 5 frames reduced the vector frame rate to 200 fps; however, this could also be performed using a moving-average, so that the frame rate could have been preserved at 1000 fps (at the cost of computational time).

4.7.4 MRI

Finally, the proposed LV phantom is also MRI compatible. Future work will assess 4D flow MRI accuracy against Tomo-PIV, facilitating comparison between 4D Echo-PIV with 4D flow MRI.

4.8 CONCLUSION

We have demonstrated, *in vitro*, that 4D Echo-PIV of the whole LV can be performed in just four heart cycles. The general flow patterns compared well with Tomo-PIV, an optical technique with far superior spatial resolution. Significant underestimations in flow rates were observed in the basal region of the LV, close to the mitral and aortic valve, which were located furthest from the probe. The reason for underestimation is suspected to be due to spatial smoothing where point-spread-function is large relative to the spatial velocity gradients.

Comparison of Two Accelerated 4D Flow MRI Sequences with Tomographic PIV in a Pulsatile Left Ventricle Phantom

5.1 INTRODUCTION

The passage of the blood flow in the LV generates 3D flow structures that may play an active role in cardiac function, avoiding kinetic energy dissipation by reorganizing the incoming blood [18], [23], [24]. Still, imaging the highly 3D and unsteady flow field in an opaque and pulsating chamber is a challenging task. Emerging in vivo imaging techniques are often complemented or validated by in vitro methods or in silico solutions [161], where the flow within the patient-specific LV is simulated numerically. Two-dimensional (2D) phase-contrast magnetic resonance (2D PC-MRI) is a widely and clinically available MRI technique used to assess blood flow by a unidirectional encoded-velocity scheme, typically perpendicular to the 2D plane. However, 2D PC-

MRI requires several acquisitions in different orientations to cover the entire domain, which leads to a long scan time. Therefore, the need to image complex cardiovascular structures in a single scan and to assess functional information have stimulated the development of more advanced MR methods.

4D flow magnetic resonance (4D flow MRI), or 4D cardiovascular MRI (4D flow CMR), is a time-resolved PC-MRI method with encoded-velocity in all three directions and the temporal dimension (along the cardiac cycle). 4D flow MRI is currently considered the gold standard technique for in vivo assessment of the volumetric flow field in cardiovascular compartments [9] [8]. One peculiarity of 4D flow MRI is that it provides a complete scenario of the region of interest by allowing retrospective visualization and analysis of the anatomical structure and temporal evolution of the blood flow field in the volume of interest.

Despite its technological advancements, 4D flow MRI still suffers from some technical limitations that hamper its widespread integration in the clinical routine protocol: the low spatial ($3 \times 3 \times 3 \text{ mm}^3$) and temporal (30-40 ms) resolution, long acquisition time (10-30 min), and consequently the long apnoea requirements. To improve the accuracy and to reduce the scanning time, different accelerated 4D flow MRI techniques are now under development [10,11]. Yet, the use of accelerated techniques inevitably implies the reduction of signal-to-noise ratio and consequently deterioration of the image quality. Thus, various studies (see Table 1), mostly performed in simplified phantoms have been conducted so far to compare 4D flow MRI schemes [110], [163]–[169] between each other or against an independent technique with higher spatial-temporal resolution, such as Particle Image Velocimetry (PIV).

Due to its high spatial resolution, time-resolved (if needed) and non-intrusive character, PIV is often considered as the gold standard approach for in vitro fluid dynamics studies. This is particularly true in case of complex flows with moving boundaries and (borderline) turbulent flow, such as in LV. PIV basically permits to measure the instantaneous velocity flow field by analysing the motion of (a group of) tracer particles, which are assumed to faithfully follow the flow [29].

In a number of studies, PIV techniques have already served as a ground truth to validate different MRI imaging modalities [102], [170]. Regarding 4D flow MRI, Töger et al. [171] validated segmented-turbo field echo (TFE) using a vortex ring phantom against 2D-2C PIV and planar laser-induced fluorescence (PLIF) measurements. Recently, the same phantom has been used for a multi-vendor 4D flow MRI comparison [172]. Knobloch et al. [173] performed 4D flow MRI combined with a multipoint velocity encoding scheme in the aortic arch to assess the ability of 4D flow MRI in detecting fluctuation velocity versus particle tracking velocimetry. Medero et al. [174] compared accelerated 4D flow MRI acquisition in an idealized carotid artery bifurcation model against 2D-2C PIV, 2D-3C PIV and Tomo-PIV. However, several 4D flow sequences

are either not validated yet or only performed in a simplified phantom or compared/validated against standard 2D-2C PIV. A non-exhaustive list of phantom-MRI studies is provided in **Table 5-1**.

Therefore, the present work is part of a research project with the aim to develop a versatile and controllable LV phantom that can be imaged using different medical imaging techniques (MRI and ultrasound) and an optimal measurement technique (Tomo-PIV) as a reference. The LV phantom has been already used to study 3D flow structures downstream biological and mechanical heart valves (chapter 3) and to study the feasibility of volumetric Echo-PIV (chapter 4). In the following study, we compare two 4D flow MRI schemes against Tomo-PIV in a phantom model under the same running settings.

Table 5-1 Overview of some of the published works on phantom-MRI investigations.

	Author	Phantom	MR imaging schemes	Reference techniques
PC-MRI	Khodarahmi et al. 2014 [170]	Stenotic tube	PC-MRI	2D-3C PIV
	Okafor et al. 2015 [102]	Left ventricle	PC-MRI	2D-2C PIV
	Roloff et al. 2018 [110]	Rigid carotid model	PC-MRI	2D-3C PIV & Tomo-PIV
4D Flow MRI	Kozerke et al. 2001 [169]	Tube with bileaflet valve	Hybrid 3D PC- MRI	-
	Elkins et al. 2003 [175]	Pipe flow	4D flow MRI*	-
	Marshall 2006 [176]	Stenotic carotid bifurcation	kt -BLAST 4D flow MRI	-
	Ooij et al. 2012 [177]	Rigid intracranial aneurysm	4D flow MRI*	CFD & 2D-2C PIV
	Nilsson et al. 2013 [163]	Rotating cylinder	4D flow MRI (TFE)	-
	Binter et al. 2013 [164]	U-bend flow tube	4D flow MRI with Multipoint VENC	-
	Knobloch et al. 2014 [173]	Aortic arch model	4D flow MRI with Multipoint VENC	PTV
	Kweon et al. 2016 [165]	Stenotic tube	4D flow MRI (GRAPPA)	CFD
	Töger et al. 2016 [171]	Vortex ring phantom	Segmented TFE 4D flow MRI	2D-2C PIV & PLIF
	Urbina et al. 2016 [178] & Montalba et al. 2017 [167]	Aortic phantom	4D flow MRI*	-
Garg et al. 2017 [168]	Circular pipe	EPI, TFE, kt -BLAST 4D flow MRI	Flow volume	

Ha et al. (2017) [179]	Stenotic pipe	4D flow MRI with iPAT	2D-2C PIV
Lee et al. 2017 [180]	Circular pipe	4D flow MRI*	-
Medero et al. 2018 [174]	Carotid bifurcation model	PC-VIPR	2D-3C PIV & Tomo-PIV
Schnell et al. 2017 [181]	Rotating phantom	Dual-VENC 4D flow MRI	
Puiseux et al. 2019 [182]	U-bend tube with branch	4D flow MRI*	CFD

Abbreviations: **CFD**: Computational fluid dynamics. **TFE**: Turbo Field Echo. **GRAPPA**: Generalized Autocalibrating Partially Parallel Acquisition. **EPI**: Echo Planar Imaging. **kt-BLAST**: Broad-use Linear Acquisition Speed-Up Technique. **PLIF**: Planar Laser-Induced Fluorescence. **PTV**: Particle Tracking Velocimetry. **SPIV**: Stereoscopic PIV. **Tomo-PIV**: Tomographic PIV. **VIPR**: Vastly undersampled Isotropic Projection Reconstruction. *: 4D flow MRI sequence not specified

5.2 METHODS

5.2.1 The phantom model

The phantom model consists of two main parts: a LV membrane and a nine-sided tank. The LV membrane has been obtained by painting silicone layers on a LV mould resulting in an approximately 0.5 mm thick shell. The 3D printed LV mould was extracted from the *statistical mean* of a dataset of computed tomography recordings of 150 patients [112], [183] and fitted with inflow and outflow tracts. The LV membrane (indicated by 1) was immersed in a pressurized nine-sided Plexiglas polygon tank (**Figure 5-2a**). Two biological valves (*Edwards Lifesciences, Irvine, USA*) of 25 and 19 mm were mounted in the mitral (indicated by 2) and the aortic (indicated by 3) positions, respectively. The shape of the tank was designed to provide undistorted optical access to the domain of interest from different viewpoints (**Figure 5-1b-c**).

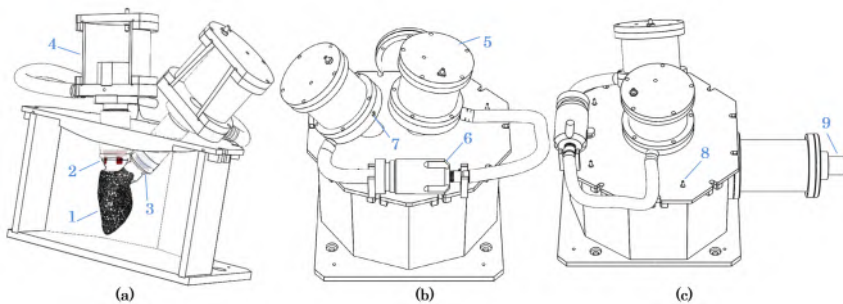


Figure 5-2: Cross-section of the physical LV model and phantom. (a) Two-part 3D printed LV mould with mitral and outflow tracts. (b-c) Front view and lateral view of the nine-sided tank.

5.2.2 Hydraulic circuit

The hydraulic setup consists of two separate flow circuits: (i) LV membrane with atrial and aortic chambers (ii) nine sided tank and pump. The tank was attached (Figure 1c) to the piston pump (Vivitro Labs Inc., Victoria, BC, Canada) to drive and monitor the pulsatile action of the LV membrane. The volumetric changes in the tank then induce inflow and outflow in the LV membrane. The atrial and aortic chambers were screwed to the lid (indicated by 7) and connected together via an adjustable resistance (Vivitro Labs Inc.) (Indicated by 6, **Figure 5-3b**). The pump was velocity-controlled and set to generate a sinusoidal-like waveform with a frequency of 70 beats per minute and a duty cycle of 35%, resulting in a 300 ms systolic period and a stroke volume of 50 ml. Pressure transducers (6069, Utah Medical Products, Inc., Athlone, Ireland) were used to monitor the pressure in the aorta and inside the tank.

The LV membrane and tanks were both filled with the same working fluid, consisting of 60% glycerol and 40% distilled water. To guarantee accurate Tomo-PIV measurements, a fluid mixture was chosen that matches the measured refractive index of the LV silicone (1.414). The dynamic viscosity and density of the working fluid were 17.7 mPa·s and 1160 kg/m³, respectively.

5.2.3 MRI setup and acquisition

The pulsatile pump and its control unit were placed outside the MRI room. The pump was kept running throughout the whole MR protocol. The control unit triggers the pump and retrospectively the MR acquisitions. Special care was taken to replicate the MRI and Tomo-PIV measurements in identical conditions by keeping the relative height between phantom and pump constant and by using the same tubing length. Approximately 5 meters semi-rigid tube were needed to connect the pump (outside the MRI room) with the phantom model (on the MRI bed). Two catheters were used to monitor the pressure in the LV phantom during the MR acquisition.

The MRI acquisition was performed on a 3 Tesla (T) system (Ingenia, Philips, Best, The Netherlands). The cardiac MR protocol consisted of steady-state free-precession 2D PC-MRI followed by two 4D flow MRI schemes, fast nonsegmented gradient-echo without acceleration and one with Echo Planar Imaging readout (with EPI factor of five), further referred to as FFE and EPI (acronyms used by Philips), respectively. The scan parameters were kept identical for the two 4D flow sequences. In order to minimize the effects of Maxwell gradients on MR acquisition the LV phantom was positioned in the isocenter of the scanner with a dStream torso coil on top, and in combination with the posterior receive elements in the table top amount to a total of 32 receive elements for signal reception. A sensitivity encoding (SENSE) [184] reduction

factor (parallel imaging factor) of 2 in the right-left direction (for both acquisitions) and EPI readout with a factor 5 (for EPI acquisition only) for acceleration were set. The most relevant 2D PC and 4D flow MRI imaging parameters are summarized in **Table 5-2**. Concerning 4D flow, in terms of spatial resolution, a field of view (FOV) of 300×300 mm and a slice thickness of 3 mm were set for both sequences and an isotropic voxel size of 3 mm was used. Reconstructed resolution (voxel size) was $1.88 \times 1.87 \times 1.88$ mm³. The velocity encoding (VENC) of 150 cm/s in all three directions was performed using a non-symmetric four-point scheme. 35 phases were acquired and then reconstructed to 30 phases to represent one cardiac cycle. Prior to data processing and analyses, the obtained MR data were pre-processed to minimize background phase errors due to Maxwell terms and eddy current [185]. The correction was performed using the software available on the MR scanner. The eddy current correction was also performed on non-corrected data, by reconstructing velocity data without local phase correction filters from the manufacturer and performing an offline subtraction of static phase data that were obtained from a repeated 4D flow acquisition of the same LV volume but, 30 minutes after the pump was turned off to avoid any remaining waves.

Table 5-2: Most relevant MR imaging scan parameters.

Acquisition parameters	4D flow MRI (EPI)	4D flow MRI (FFE)	2D PC-MRI
Echo time (ms)	4.6	2.1	2.91
Repetition time (ms)	8.7	3.4	4.87
Flip angle (°)	7	7	10
Velocity encoding (m/s)	150	150	150
Acquisition resolution (mm)	$3 \times 3 \times 3$	$3 \times 3 \times 3$	$1 \times 1 \times 8$
Reconstructed resolution (mm)	$1.88 \times 1.87 \times 1.88$	$1.88 \times 1.87 \times 1.88$	-
Field of view [x, y] (mm)	300×300	300×300	337×328
Slice thickness (mm)	3	3	8
N° of reconstructed phases	35	35	-
N° of phases	30	30	30
SENSE [RL, FH]	[2,1]	[2,1]	-
EPI factor	5	1	-

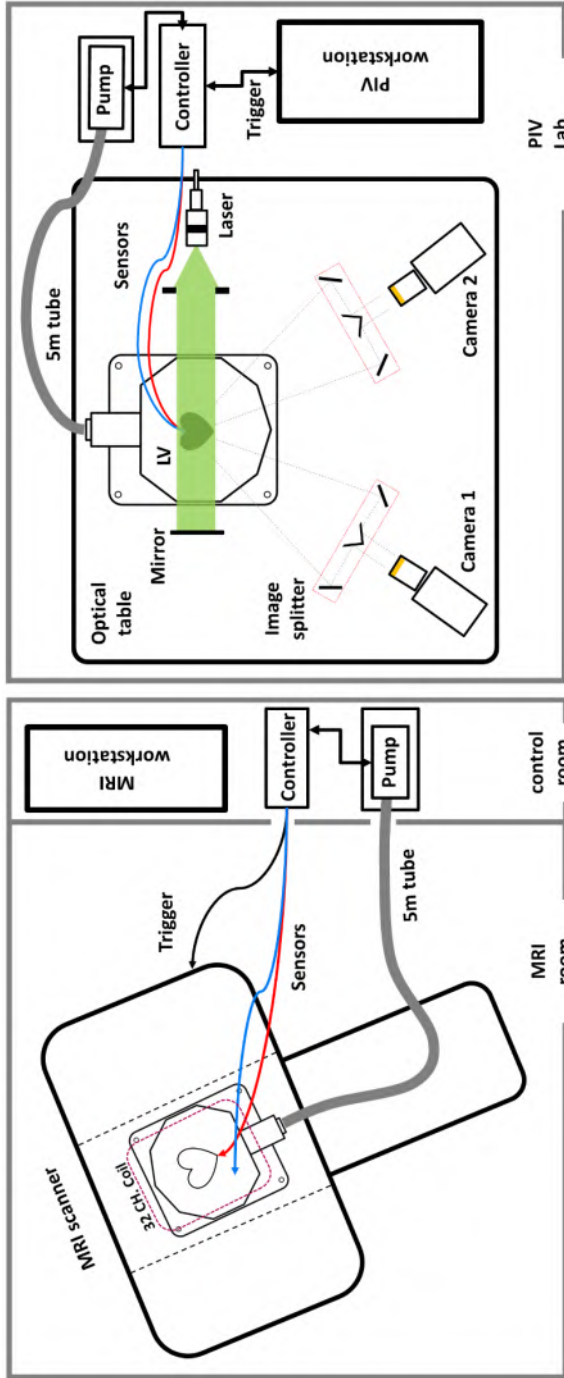


Figure 5-4: *Left:* Layout of the MR setup: the control unit and the pump were placed in the control room. The LV phantom positioned in the isocenter of the scanner and supplied with a 5 meters reinforced vinyl tubing, led through the wall. 32 channels coil was placed on the top of the phantom model. *Right:* Layout of the PIV setup: the imaging system and the LV phantom were mounted on a rigid optical table. The pump is connected to the phantom with a reinforced flexible tube. The control unit triggers the imaging system and the PIV workstation.

5.2.4 Tomographic PIV: setup

Tomo-PIV estimates the instantaneous three velocity components in a whole volume of interest by recording simultaneously images of illuminated tracer particles from (at least three) different angles. In this study, an imaging system was used to perform Tomo-PIV measurements from four different viewpoints using a custom-made image mirror splitter placed in front of each camera. **Figure 5-2** shows the layout of the complete phantom-PIV arrangement. The optical system consists of two high-speed CMOS cameras mounted in a linear composition (Imager Pro HS 4M, PCO, Kelheim, Germany) with 4 megapixels sensor equipped with a Macro prime lenses with a focal length of 100 mm and maximum aperture of T3.1 (Samyang Optics co Ltd., Korea). A long-pass filter at 540 nm (Thorlabs, Inc., Newton, NJ, USA) was mounted in front of each lens to selectively capture the scattered fluorescent tracer light. Fluorescent Rhodamine-B coated particles with a diameter of 20-50 μm and density of 1100 kg/m^3 were used as tracers. A concentration of 0.04 particles per pixel (PPP) has been reached as an optimal measurement condition. The time separation Δt of 500 μs between image-pairs was optimized to ensure that maximum particle displacement is about 6-10 pixels.

A combination of a double-cavity pulsed Nd:YLF laser (527 nm Litron Laser, England) delivering 30 mJ/pulse at 2 kHz with diverging lenses were used to shape the laser beam to volume illumination. A mechanical mask was used to collimate the diverging laser volume to homogenous illumination of approximately $80 \times 110 \times 70 \text{ mm}^3$. To be able to cover the whole measurement domain and to avoid the particle blurring effects an aperture of $f/16$ has been set. **Table 5-3** provides an overview of the relevant experimental parameters for this Tomo-PIV setup.

5.2.5 Tomographic PIV: Calibration, measurement protocol and analysis

To map the 3D space object onto the two-dimensional camera sensor plane (mapping function) a physical calibration has been performed with a calibration target placed in nine positions within the tank. The geometrical calibration yielded an average error for all cameras of approximately 0.2 pixels. Prior to Tomo-PIV measurements a volume self-calibration [61] has been performed to correct the mapping function calculated in the previous step and consequently minimize the disparity error between the four views. The velocity field data were reconstructed from 30 time-averaged cardiac cycles with a temporal resolution of 28.5 ms (30 time points). The spatial resolution after the

Tomo-PIV processing is 0.98 mm (isotropic) and the number of vectors is $63 \times 102 \times 58$ in the three spatial directions (x, y, z), respectively. All data post-processing, calibration, self-calibration steps and tomographic analyses have been performed using Davis 10 (LaVision, Göttingen, Germany).

More detailed information on the Tomo-PIV setup, calibration and processing is given in (chapter 3 and [148]).

Table 5-3: List of relevant experimental parameters for Tomo-PIV.

<i>Imaging</i>	<i>Camera sensor</i>	<i>4 Megapixel CMOS</i>
	<i>Time pulse</i>	<i>500 μs</i>
	<i>Focal length</i>	<i>100 mm</i>
	<i>Lens aperture</i>	<i>16</i>
	<i>Image resolution</i>	<i>12.4 pixel/mm</i>
<i>Laser</i>	<i>Laser</i>	<i>Nd:YLF</i>
	<i>Pulse distance</i>	<i>200 μs</i>
	<i>Laser energy</i>	<i>44 mJ at 2 kHz</i>
<i>seeding</i>	<i>Tracer</i>	<i>Rhodamine-B</i>
	<i>Diameter</i>	<i>20-50 μm</i>
	<i>Density</i>	<i>1100 kg/m³</i>
<i>Fluid</i>	<i>Working fluid</i>	<i>60% Glycerine, 40% water</i>
	<i>Density</i>	<i>1160 kg/m³</i>
	<i>Dynamic viscosity</i>	<i>17.7 mPa·s</i>
<i>Hydraulic</i>	<i>Cycle frequency</i>	<i>70 BPM</i>
	<i>Stroke volume</i>	<i>50 ml</i>
	<i>Peak Aortic and LV pressure</i>	<i>150 mmHg</i>

5.3 PRELIMINARY RESULTS AND DISCUSSION

5.3.1 Comparison: EPI vs FFE

Two 4D flow MRI sequences (EPI and FFE), each with (EPI_{on}, FFE_{on}) and without (EPI_{off}, FFE_{off}) the phase offset correction will be compared side-by-side with tomographic PIV data. The Tomo-PIV velocity field data with a resolution of 0.98 mm³ (isotropic) were down-sampled to match the reconstructed resolution (1.88x1.87x1.88 mm³) of the MR data. Considering that MRI acquisitions have the same spatial resolution and field of view, segmentations parameters are spatial-temporal registered.

Conversely, the registration between the Tomo-PIV and MRI data sets was performed manually on Tecplot 360 (Tecplot, Inc., Bellevue, USA). Firstly, we compare side-by-side the three velocity components between EPI and FFE. The velocity data was obtained in a volume domain that covers the inflow jet (**Figure 5-5**). The agreement between the MRI sequences on using phase offset correction was evaluated according to correlation (R^2) and Bland-Altman analyses.

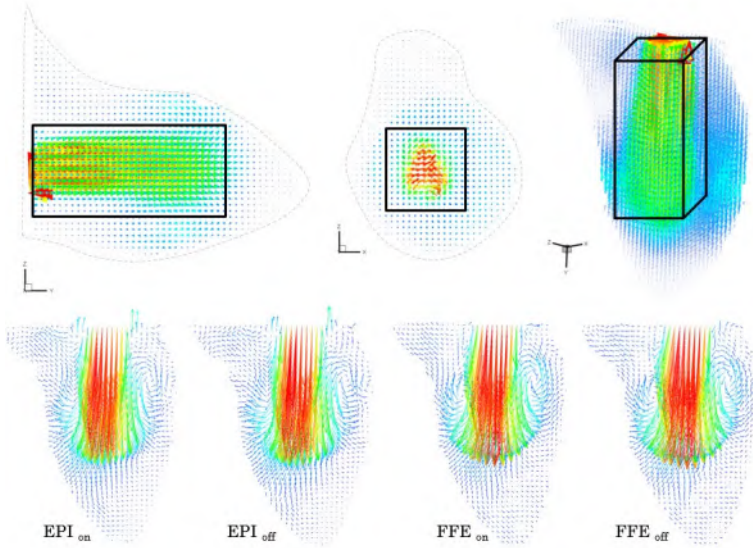


Figure 5-5: Top row: selected velocity vectors for pixel-wise comparison enclosed in the black roi (5096 vectors). Bottom row: Qualitative comparison: Velocity vector field maps of the MR sequences with (on) and without (off) the phase offset correction. The vectors are colour coded based on the velocity magnitude.

Figure 5-6 shows pixel-wise comparison of velocity vector field (enclosed in the black volume (**Figure 5-5**)) obtained with the two 4D flow MRI sequences acquisitions, in order to evaluate the effect of the phase correction filter. For both sequences (EPI and FFE), a strong correlation and very small bias were found between the velocity data corrected (on) and not corrected (off): (EPI_{on} vs EPI_{off}: $R^2 = 1$, bias 0.29 ± 2.25 cm/s. FFE_{on} vs FFE_{off}: $R^2 = 1$, bias 0.34 ± 2.85 cm/s). **Figure 5-7** compares pixel-wise EPI against FFE velocity vector field with the phase correction filter. The two comparisons showed a good correlation and small bias (EPI_{on} vs FFE_{on}: $R^2 = 0.93$, bias 2.4 ± 15 cm/s).

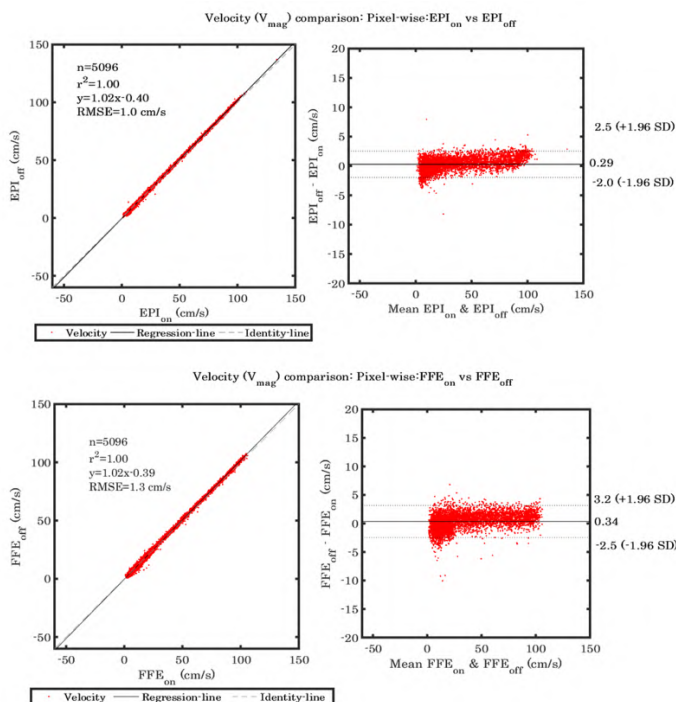


Figure 5-6: Linear regression and Bland-Altman plots of velocity vector field (5096 points). *Top row* EPI_{on} vs EPI_{off}, *bottom row:* FFE_{on} vs FFE_{off}.

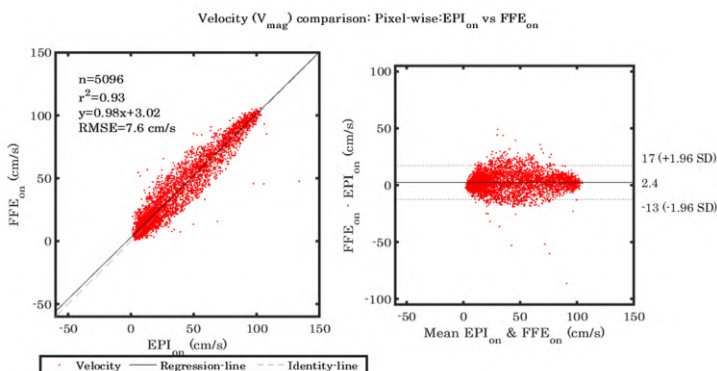


Figure 5-7: Linear regression and Bland-Altman plots of velocity vector field (5096 points) EPI_{on} vs FFE_{on}

5.3.2 Comparison: Tomo-PIV vs EPI and FFE

As mentioned earlier, the Tomo-PIV data is down-sampled to match the spatial resolution of the MRI data. Thus, in order to investigate the influence of down-sampling, **Figure 5-8**, compares the volume flow rate through one slice of raw and down-sampled data. The agreement between Tomo-PIV and 4D flow MRI sequences has been evaluated by comparing the volume flow rate through a slice parallel to the mitral valve and by integrating the kinetic energy in the whole LV domain.

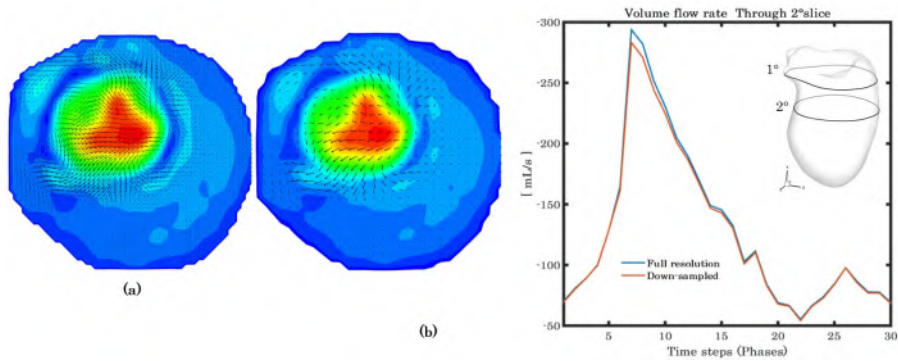


Figure 5-8: *left:* Transversal cross-section of Tomo-PIV velocity vector field (a) full resolution and (b) down-sampled. *Right:* Computed volume flow rate through cross-section 2. Peak difference of 7.5% occurs at time step 7.

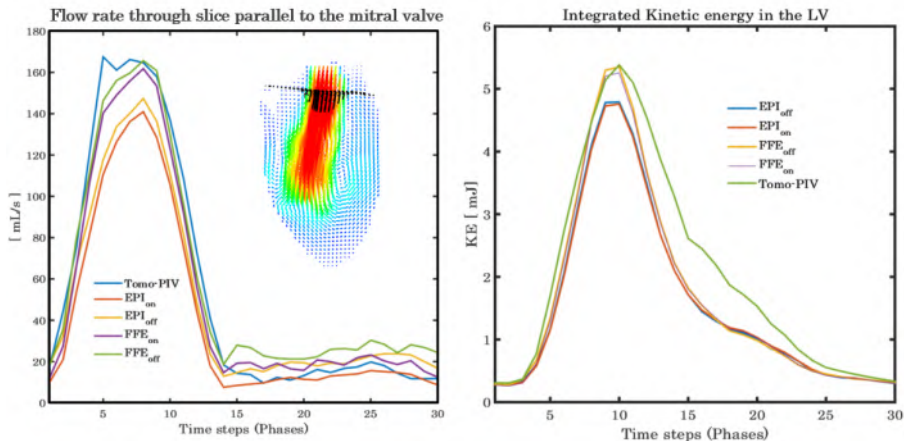


Figure 5-9: *Left:* volume flow rate computed in transversal cross-section (black vectors) perpendicular to the inflow jet. *Right:* integrated KE within the LV. $KE = 0.5\rho \int V^2 dv$, where $\rho = 1060 \text{ kg/m}^3$ and V is velocity magnitude.

5.4 CONCLUSIONS

The goal of this ongoing work is to assess the accuracy of 4D flow MRI sequences using a pulsatile LV phantom and comparing the acquired velocity vector data against an independent technique. Both accelerated sequences were compared pixel-wise with and without the phase correction filter and correlated well, with small bias. Further, the sequences were compared to downsampled Tomo-PIV data by calculating the volume flow rate and kinetic energy.

Conclusions and future perspectives

6.1 CONCLUSIONS

Here we provide a summary of the PhD work and the most important findings. We would like to point out that each chapter contains a dedicated discussion and conclusion section.

The visualization of the unsteady 3D flow within a moving opaque cavity such as a large blood vessel, an aneurysm or the LV, as well as the quantitative measurement and interpretation of the flow velocity fields, are challenging tasks. A multidisciplinary approach is required which integrates medical imaging, computational methods and their validation by means of experimental techniques. The analysis of distinctive flow patterns in the LV may lead to new flow-based metrics for early diagnosis, complementary to conventional functional parameters (e.g. flow imaging, transmitral flow velocity parameters and tissue velocities) and anatomical information. Also, it could provide further insights into the relation between (prosthetic and native) mitral valve function and LV flow [71], [186], [187].

Several recent studies highlighted the use of PIV data in support of numerical simulation results [16], [103], [161], [188], [189] and medical imaging data [102], [143], [171], [190]. While in vitro simulations are an indispensable component of the LV fluid dynamics research cycle [191], the use of PIV systems is not restricted to validation or comparison studies. A number of studies focused on the relation between mitral valve flow and LV flow [72] [73], [101], [192].

Generally, all in vitro studies inevitably rely on simplifications, such as, (imposed) pressure and flow conditions, mechanical and geometric properties of the model and the fluid properties. As mentioned in several studies available in the literature, the insights offered by planar measurements are rather limited; only three-component measurements can overcome the simplification of the symmetrical flow pattern assumption. Moreover, the estimation of various fluid dynamics parameters (such as Reynolds stresses, turbulent kinetic energy and vorticity) is impaired because of the absence of the third velocity component. These limitations are overcome in volumetric measurements, as they provide all components of the velocity gradient tensor and, as such, allow for more accurate computations of fluid dynamic variables. As shown in the present work, we believe that volumetric reconstruction of the flow field, starting from a complete data set of velocity components, should allow for a more reliable investigation of the effect of the valve type and orientation on LV flow.

In recent years, only few technically oriented PIV studies actually attempted to reconstruct the 3D flow in a laboratory model of a ventricular cavity. The state of the art is shown in a study of Fortini et al., who carried out time-resolved planar PIV measurements using a feature-tracking algorithm [92] on two sets of orthogonal planes in an LV replica. The two-dimensional Eulerian velocity data were phase averaged over the cycles and combined (by linear interpolation) to obtain a 3D velocity field. The resulting temporal and spatial resolutions of the data set were 4.0 ms and 2.2 mm, respectively. These data were later used as a reference to compare with numerically simulated flow data [189]. Falahatpisheh et al. suggested a different approach and started from planar PIV measurements acquired on multiple perpendicular planes and reconstructed the data into a 3D velocity field through Kriging interpolation and by imposing the incompressibility constraint (i.e. ensuring a divergence free velocity field). Despite the fact that they were based on 2D PIV data (which causes minor projection errors to the velocity vectors and derived parameters) [37], both studies have contributed significantly to the field of LV hemodynamics. In a recent work, Tang et al. have performed multiplane stereoscopic PIV measurement in an LV model to evaluate the effects of a prototype valve on the LV flow dynamics [105].

The aim of this PhD project was to extend current Particle Image Velocimetry techniques to capture the complex intraventricular flow dynamics. In the first step, a stereoscopic PIV setup has been upgraded to be able to acquire particle images in

several parallel planes by performing only one calibration. The setup has been used to reconstruct 3D flow velocity data within a simplified LV model. Next, in collaboration with different research groups (Erasmus MC, TU Delft and LUMC), a new LV phantom has been designed and fabricated to be used in multimodality imaging techniques: Tomo-PIV, MRI and Echo-PIV. It has allowed to investigate and compare under the same running conditions the effects of prosthetic heart valves on the flow in the LV domain. The LV phantom has been imaged with a prototype transesophageal matrix probe and 4D flow MRI. Subsequently, the acquired data have been compared to Tomo-PIV measurements.

In the second part of the thesis, we have presented in chapter 2 a PIV setup consisting of relatively low end hard- and software. It allows volumetric (3D) reconstruction of the flow velocity field in a transparent pulsatile LV membrane model. The setup was primarily designed and developed to facilitate consecutive stereoscopic PIV measurements in several parallel planes, without repeating the complex and time consuming stereo calibration. The setup has been used to evaluate the effects of the orientation of a bileaflet valve on the intraventricular flow dynamics. For each orientation, the 3D velocity map has been reconstructed at two time points of the cardiac cycle. Our results indicate that in both orientations the bileaflet valve gives rise to a crossed flow path. The anatomical orientation produced a more organized flow pattern and presented a vortex core closer to the LV apex. However, this latter configuration produced a higher vorticity downstream the aortic valve compared to the anti-anatomical orientation. This phenomena may be explained by the opening from outside of the bileaflet valve that induces jet dispersion. However, the presented results were obtained in an axisymmetric LV model and adopted a working fluid containing sodium iodide which does not permit the use of biological valves which experiences a dehydration process.

In chapter 3, we have implemented a tomographic Particle Image Velocimetry (Tomo-PIV) setup. It is known that Tomo-PIV requires at least three views in order to correctly reconstruct the 3D object. In our study, in order to reduce the PIV apparatus costs, an imaging system that allows to record particle images from four angles using only two cameras has been developed. Phase-locked measurements were carried out in an anatomically shaped LV phantom. The effects of the geometry and the orientation of different prosthetic heart valves on the LV flow dynamics were analysed by means of velocity vector maps, vortical structures and kinetic energy maps within the LV domain. The results show that due to a larger orifice, the kinetic energy level associated with the biological valve during diastole is approximately four times higher than the mechanical valves. However, this kinetic energy is dissipated much faster in the BHV

than in all of the MHVs. The rapid decline of kinetic energy in case of a BHV could indicate that accurate positioning during surgical implantation is more critical for a BHV valve than for a MHV. Furthermore, the results also indicate that an anatomic orientation of the bileaflet valve yields an overall slightly higher kinetic energy of the inflow jet than the anti-anatomic configuration. Yet, none of our performed analyses reveal that one orientation of the bileaflet valve is to be preferred over the other in clinical practice. Additionally, the results indicate that the jet entering the LV cavity collides more closely to the apex with a porcine valve than with a bileaflet valve. This facilitates the wash-out of the apical region, avoiding stagnation zones, which may indicate that the BHV performs better than a MHV in patients with dilated cardiomyopathy.

As we have introduced in the first chapter, intraventricular fluid dynamics is a multidisciplinary domain, where engineers and clinicians collaborate to understand the physics of the blood flow inside the heart and to ameliorate the available imaging tools. For this purpose, the here presented LV phantom and the Tomo-PIV measurements have been used to evaluate the feasibility and accuracy of emerging medical imaging techniques in the third part of this thesis. In chapter 4, we have used a prototype transesophageal matrix probe for 3D high frame rate (4 kHz) imaging to test the capabilities of 4D Echo-PIV in capturing the flow field within the LV. The results indicate that volumetric 4D Echo-PIV of the whole LV can be performed in just four heart cycles. The results also showed that 4D Echo-PIV is able to depict the general flow patterns. However, it underestimates the velocity magnitudes and flow rates closer to the mitral and aortic valves. In chapter 5, we have compared the velocity field obtained with two 4D flow MRI accelerated sequences with and without the phase correction filter. Also, in this case Tomo-PIV data were used as an independent validation technique. MRI measurements in the LV phantom allowed to perform pixel-wise comparison of 3D velocity vector data between different accelerated sequences. Preliminary results show a strong correlation and small bias between the velocity data with and without background correction filter. Further, the sequences were compared to downsampled Tomo-PIV data by calculating the volume flow rate and kinetic energy.

6.2 FUTURE PERSPECTIVES

6.2.1 Clinical challenges

The role of flow structures in the LV cavity is yet under investigation and the choice of mitral valve replacement (especially between biological and bileaflet valves) is still an

open question. The approach of selection is often determined by balancing the risks of anticoagulation and reoperation. A recent study indicates that the use of biological valves was associated with a higher risk of reoperation than the use of mechanical valves. These findings were associated with the increased structural valve degeneration and not with flow dynamics alterations.

With the progress of catheter-based technology, mitral valve treatment is moving towards less invasive approaches. Mitral valve repair does not only preserve anatomical elements, but also maintains the normal intraventricular flow dynamics and it is energetically more efficient compared to valve replacement. MitraClip is one of the most implanted devices to treat mitral valve regurgitation. The device mimics the surgical edge-to-edge repair by clipping the leaflets edges. However, the MitraClip leads to a double orifice and an increase of the pressure gradient, which may require a repositioning of the device. Alternatively, transcatheter mitral valve replacement strategy is a highly active research area. However, these techniques are still complicated by the risk of LV outflow tract obstruction and valve migration. It would be highly interesting to compare the percutaneous against mitral valve replacement techniques. However, due to the complexity of the mitral valve apparatus (native leaflets, chordae and papillary muscles) it doesn't seem feasible to design and implement an in vitro model to investigate the effects of percutaneous treatments or LV wall diseases on the intraventricular fluid dynamics.

The LV cavity presents complex flow dynamics with straight and turning flow, flow-flow and flow-structure interactions, recirculation regions and structures that develop and extinguish within the cardiac cycle. All these phenomena are altered with the change of wall thickness, shape, rhythm and geometry (of the LV cavity and the valve). The clinical interest is to evaluate whether these flow phenomena reveal the underlying cardiac conditions and to find out if it is possible to develop flow parameters to aid in choosing the best surgical interventions, medication or pacing strategy. However, patients with similar cardiac dysfunction can present with different degrees of cardiac compensation. This makes it difficult to use single flow-based parameters for diagnostic or stratification purposes. The complex flow structures inside the LV may suggest the combination of a flow-based parameter such as vorticity, pressure gradient or kinetic energy for different blood flow components (such as direct flow and retained inflow traces) in various disease conditions.

6.2.2 Technical challenges

Emerging medical techniques that can image 3D flow inside the heart throughout the cardiac cycle are becoming more mature and can provide more details on the flow structures. Technological advancements in the ultrasound field have managed to bring

2D vector flow visualisation in to a clinical scanner. The high temporal resolution obtained with ultrasound compared to 4D flow MRI is a great advantage to image rapid flow in the LV. However, the spatial resolution and clutter filtering are still limitation factors of the image quality and therefore clinical assessment of intraventricular flows. Several research groups are developing new high frame/volume rate ultrasound techniques to image the flow inside the heart using either modified clinical scanners or research acquisition platforms.

4D Flow MRI is a promising tool that allows intuitive visualization and quantification of the intraventricular flow during the cardiac cycle. MRI allows flow-based studies to reconstruct the averaged velocity field in all three directions over hundreds of cardiac cycles. Despite that, the technique still suffers from technical limitations such as relatively low spatio-temporal resolution and loss of SNR related to the acceleration factor, as well as the time consuming post-processing procedure and lack of standardized workflow. 4D flow MRI with accelerated sequences is an evolving technology and its accuracy and usefulness in depicting intracardiac flow are under investigation in various experimental and in vivo studies.

Experimental fluid dynamic studies play an important role in the cardiovascular fluid dynamics tool-set (computational models, in vivo research in animal models/humans) in investigating the impact of new medical devices on the vascular or cardiac system. In the LV field, in vitro studies are mostly focused on understanding the impact of different mitral valves on the LV flow dynamics or the effect of aortic valve regurgitation on the intraventricular flow structures. With technological advancements in PIV, it has become possible to obtain 3D velocity vector fields at high spatial and temporal resolution. This serves to understand complex flow phenomena and overcome the assumption of symmetric flow or the acquisition of multiple measurements to reconstruct the domain under investigation.

The outcome of experimental studies, the 3D velocity vector field over the cardiac cycle datasets, is often used for validation purposes. However, in order to perform blood flow simulations inside the heart, there are several factors and parameters that have to be provided and measured. The geometry of the LV during the cardiac cycle is an important factor in computational flow dynamic simulations. They can be extracted from medical images (3D ultrasound or Cine-MRI). However, due to the low temporal resolution, the shape of the LV is available only at few time points over the cardiac cycle. Consequently, intermediate geometries have to be interpolated. The quality of the model depends also on the image quality and spatial resolution. Additionally, the shape of the heart valves and their motions create significant complications for CFD of intraventricular flow. The shape of the prosthetic heart valves (mechanical and biological) is relatively easier to reconstruct compared to native heart valves. The motion of the leaflet can be prescribed based on medical imaging data or sensor

measurements (like sonocrystal transducer) can be used to create a kinematic model of the leaflets. Further complications are the papillary muscle and chordae attached to the native valve.

6.2.3 Technological advancements in the field of PIV

In biomedical flows, when the flow is often periodic (like LV flow in patients in sinus rhythm or in experimental settings), the fluid dynamics can be investigated by synchronizing the PIV apparatus with the hydraulic circuit and performing measurements in a phase-locked manner. The relevance of using a phase-locked protocol has been questioned by [101], due to the beat-by-beat changes in LV flow observed in vivo as well as in our LV phantom. However, the authors believe that ensemble averaged flow structures, compared to time resolved flow structures acquired within a unique cycle, are more suitable for validating new in vivo imaging tools, like 4D flow MRI, given that beat by beat changes are discarded during the acquisition. On the other hand, it is probably more representative to rely on time resolved flow data (obtained in one or a few cardiac cycles) to extract the Lagrangian path lines and calculate the time-varying viscous stress that is experienced by the blood corpuscles when they move along their path.

The 3D velocity vector field presented in chapters 3 and 5 were obtained by processing particle images in a phase-locked manner. Instead, in order to be able to compare high-volume rate Echo-PIV, time-resolved data have been acquired as well. However, one of the limitations of Tomo-PIV is the required processing time to extract one velocity field starting from the four particles image pairs. A collaborative study with a research group of the German Aerospace Center (DLR) is ongoing to overcome the limitation of the Tomo-PIV processing time. The recording sequence was processed using the *Shake-The-Box* (STB) algorithm [52]. STB is a Lagrangian Particle Tracking (LPT) algorithm employed to reconstruct individual particle tracks during the cardiac cycle. In this case, STB enables the reconstruction of single particle tracks in 3D over long time-resolved sequences of recordings from a multi-camera imaging system. The method makes use of the Iterative Particle Reconstruction to reconstruct the 3D particle locations. An initial phase where tracks are identified over the first few realizations is followed by the prediction of the particle location at subsequent recordings; the predicted location is then corrected by means of an image matching scheme. Subsequently, the scattered position, velocity and acceleration measurement provided by the STB are interpolated onto a regular 3D grid by the FlowFit data assimilation algorithm [193] where a system of cubic B-splines is used to represent the velocity and pressure fields. By leveraging physical constraints derived from the Navier-Stokes equations, the spatial resolution is increased beyond the sampling offered by the tracked particles. The spatial gradients (such as vorticity, Q-criterion and viscous stress) can be evaluated analytically from the

B-spline functions. In addition, the FlowFit data assimilation algorithm allows for the extraction of the 4D relative pressure field.

Figure 6-1 shows approximately 7000 individual particle tracks during the inflow phase (left panel); the tracks are visualized in the 3D domain by plotting the velocity vectors (color-coded by the vertical velocity) at the instantaneous particle locations along 18 subsequent recordings. The biological valve induces a strong trans-mitral jet directed towards the anterior wall of the LV, with a vertical velocity (V_y) of up to 1.3 m/s. The right panel of the figure depicts the iso-surface of velocity magnitude coloured by the pressure field relative to an offset (normalized by fluid density). The ability to extract particle tracks and the relative pressure field will give the possibility to validate for example MRI softwares used in clinical research. Additionally, the dynamic LV geometry over the cardiac cycle has been extracted (averaging particle tracks within the LV) and will be used for numerical simulation studies.

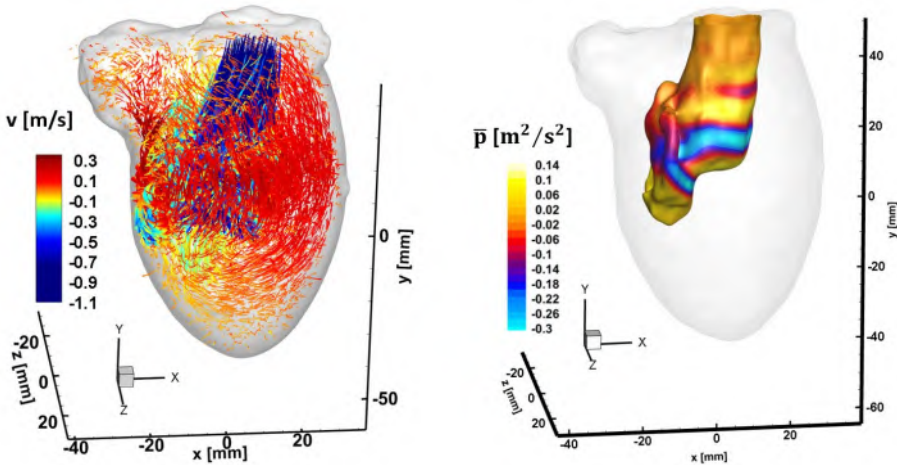
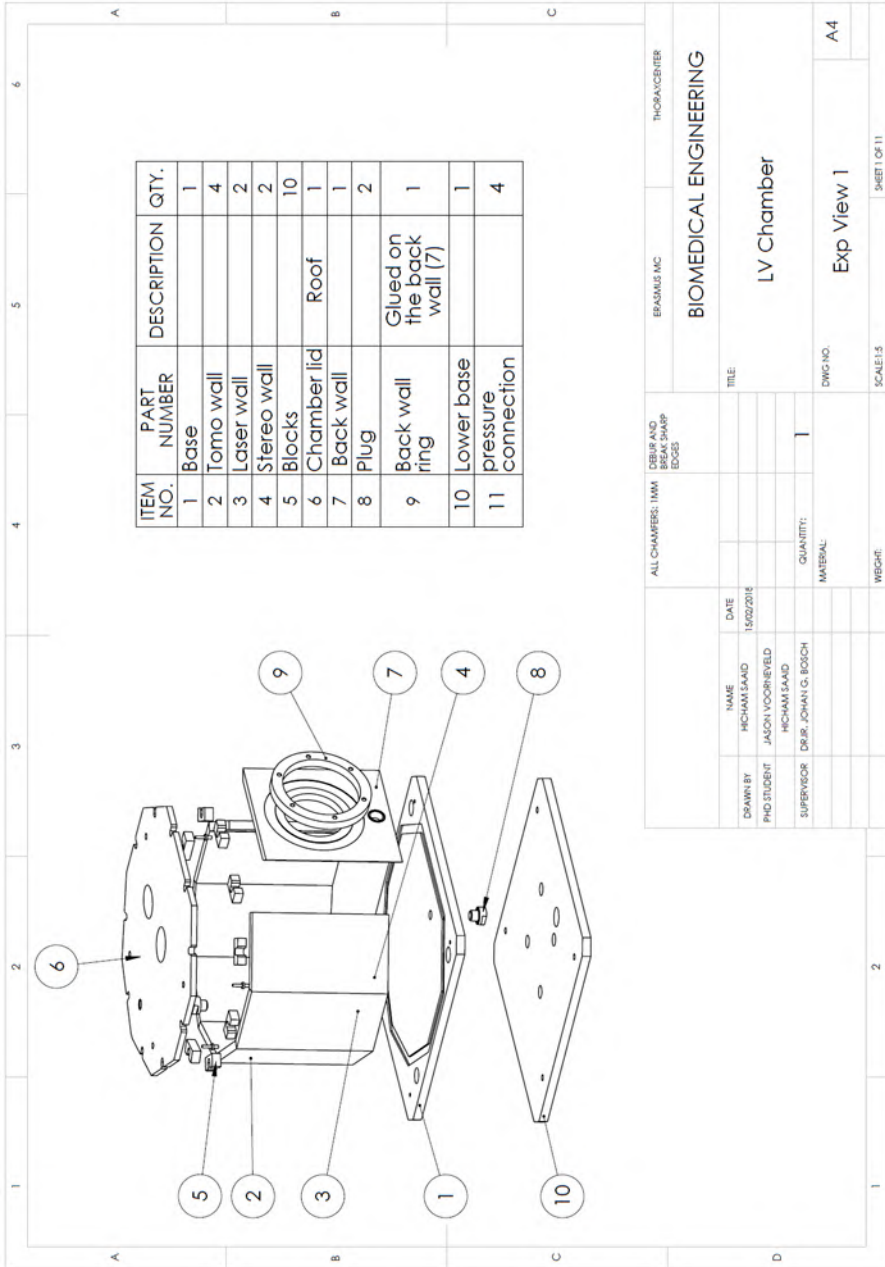
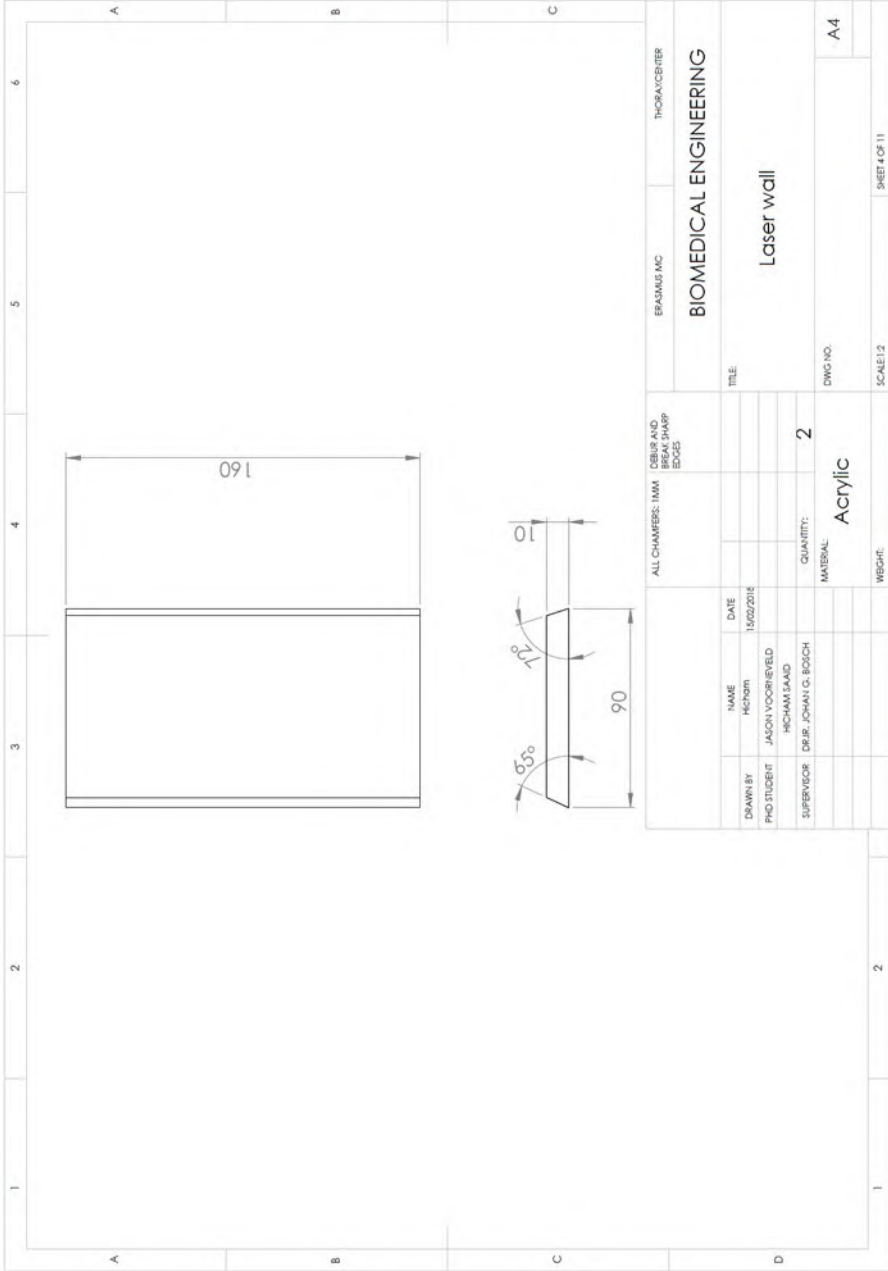


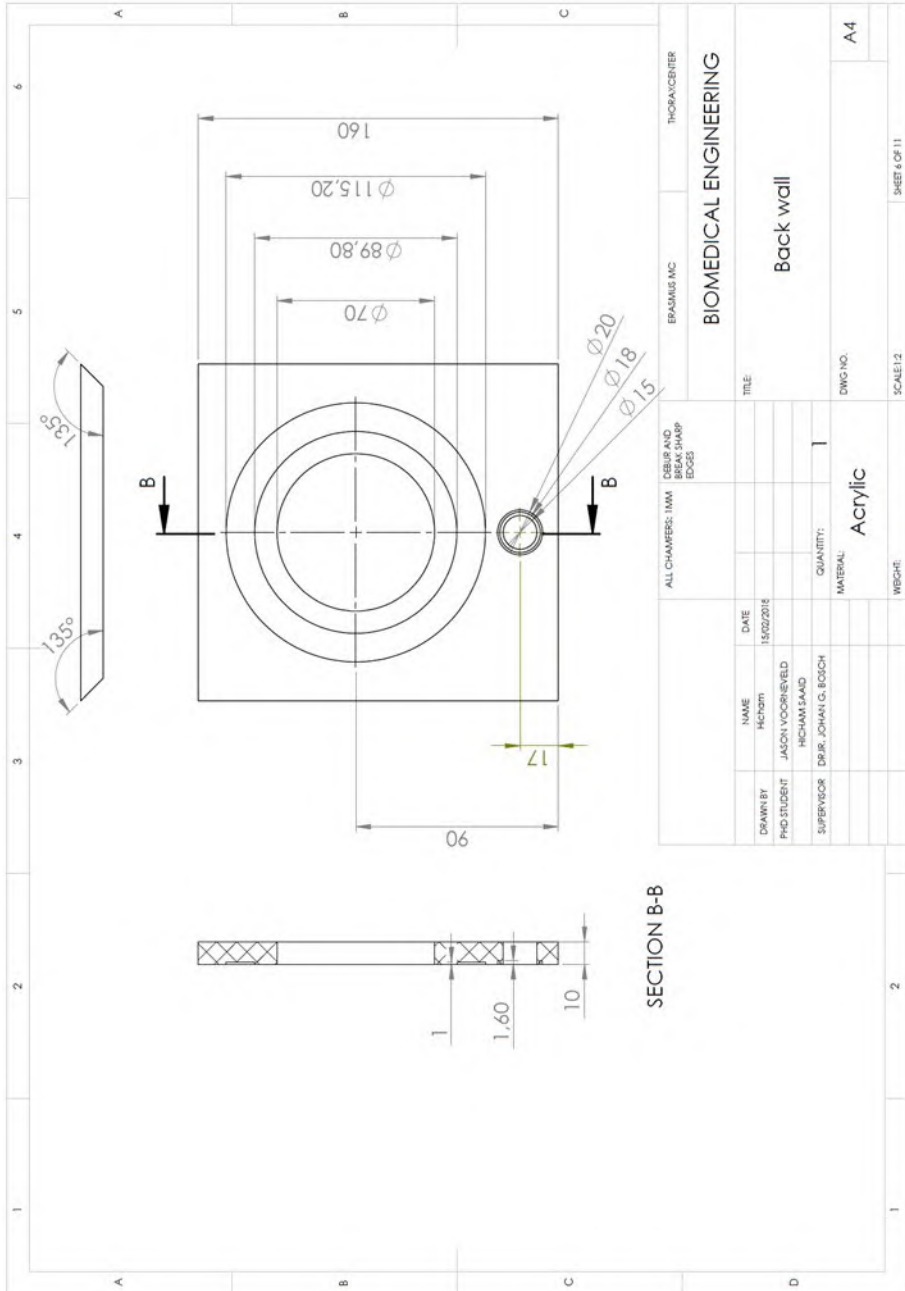
Figure 6-1: *left*, Particle tracks over 18 recordings during the diastolic phase, colored by the vertical velocity component (along the Y axis). *Right*, Isosurface of velocity magnitude color-coded with the relative pressure.

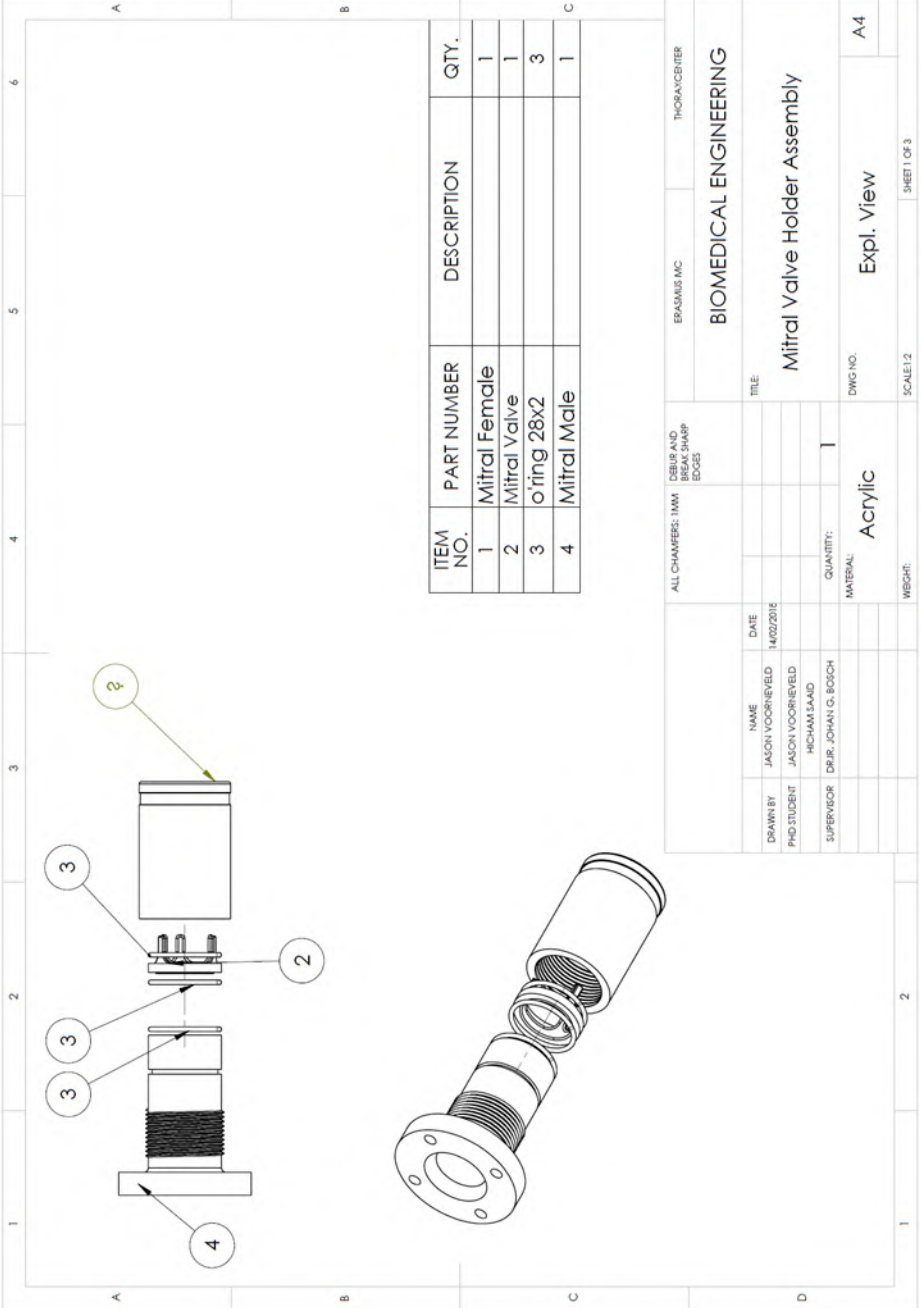
Appendix: Technical drawings



ALL CHAMBERS: 1MM CSPR AND BREAK SHARP EDGES		ERASMUS MC	THORACRITER
BIOMEDICAL ENGINEERING			
DRAWN BY: HICHAM SAAD		TITLE:	
PHD STUDENT: JACON VOORRIEVELD		LV Chamber	
SUPERVISOR: DR. JOHAN G. BOSCH		DWG NO.:	
		Exp View 1	
		SHEET OF 11	
		SCALE: 1:1	
		A4	

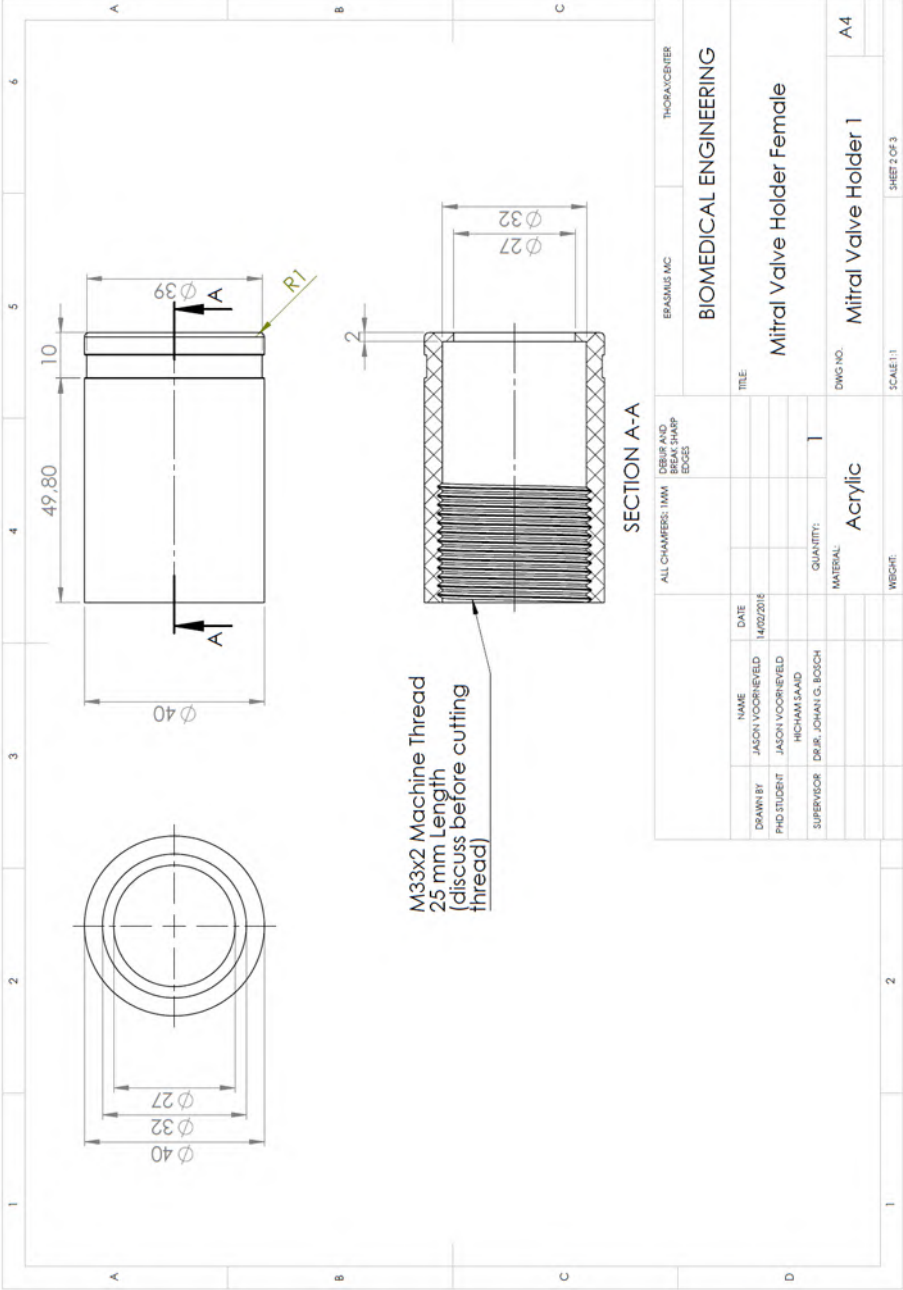




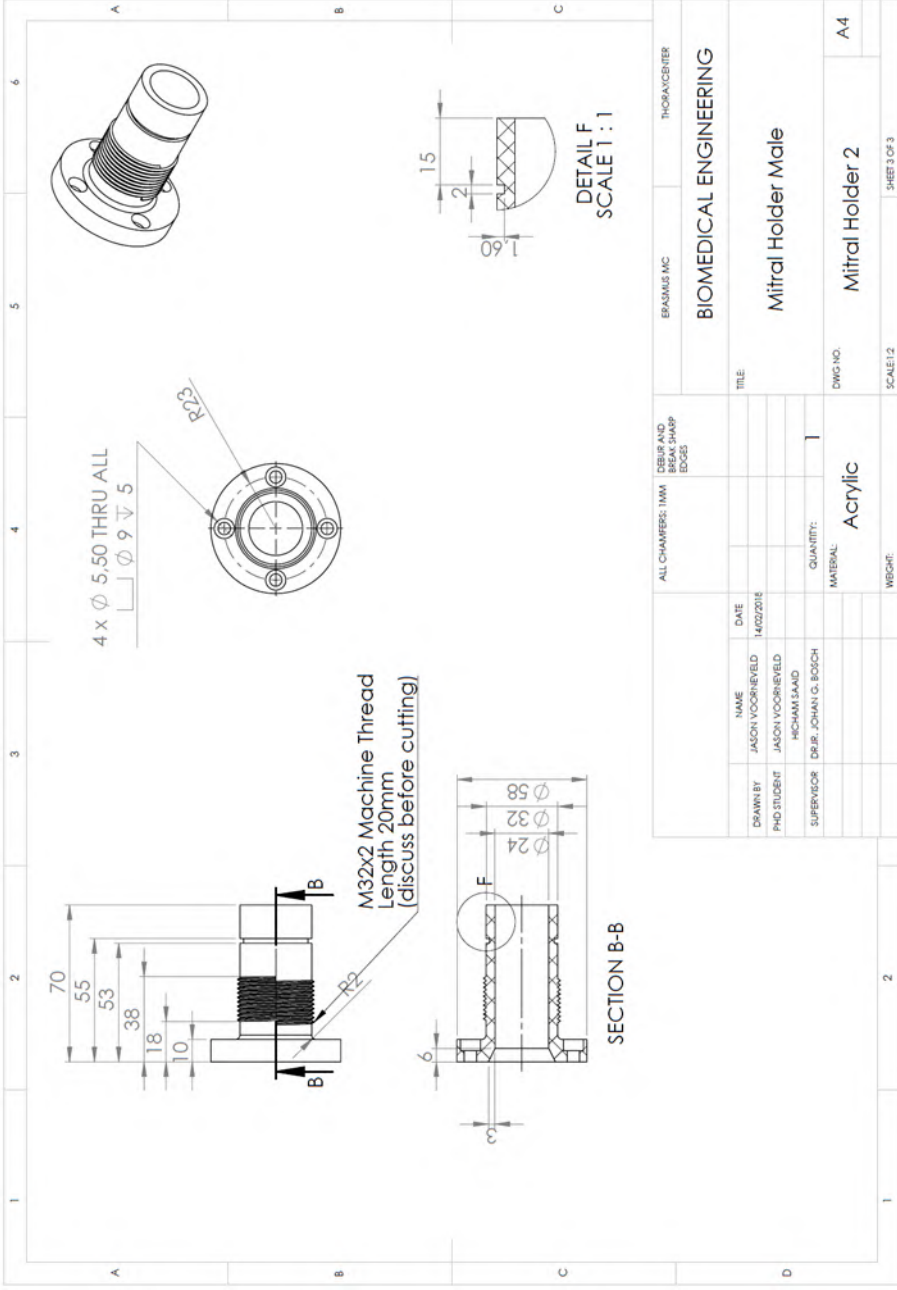


ITEM NO.	PART NUMBER	DESCRIPTION	QTY.
1	Mitral Female		1
2	Mitral Valve		1
3	o'ring 28x2		3
4	Mitral Male		1

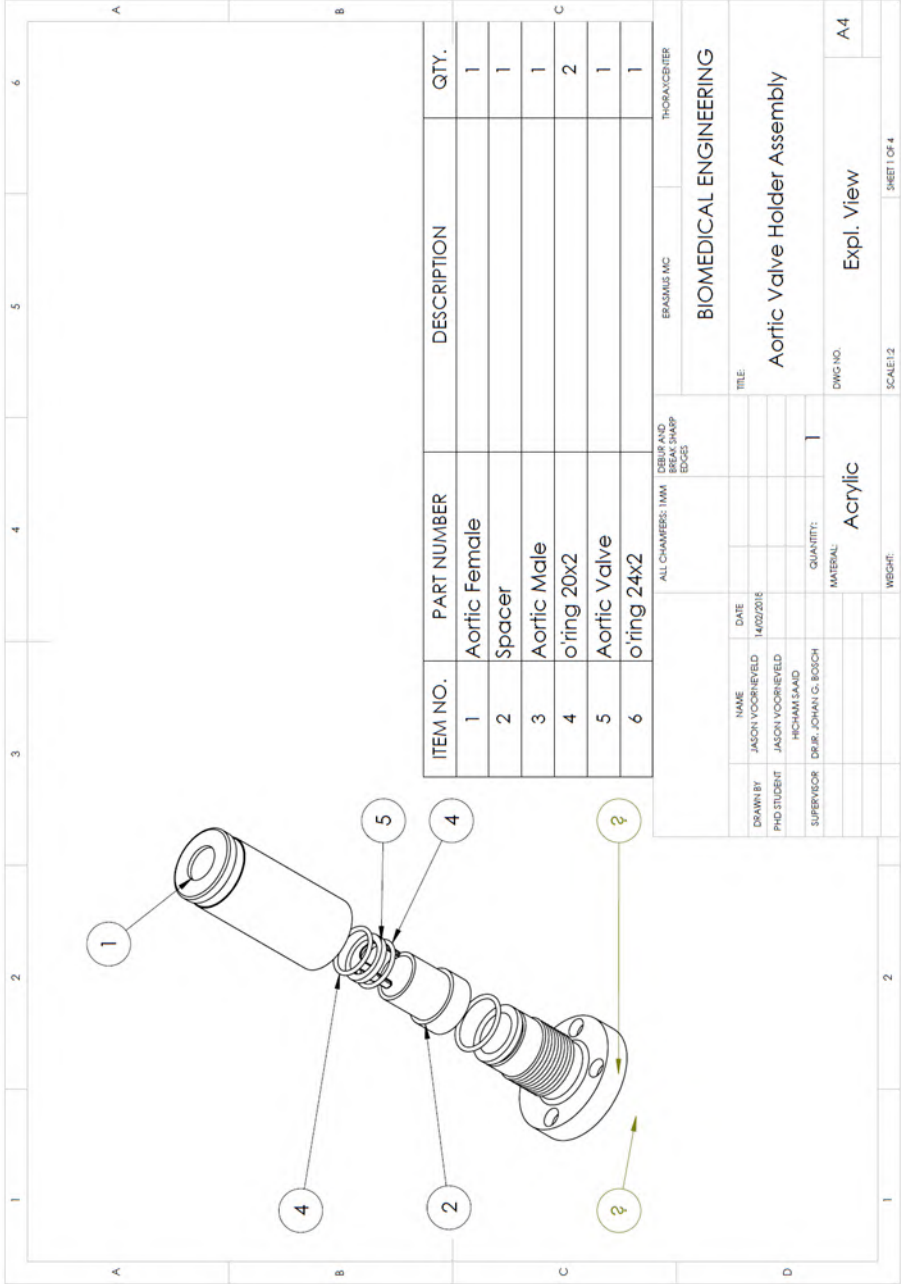
ALL CHAMFERS: 1MM		DEBUR AND BREAK SHARP EDGES		ERASMUS INC		THORACICENTER	
BIOMEDICAL ENGINEERING							
DRAWN BY: JASON VOORRIEVELD				DATE: 14/02/2016			
PHD STUDENT: JACON VOORRIEVELD				TITLE:			
SUPERVISOR: DR. J. JOHAN G. BOOCH				Mitral Valve Holder Assembly			
				QUANTITY: 1			
				MATERIAL: Acrylic			
				DWG NO.:			
				Expl. View			
				SCALE: 1:2			
				SHEET 1 OF 3			



DRAWN BY		NAME		DATE	
PHD STUDENT		JASON VOORNVELD		14/02/2016	
SUPERVISOR		DR. J. JOHAN G. BOGCH		QUANTITY: 1	
MATERIAL:		Acrylic		DWG NO.	
WEIGHT:		Mitral Valve Holder 1		A4	
SCALE: 1:1		SHEET 2 OF 3		THORACIC CENTER	
EPASMIUS MC		BIOMEDICAL ENGINEERING			
ALL CHAMBERS: 1MM / DSEEP AND BREAK SHARP EDGES		TITLE			
SECTION A-A		Mitral Valve Holder Female			

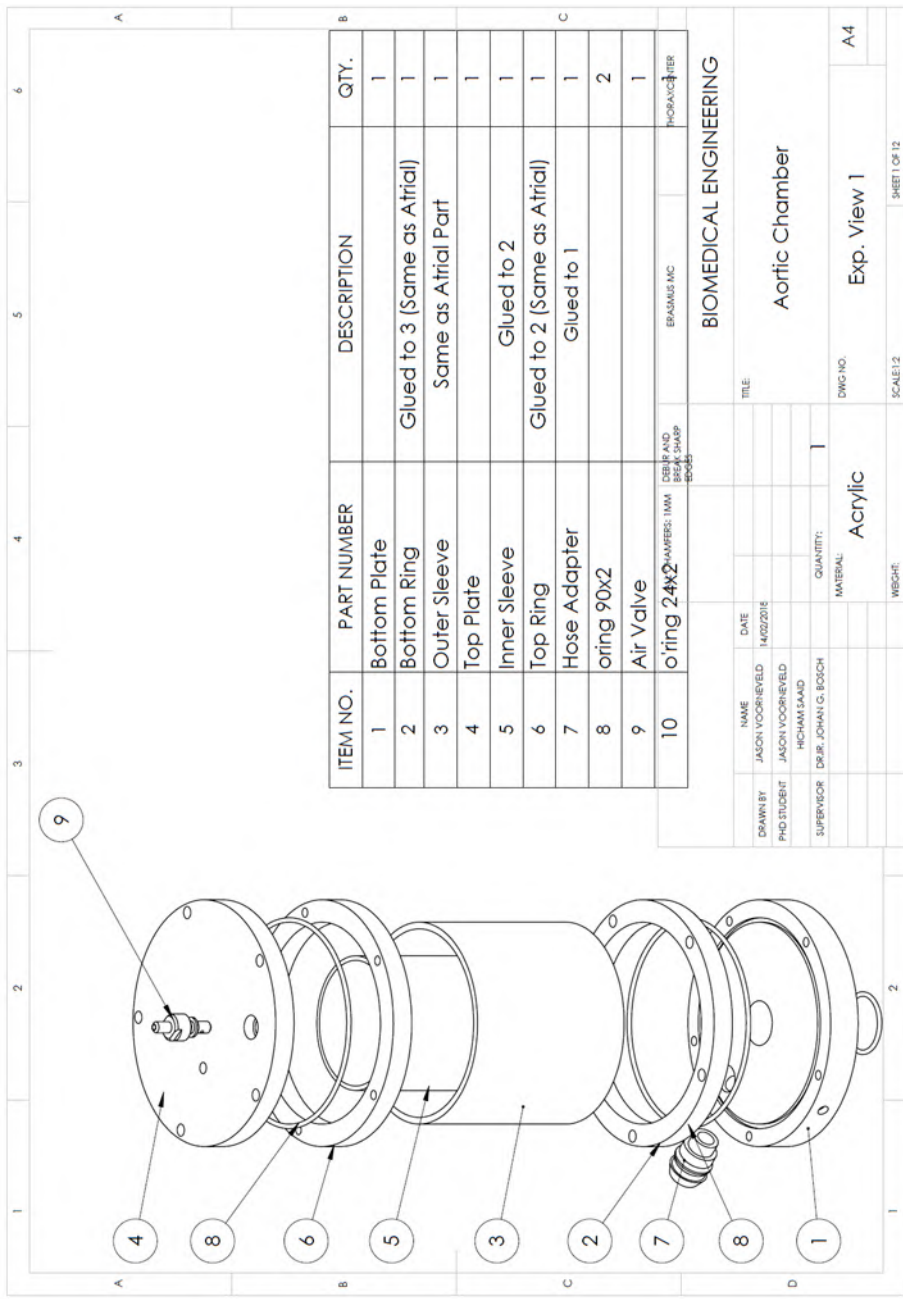


DRAWN BY PHD STUDENT SUPERVISOR		NAME JASON VOORNIEVELD JASON VOORNIEVELD HOCHAM SAND DR. J. JOHAN G. BOSCH		DATE 14/02/2016	ALL CHAMFERE: 1MM DSEEP AND BREAK SHARP EDGES		EPASULUS MC	THOKA/CENTER
TITLE BIOMEDICAL ENGINEERING								
Mitral Holder Male								
DWG NO.					Mitral Holder 2			
SCALE 1:1					A4			
MATERIAL Acrylic					SCALE 1:2			
WEIGHT					SHEET 3 OF 3			



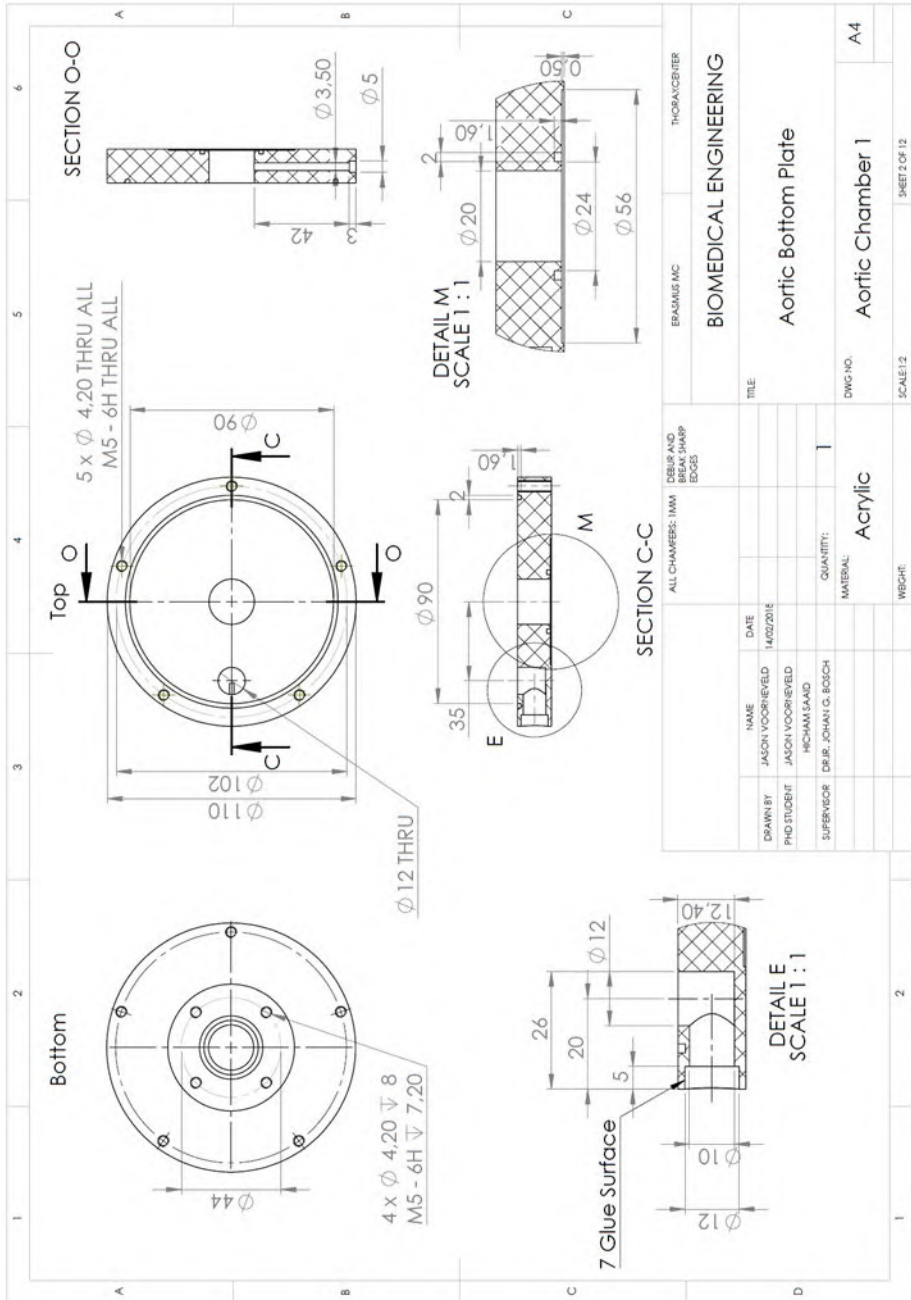
ITEM NO.	PART NUMBER	DESCRIPTION	QTY.
1	Aortic Female		1
2	Spacer		1
3	Aortic Male		1
4	O-ring 20x2		2
5	Aortic Valve		1
6	O-ring 24x2		1

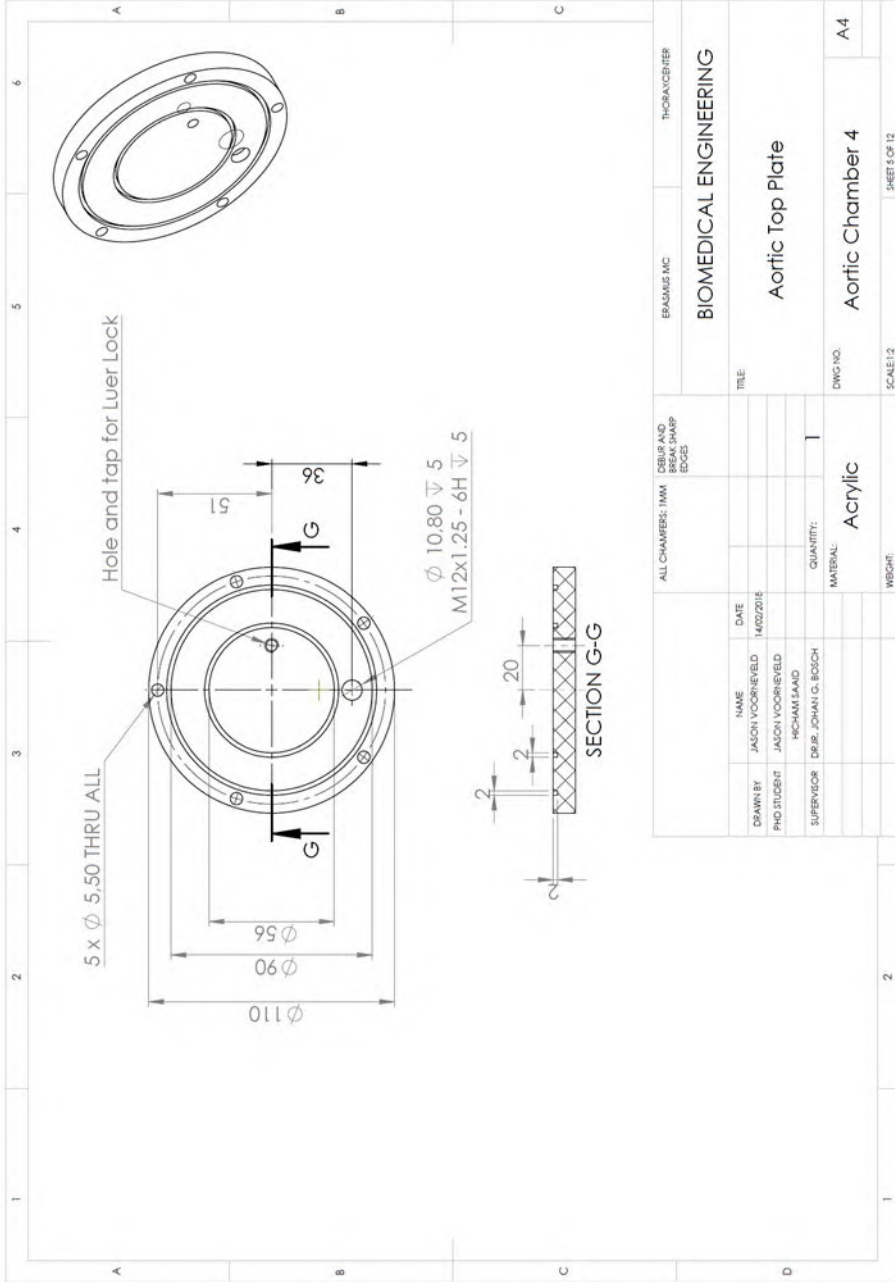
EPOSAFE, INC.		THORAN/CENTER	
BIOMEDICAL ENGINEERING			
TITLE: Aortic Valve Holder Assembly			
DRAWN BY: JASON VOORHEVELD		DATE: 14/02/2016	
PND/STUBBIT		RICHALISAARD	
SUPERVISOR: DR. J. JOHAN G. BOSCH		QUANTITY: 1	
		MATERIAL: Acrylic	
		DWG. NO.:	
		Expl. View	
		SCALE: 1:1	
		SHEET 1 OF 4	



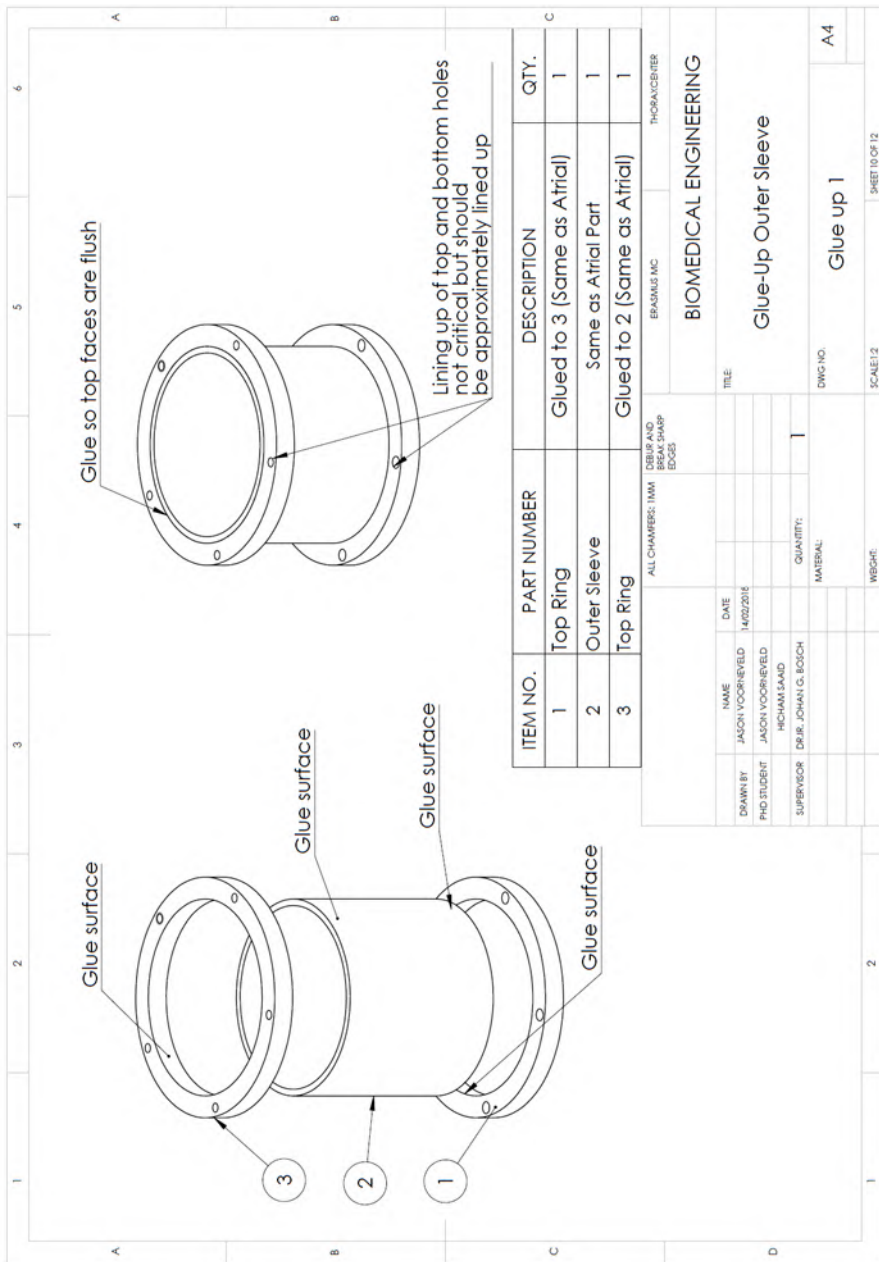
ITEM NO.	PART NUMBER	DESCRIPTION	QTY.
1	Bottom Plate		1
2	Bottom Ring	Glued to 3 (Same as Atrial)	1
3	Outer Sleeve	Same as Atrial Part	1
4	Top Plate		1
5	Inner Sleeve	Glued to 2	1
6	Top Ring	Glued to 2 (Same as Atrial)	1
7	Hose Adapter	Glued to 1	1
8	oring 90x2		2
9	Air Valve		1
10	oring 24x2		1

DRAWN BY PHD STUDENT SUPERVISOR		NAME JASON VOORNEVELD JASON VOORNEVELD RICHAM SAAD DR. J. JOHAN G. BOCH		DATE M02/2016	
TITLE		BIOMEDICAL ENGINEERING			
Dwg No.		Aortic Chamber			
Quantity		1			
Material		Acrylic			
Scale		Exp. View 1		A4	
Sheet		SHEET 1 OF 12			



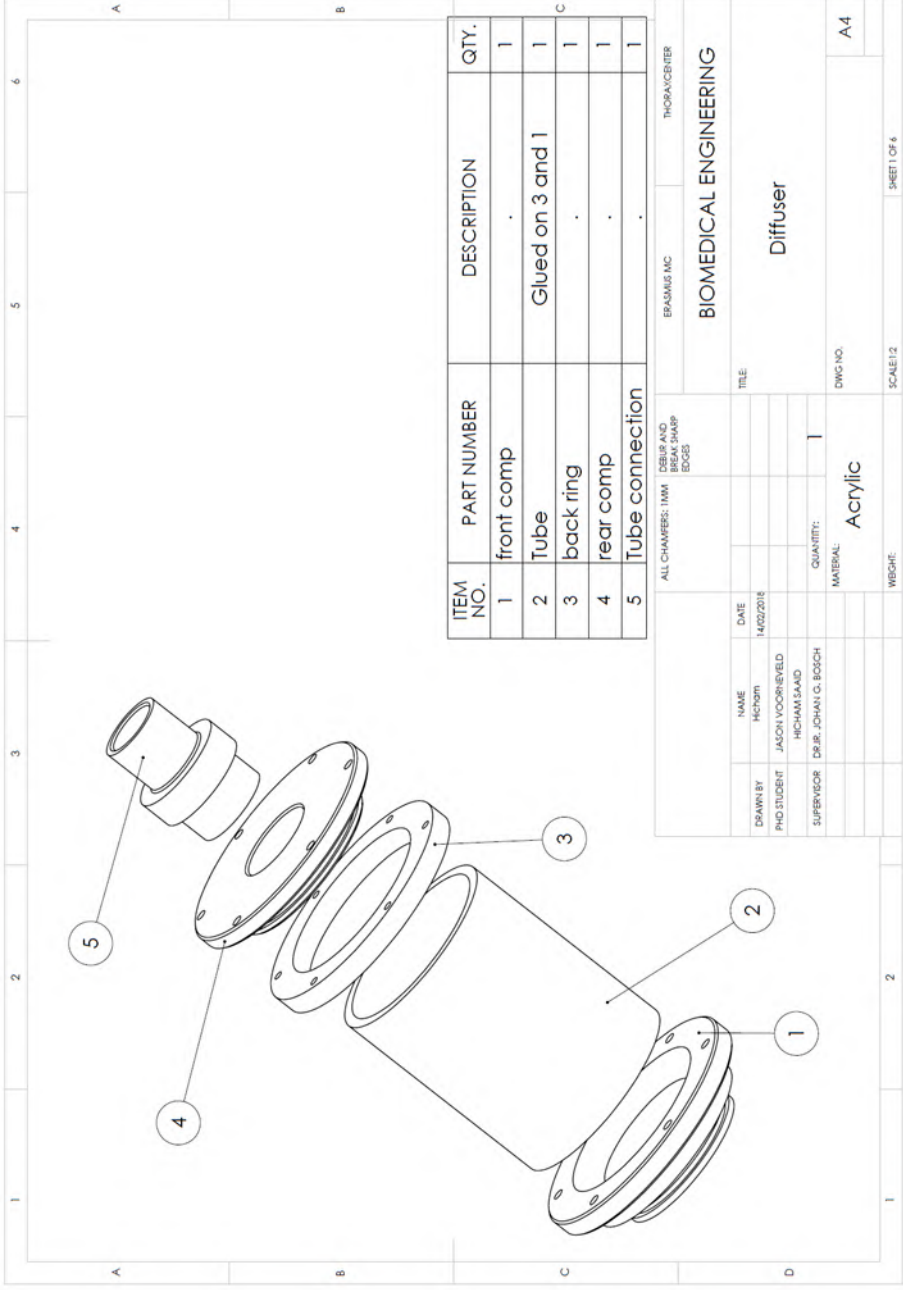


EBS&S MC		THORACENTER	
BIOMEDICAL ENGINEERING			
TITLE: Aortic Top Plate			
DWG NO: Aortic Chamber 4			
SCALE: 1:2			
SHEET 5 OF 12			
ALL CHAMBERS: 1MM		DEBUR AND BREAK SHARP EDGES	
DRAWN BY	NAME	DATE	
JASON VOORRIEVELD	JASON VOORRIEVELD	14/02/2016	
PRO STUDENT	JASON VOORRIEVELD		
	HICHAM MAAD		
SUPERVISOR	DR. JOHAN G. BOSCH	QUANTITY:	1
		MATERIAL:	Acrylic
		WGT:	



ITEM NO.	PART NUMBER	DESCRIPTION	QTY.
1	Top Ring	Glued to 3 (Same as Atrial)	1
2	Outer Sleeve	Same as Atrial Part	1
3	Top Ring	Glued to 2 (Same as Atrial)	1

ALL CHAMBERS: 1MM		DIBLUP AND BREAK SHARP EDGES		EBC303US MC		THORACIC/BIB	
BIOMEDICAL ENGINEERING							
Glue-up Outer Sleeve							
DRAWN BY	NAME	DATE	TITLE				
PHD.TJUBERT	JASON VOORNEVELD	14/02/2016					
SUPERVISOR	DR. J. CHAN G. BOCH	QUANTITY:	DWC NO.				
	RICHARD SAAD	1	A4				
		MATERIAL:	SCALE: 1:2				
			SHEET 10 OF 12				



ITEM NO.	PART NUMBER	DESCRIPTION	QTY.
1	front comp	.	1
2	Tube	Glued on 3 and 1	1
3	back ring	.	1
4	rear comp	.	1
5	Tube connection	.	1

DRAWN BY PND STUBBT		NAME Hicham	DATE 14/02/2018
DESIGNED BY JACH VOORVELD		NAME HICHAM SAAD	DATE
SUPERVISOR DR. J. JHANI G. BOSCH		NAME DR. J. JHANI G. BOSCH	DATE
QUANTITY: 1		MATERIAL: Acrylic	DWG NO. A4
TITLE: Diffuser		SCALE: 1:1	
PROJECT: BIOMEDICAL ENGINEERING		SHEET 1 OF 6	
DESIGNER: THORACBITER		DATE: 14/02/2018	

Bibliography

- [1] G. T. R Rhoades, "Medical Physiology," pp. 237–251, 2003.
- [2] J. Bermejo, P. Martínez-Legazpi, and J. C. del Álamo, "The Clinical Assessment of Intraventricular Flows," *Annu. Rev. Fluid Mech.*, vol. 47, no. 1, pp. 315–342, 2015.
- [3] J. Erb, "Basic principles of physics in echocardiographic imaging and Doppler techniques," *Cambridge Univ. Press 2010.*, vol. section 1-, pp. 13–33, 2010.
- [4] F. A. Uejima T, Koike A, Sawada H, Aizawa T, Ohtsuki S, Tanaka M, Furukawa T, "A new echocardiographic method for identifying vortex flow in the left ventricle: numerical validation," *Ultrasound Med. Biol.*, vol. 36, no. 5, pp. 772–788, 2010.
- [5] M. Crapper and T. Bruce, "Flow field visualization of sediment-laden flow using ultrasonic imaging," *Dyn. Atmos. Ocean.*, pp. 233–245, 2000.
- [6] H. B. Kim, J. R. Hertzberg, and R. Shandas, "Development and validation of echo PIV," *Exp. Fluids*, vol. 36, pp. 455–462, 2004.
- [7] G. Kheradvar, Arash , Pedrizzetti, *Vortex Formation in the Cardiovascular System*. Springer London Dordrecht Heidelberg New York, 2012.
- [8] P. Dyverfeldt, M. Bissell, A. J. Barker, A. F. Bolger, C.-J. Carlhäll, T. Ebberts, C. J. Francios, A. Frydrychowicz, J. Geiger, D. Giese, M. D. Hope, P. J. Kilner, S. Kozerke, S. Myerson, S. Neubauer, O. Wieben, and M. Markl, "4D flow cardiovascular magnetic resonance consensus statement.," *J. Cardiovasc. Magn. Reson.*, vol. 17, no. 1, p. 72, 2015.
- [9] P. P. Sengupta, G. Pedrizzetti, P. J. Kilner, A. Kheradvar, T. Ebberts, G. Tonti, A. G. Fraser, and J. Narula, "Emerging trends in CV flow visualization," *JACC Cardiovasc. Imaging*, vol. 5, no. 3, pp. 305–316, 2012.
- [10] S. Peir, Joaquim. Spencer, "finite difference, finite element and finite volume methods for partial differential equations.," *Handb. Mater. Model. Vol. I Methods Model.*, vol. M, pp. 1–32, 2005.
- [11] V. P. Vierendeels J A, Rienslagh, K and E. Dick, "Computer Simulation of Intraventricular Flow and Pressure gradient during diastole," *J. Biomech. Eng.*, vol. 122, no. December 2000, pp. 667–674, 2000.
- [12] B. Baccani, F. Domenichini, and G. Pedrizzetti, "Vortex dynamics in a model left ventricle during filling," *Eur. J. Mech. B/Fluids*, vol. 21, no. 5, pp. 527–543, 2002.
- [13] F. Domenichini, G. Pedrizzetti, and B. Baccani, "Three-dimensional filling flow into a model left ventricle," *J. Fluid Mech.*, vol. 539, no. -1, p. 179, 2005.
- [14] B. Baccani, F. Domenichini, and G. Pedrizzetti, "Model and influence of mitral valve opening during the left ventricular filling," *J. Biomech.*, vol. 36, pp. 355–361, 2003.

- [15] G. Pedrizzetti and F. Domenichini, "Left Ventricular Fluid Mechanics: The Long Way from Theoretical Models to Clinical Applications," *Ann. Biomed. Eng.*, vol. 43, no. 1, pp. 26–40, 2014.
- [16] R. Mittal, J. H. Seo, V. Vedula, Y. J. Choi, H. Liu, H. H. Huang, S. Jain, L. Younes, T. Abraham, and R. T. George, "Computational modeling of cardiac hemodynamics: Current status and future outlook," *J. Comput. Phys.*, vol. 305, pp. 1065–1082, 2016.
- [17] A. Pasipoularides, *Heart 's Vortex: Intracardiac Blood Flow Phenomena*. People's Medical Publishing House, 2010.
- [18] C. J. Carlhäll and A. Bolger, "Passing strange flow in the failing ventricle," *Circ. Hear. Fail.*, vol. 3, no. 2, pp. 326–331, 2010.
- [19] B. J. B. & F. H. Ellhouse, "Fluid Mechanics of the Mitral Valve," *Nature*, vol. 224, pp. 615–616, 1969.
- [20] H. Reul, N. Talukder, and E. W. Muller, "Fluid mechanics of the natural mitral valve," *J. Biomech.*, vol. 14, no. 5, pp. 361–372, 1981.
- [21] S. Beppu, S. Izumi, K. Miyatake, S. Nagata, Y.-D. Park, H. Sakakibara, and Y. Nimura, "Abnormal Blood Pathways in Left Ventricular Cavity in Acute Myocardial Infarction," *Circulation*, vol. 78, no. 1, pp. 157–165, 1988.
- [22] Kim WY et al., "Two-dimensional mitral flow velocity profiles in pig models using epicardial doppler echocardiography," *J. Am. Coll. Cardiol.*
- [23] W. Y. Kim, P. G. Walker, E. M. Pedersen, J. K. Poulsen, S. Oyre, K. Houliind, and A. P. Yoganathan, "Left ventricular blood flow patterns in normal subjects: A quantitative analysis by three-dimensional magnetic resonance velocity mapping," *J. Am. Coll. Cardiol.*, vol. 26, no. 1, pp. 224–238, 1995.
- [24] P. J. Kilner, G. Yang, A. J. Wilkes, R. H. Mohiaddin, D. N. Firmin, and M. H. Yacoub, "Asymmetric redirection of flow through the heart," pp. 759–761, 2000.
- [25] M. Gharib, E. Rambod, A. Kheradvar, D. J. Sahn, and J. O. Dabiri, "Optimal vortex formation as an index of cardiac health.," *Proc. Natl. Acad. Sci. U. S. A.*, vol. 103, no. 16, pp. 6305–6308, 2006.
- [26] J. O. Dabiri, "Optimal Vortex Formation as a Unifying Principle in Biological Propulsion," *Annu. Rev. Fluid Mech.*, vol. 41, no. 1, pp. 17–33, 2009.
- [27] G. R. Hong, G. Pedrizzetti, G. Tonti, P. Li, Z. Wei, J. K. Kim, A. Baweja, S. Liu, N. Chung, H. Houle, J. Narula, and M. A. Vannan, "Characterization and quantification of vortex flow in the human left ventricle by contrast echocardiography using vector particle image velocimetry," *JACC Cardiovasc Imaging*, vol. 1, no. 6, pp. 705–717, 2008.
- [28] R. Adrian, "Particle-Imaging Techniques For Experimental Fluid-Mechanics," *Annu. Rev. Fluid Mech.*, vol. 23, no. 1, pp. 261–304, 1991.
- [29] R. J. Adrian, "Multi-point optical measurements of simultaneous vectors in unsteady flow-a review," *Int. J. Heat Fluid Flow*, vol. 7, no. 2, pp. 127–145, 1986.
- [30] J. Westerweel, "Digital particle image velocimetry: Theory and application," Delft University of Technology.
- [31] C. E. Willert and M. Gharib, "Experiments in Fluids Digital particle image velocimetry," *Exp. Fluids*, vol. 193, pp. 181–193, 1991.
- [32] D. Dabiri, "Digital particle image thermometry / velocimetry : A review . Exp Digital

- particle image thermometry / velocimetry : a review,” *Exp. Fluids*, vol. 46, no. May, pp. 191–241, 2014.
- [33] R. D. Keane and R. J. Adrian, “Optimization of particle image velocimeters: II. Multiple pulsed systems,” *Meas. Sci. Technol.*, vol. 963, no. 2, pp. 963–974.
- [34] J. F. F. Cameron Tropea, Alexander L. Yarin, *Springer Handbook of Experimental Fluid Mechanics*. .
- [35] M. Raffel, C. E. Willert, F. Scarano, and C. J. Kähler, *Particle Image Velocimetry A Practical Guide. Third Edition*. Springer Berlin Heidelberg, 2017.
- [36] C. Willert, “Stereoscopic digital particle image velocimetry for application in wind tunnel flows,” *Meas. Sci. Technol.*, vol. 1465, pp. 1465–1479.
- [37] a. K. Prasad, “Stereoscopic particle image velocimetry,” *Exp. Fluids*, vol. 29, no. 2, pp. 103–116, 2000.
- [38] A. K. Prasad and K. Jensen, “Scheimpflug stereocamera for particle image velocimetry in liquid flows,” *Appl. Opt.*, vol. 34, no. 30, pp. 7093–7099, 1995.
- [39] S. M. Soloff, R. J. Adrian, and Z.-C. Liu, “Distortion compensation for generalized stereoscopic particle image velocimetry,” *Meas. Sci. Technol.*, vol. 8, no. 12, pp. 1441–1454, 1997.
- [40] Z. Liu, Y. Zheng, L. Jia, J. Jiao, and Q. Zhang, “Stereoscopic PIV studies on the swirling flow structure in a gas cyclone,” *Chem. Eng. Sci.*, vol. 61, pp. 4252–4261, 2006.
- [41] B. Wieneke, “Stereo-PIV using self-calibration on particle images,” *Exp. Fluids*, vol. 39, no. 2, pp. 267–280, 2005.
- [42] J. C. J. Kahler, Kompenhans, “Fundamentals of multiple plane stereo particle image velocimetry,” *Exp. Fluids*, pp. 70–77, 2000.
- [43] J. A. Mullin and W. J. A. Dahm, “Dual-plane stereo particle image velocimetry (DSPIV) for measuring velocity gradient fields at intermediate and small scales of turbulent flows,” *Exp. Fluids*, vol. 38, no. 2, pp. 185–196, 2005.
- [44] H. Hu and T. Saga, “Dual-Plane Stereoscopic PIV Measurements in a Lobed Jet Mixing Flow,” *Am. Inst. Aeronaut. Astronaut.*, no. January, pp. 1–17, 2005.
- [45] T. Hori and J. Sakakibara, “High-speed scanning stereoscopic PIV for 3D vorticity measurement in liquids,” *Meas. Sci. Technol.*, vol. 15, no. 6, pp. 1067–1078, 2004.
- [46] R. Watanabe, T. Gono, T. Yamagata, and N. Fujisawa, “Three-dimensional flow structure in highly buoyant jet by scanning stereo PIV combined with POD analysis,” *Int. J. Heat Fluid Flow*, vol. 52, pp. 98–110, 2015.
- [47] D. Hess and J. Kitzhofer, “Single-view volumetric PIV via high-resolution scanning, isotropic voxel restructuring and 3D least-squares matching,” *Meas. Sci. Technol.*, vol. 23, 2012.
- [48] Q. Gao, H. Wang, and G. Shen, “Review on development of volumetric particle image velocimetry,” *Chinese Sci. Bull.*, vol. 58, no. 36, pp. 4541–4556, 2013.
- [49] G. E. Elsinga, F. Scarano, B. Wieneke, and B. W. van Oudheusden, “Tomographic particle image velocimetry,” *6th Int. Symp. Part. Image Velocim.*, pp. 1–12, 2005.
- [50] F. Scarano, “Tomographic PIV: principles and practice,” *Meas. Sci. Technol.*, vol. 24, no. 1, p. 012001, 2013.
- [51] D. P. S. H. G. Maas, A. Gruen, “Particle tracking velocimetry in three-dimensional

- flows,” *Exp. Fluids*, vol. 146, pp. 133–146, 1993.
- [52] D. Schanz, S. Gesemann, and A. Schröder, “Shake - The - Box : Lagrangian particle tracking at high particle image densities,” *Exp. Fluids*, vol. 57, no. 5, pp. 1–27, 2016.
- [53] H. Meng, G. Pan, Y. Pu, and S. H. Woodward, “Holographic particle image velocimetry: from film to digital recording,” *Meas. Sci. Technol.*, vol. 15, no. 4, pp. 673–685, 2004.
- [54] M. S. Chong, A. E. Perry, and B. J. Cantwell, “A general classification of three-dimensional flow fields,” *Phys. Fluids A Fluid Dyn.*, vol. 2, no. 5, pp. 765–777, 1990.
- [55] F. Pereira, M. Gharib, D. Dabiri, and D. Modarress, “Defocusing digital particle image velocimetry: a 3-component 3-dimensional DPIV measurement technique . Application to bubbly flows,” *Exp. Fluids*, pp. s78–s84, 2000.
- [56] K. Lynch, “Three-Dimensional Particle Image Velocimetry Using a Plenoptic Camera,” *50th AIAA Aerosp. Sci. Meet. Incl. New Horizons Forum Aerosp. Expo. 09 - 12 January 2012, Nashville, Tennessee*, pp. 1–14, 2012.
- [57] F. Scarano and C. Poelma, “Three-dimensional vorticity patterns of cylinder wakes,” *Exp. Fluids*, vol. 47, no. 1, pp. 69–83, 2009.
- [58] F. J. W. A. Martins, J. Foucaut, L. Thomas, J. Belden, T. T. Truscott, M. C. Axiak, S. Ghaemi, and F. Scarano, “Multi-pass light amplification for tomographic particle image velocimetry.”
- [59] G. T. Herman and A. Lent, “Iterative reconstruction algorithms,” *Comput. Med. Imaging Graph.*, vol. 6, no. 3, pp. 273–294, 1976.
- [60] G. E. Elsinga, “Tomographic particle image velocimetry,” Technische Universiteit Delft, 2008.
- [61] B. Wieneke, “Volume self-calibration for 3D particle image velocimetry,” *Exp. Fluids*, pp. 549–556, 2008.
- [62] G. E. Elsinga, J. Westerweel, F. Scarano, and M. Novara, “On the velocity of ghost particles and the bias errors in Tomographic-PIV,” *Exp. Fluids*, vol. 50, pp. 825–838, 2011.
- [63] C. Atkinson and Æ. J. Soria, “An efficient simultaneous reconstruction technique for tomographic particle image velocimetry,” *Exp. Fluids*, vol. 47, pp. 553–568, 2009.
- [64] M. Novara, K. J. Batenburg, and F. Scarano, “Motion tracking-enhanced MART for tomographic PIV,” *Meas. Sci. Technol.*, vol. 21, 2010.
- [65] G. Pedrizzetti, G. La Canna, O. Alfieri, and G. Tonti, “The vortex--an early predictor of cardiovascular outcome?,” *Nat. Rev. Cardiol.*, vol. 11, no. 9, pp. 545–53, 2014.
- [66] J. Eriksson, *Quantification of 4D Left Ventricular Blood Flow in Health and Disease*, no. 1374. 2013.
- [67] J. Bermejo, Y. Benito, M. Alhama, R. Yotti, P. Martínez-Legazpi, C. Pérez Del Villar, E. Pérez-David, A. González-Mansilla, C. Santa-Marta, A. Barrio, F. Fernández-Avilés, and J. C. Del Alamo, “Intraventricular vortex properties in non-ischemic dilated cardiomyopathy,” *Am. J. Physiol. Heart Circ. Physiol.*, pp. 718–729, 2014.
- [68] A. F. Bolger, E. Heiberg, M. Karlsson, L. Wigstrom, J. Engvall, A. Sigfridsson, T. Ebbers, J. P. Kvitting, C. J. Carlhall, and B. Wranne, “Transit of blood flow through the human left ventricle mapped by cardiovascular magnetic resonance,” *J Cardiovasc Magn Reson*, vol. 9, no. 5, pp. 741–747, 2007.
- [69] G. Pedrizzetti and F. Domenichini, “Nature optimizes the swirling flow in the human

- left ventricle,” *Phys. Rev. Lett.*, vol. 95, no. 10, pp. 1–4, 2005.
- [70] R. Faludi, M. Szulik, J. D’hooge, P. Herijgers, F. Rademakers, G. Pedrizzetti, and J. U. Voigt, “Left ventricular flow patterns in healthy subjects and patients with prosthetic mitral valves: An in vivo study using echocardiographic particle image velocimetry,” *J. Thorac. Cardiovasc. Surg.*, vol. 139, no. 6, pp. 1501–1510, 2010.
- [71] F. Sotiropoulos, T. B. Le, and A. Gilmanov, “Fluid Mechanics of Heart Valves and Their Replacements,” *Annu. Rev. Fluid Mech.*, vol. 48, no. 1, pp. 259–283, 2016.
- [72] O. Pierrakos, P. P. Vlachos, and D. P. Telionis, “Time-resolved DPIV analysis of vortex dynamics in a left ventricular model through bileaflet mechanical and porcine heart valve prostheses,” *J. Biomech. Eng.*, vol. 126, no. 6, pp. 714–726, 2004.
- [73] T. Akutsu and T. Fukuda, “Time-resolved particle image velocimetry and laser doppler anemometry study of the turbulent flow field of bileaflet mechanical mitral prostheses,” *J. Artif. Organs*, vol. 8, no. 3, pp. 171–183, 2005.
- [74] M. Y. Yousif, D. W. Holdsworth, and T. L. Poepping, “A blood-mimicking fluid for particle image velocimetry with silicone vascular models,” *Exp. Fluids*, vol. 50, no. 3, pp. 769–774, 2011.
- [75] M. R. Najjari, J. A. Hinke, K. V. Bulusu, and M. W. Plesniak, “On the rheology of refractive-index-matched, non-Newtonian blood-analog fluids for PIV experiments,” *Exp. Fluids*, vol. 57, no. 6, pp. 1–6, 2016.
- [76] A. K. Prasad, “Particle Image Velocimetry,” *Curr. Sci.*, vol. 79, no. 1, pp. 51–60, 2000.
- [77] T. Yagi, W. Yang, D. Ishikawa, K. Iwasaki, and M. Umezu, “Stereoscopic Particle Image Velocimetry for Application in Three-dimensional Flow within a Spiral Vortex Pulsatile Blood Pump,” *Biocybern. Biomed. Eng.*, vol. 26, no. 2, pp. 53–62, 2006.
- [78] T. Yagi, W. Yang, and M. Umezu, “Effect of bileaflet valve orientation on the 3d flow dynamics in the sinus of valsalva,” *J. Biomech. Sci. Eng.*, vol. 6, no. 2, pp. 64–78, 2011.
- [79] N. A. Buchmann, C. Atkinson, M. C. Jeremy, and J. Soria, “Tomographic particle image velocimetry investigation of the flow in a modeled human carotid artery bifurcation,” *Exp. Fluids*, vol. 50, no. 4, pp. 1131–1151, 2011.
- [80] J. Westerweel and F. Scarano, “Universal outlier detection for PIV data,” *Exp. Fluids*, vol. 39, no. 6, pp. 1096–1100, 2005.
- [81] J. Jeong and F. Hussain, “On the identification of a vortex,” *J. Fluid Mech.*, vol. 285, no. -1, p. 69, 1995.
- [82] G. L. Van Rijk-Zwikker, B. J. Delemarre, and H. a Huysmans, “The orientation of the bi-leaflet CarboMedics valve in the mitral position determines left ventricular spatial flow patterns,” *Eur. J. Cardiothorac. Surg.*, vol. 10, no. 7, pp. 513–20, 1996.
- [83] G. Querzoli and S. Fortini, “Effect of the prosthetic mitral valve on vortex dynamics and turbulence of the left ventricular flow,” no. April, 2010.
- [84] J. C. Westerdale, R. Adrian, K. Squires, H. Chaliki, and M. Belohlavek, “Effects of Bileaflet Mechanical Mitral Valve Rotational Orientation on Left Ventricular Flow Conditions,” *Open Cardiovasc. Med. J.*, vol. 9, no. September, pp. 62–68, 2015.
- [85] R. J. Geest and P. Garg, “Advanced Analysis Techniques for Intra- cardiac Flow Evaluation from 4D Flow MRI,” *Curr. Radiol. Rep.*, no. July, 2016.
- [86] T. Akutsu and T. Masuda, “Three-dimensional flow analysis of a mechanical bileaflet mitral prosthesis,” *J. Artif. Organs*, vol. 6, no. 2, pp. 112–23, 2003.

- [87] Y. J. Choi, V. Vedula, and R. Mittal, "Computational study of the dynamics of a bileaflet mechanical heart valve in the mitral position," *Ann. Biomed. Eng.*, vol. 42, no. 8, pp. 1668–1680, 2014.
- [88] J. C. Westerdale, R. Adrian, K. Squires, H. Chaliki, and M. Belohlavek, "Effects of Bileaflet Mechanical Mitral Valve Rotational Orientation on Left Ventricular Flow Conditions," *Open Cardiovasc. Med. J.*, vol. 9, pp. 62–68, 2015.
- [89] C. M. De Silva, J. Philip, and I. Marusic, "Minimization of divergence error in volumetric velocity measurements and implications for turbulence statistics," *Exp. Fluids*, vol. 54, no. 7, 2013.
- [90] R. M. Lang, M. Bierig, R. B. Devereux, F. A. Flachskampf, E. Foster, P. A. Pellikka, M. H. Picard, M. J. Roman, J. Seward, J. S. Shanewise, S. D. Solomon, K. T. Spencer, M. St John Sutton, and W. J. Stewart, "Recommendations for chamber quantification: A report from the American Society of Echocardiography's guidelines and standards committee and the Chamber Quantification Writing Group, developed in conjunction with the European Association of Echocardiograph," *J. Am. Soc. Echocardiogr.*, vol. 18, no. 12, pp. 1440–1463, 2005.
- [91] T. L. Narrow, M. Yoda, and S. I. Abdel-Khalik, "A simple model for the refractive index of sodium iodide aqueous solutions," *Exp. Fluids*, vol. 28, no. 3, pp. 282–283, 2000.
- [92] S. Fortini, G. Querzoli, S. Espa, and a. Cenedese, "Three-dimensional structure of the flow inside the left ventricle of the human heart," *Exp. Fluids*, vol. 54, no. 11, 2013.
- [93] D. Mele, V. Smarrazzo, G. Pedrizzetti, F. Capasso, M. Pepe, S. Severino, G. A. Luisi, M. Maglione, and R. Ferrari, "Intracardiac Flow Analysis: Techniques and Potential Clinical Applications," *J. Am. Soc. Echocardiogr.*, 2018.
- [94] D. R. Muñoz, M. Markl, J. L. M. Mur, A. Barker, C. Fernández-Golfín, P. Lancellotti, and J. L. Z. Gómez, "Intracardiac flow visualization: Current status and future directions," *European Heart Journal Cardiovascular Imaging*, vol. 14, no. 11. pp. 1029–1038, 2013.
- [95] N. S. V Vraghav , Sudeep Sastry, "Experimental Assessment of Flow Fields Associated with Heart Valve Prostheses Using Particle Image Velocimetry (PIV): Recommendations for Best Practices," *Cardiovasc. Eng. Technol.*, vol. 9, no. 3, pp. 273–287, 2018.
- [96] M. Belohlavek, "Vortex formation time: An emerging echocardiographic index of left ventricular filling efficiency?," *Eur. Heart J. Cardiovasc. Imaging*, vol. 13, no. 5, pp. 367–369, 2012.
- [97] G. I. P. Pedrizzetti, F. E. D. Omenichini, and G. T. Tonti, "On the Left Ventricular Vortex Reversal after Mitral Valve Replacement," *Ann. Biomed. Eng.*, vol. 38, no. 3, pp. 769–773, 2010.
- [98] K. Akiyama, N. Nakamura, K. Itatani, Y. Naito, M. Kinoshita, M. Shimizu, S. Hamaoka, H. Kato, H. Yasumoto, Y. Nakajima, T. Mizobe, S. Numata, H. Yaku, and T. Sawa, "Flow-dynamics assessment of mitral-valve surgery by intraoperative vector flow mapping," *Interact. Cardiovasc. Thorac. Surg.*, vol. 24, no. February, pp. 869–875, 2017.
- [99] Chikwe, "Prosthesis Type for Aortic- and Mitral-Valve Replacement," *N. Engl. J. Med.*, pp. 776–779, 2018.
- [100] Goldstone, "Mechanical or Biologic Prostheses for Aortic-Valve and Mitral-Valve

- Replacement,” *N. Engl. J. Med.*, pp. 1847–1857, 2017.
- [101] A. Falahatpisheh and A. Kheradvar, “High-speed particle image velocimetry to assess cardiac fluid dynamics in vitro: From performance to validation,” *Eur. J. Mech. B/Fluids*, vol. 35, pp. 2–8, 2012.
- [102] I. U. Okafor, A. Santhanakrishnan, B. D. Chaffins, L. Mirabella, J. N. Oshinski, and A. P. Yoganathan, “Cardiovascular magnetic resonance compatible physical model of the left ventricle for multi-modality characterization of wall motion and hemodynamics,” *J. Cardiovasc. Magn. Reson.*, vol. 17, no. 1, p. 51, 2015.
- [103] J. Wang, Q. Gao, R. Wei, and J. Wang, “Experimental study on the effect of an artificial cardiac valve on the left ventricular flow,” *Exp. Fluids*, vol. 58, no. 9, p. 126, 2017.
- [104] A. Falahatpisheh, G. Pedrizzetti, and A. Kheradvar, “Three-dimensional reconstruction of cardiac flows based on multi-planar velocity fields,” *Exp. Fluids*, vol. 55, no. 11, 2014.
- [105] S. G.-D. Tan, S. Kim, J. K. F. Hon, and H. L. Leo, “A D-Shaped Bileaflet Bioprosthesis which Replicates Physiological Left Ventricular Flow Patterns,” *PLoS One*, vol. 11, no. 6, p. e0156580, 2016.
- [106] H. Saaïd, P. Segers, M. Novara, T. Claessens, and P. Verdonck, “Single calibration multiplane stereo-PIV : the effect of mitral valve orientation on three-dimensional flow in a left ventricle model,” *Exp. Fluids*, vol. 59, no. 3, pp. 1–13, 2018.
- [107] K. P. L. F. Scarano, “An efficient and accurate approach to MTE - MART for time - resolved tomographic PIV,” pp. 1–16, 2015.
- [108] D. Hasler, A. Landolt, and D. Obrist, “Tomographic PIV behind a prosthetic heart valve,” *Exp. Fluids*, vol. 57, no. 5, pp. 1–13, 2016.
- [109] D. Hasler and D. Obrist, “Three-dimensional flow structures past a bio- prosthetic valve in an in-vitro model of the aortic root,” *PLoS One*, 2018.
- [110] C. Roloff, D. Stucht, O. Beuing, and P. Berg, “Comparison of intracranial aneurysm flow quantification techniques : standard PIV vs stereoscopic PIV vs tomographic PIV vs phase- contrast MRI vs CFD,” pp. 1–8, 2018.
- [111] H. A. Kirişli, M. Schaap, S. Klein, S. L. Papadopoulou, M. Bonardi, C. H. Chen, A. C. Weustink, N. R. Mollet, E. J. Vonken, R. J. van der Geest, T. van Walsum, and W. J. Niessen, “Evaluation of a multi-atlas based method for segmentation of cardiac CTA data: a large-scale, multicenter, and multivendor study,” *Med. Phys.*, vol. 37, no. 12, pp. 6279–6291, Nov. 2010.
- [112] C. T. Metz, N. Baka, H. Kirisli, M. Schaap, S. Klein, L. A. Neefjes, N. R. Mollet, B. Lelieveldt, M. De Bruijne, W. J. Niessen, and T. Van Walsum, “Regression-Based Cardiac Motion Prediction,” *IEEE Trans. Med. Imaging*, vol. 31, no. 6, pp. 1311–1325, 2012.
- [113] de J. N. and B. J. G. Voorneveld J., Muralidharan A., Hope T., Vos H. J., Kruizinga P., van der Steen A. F. W., Gijzen F. J. H., Kenjeres S., “High Frame Rate Ultrasound Particle Image Velocimetry for Estimating High Velocity Flow Patterns in the Left Ventricle,” *IEEE Trans. Ultrason. Ferroelectr. Freq. Control*, vol. PP, no. c, p. 1, 2018.
- [114] W. Zang and A. K. Prasad, “Performance evaluation of a Scheimpflug stereocamera for particle image velocimetry,” *Appl. Opt.*, vol. 36, no. 33, pp. 8738–8744, 1997.
- [115] A. Cenedese, Z. Del Prete, M. Miozzi, and G. Querzoli, “A laboratory investigation of the flow in the left ventricle of a human heart with prosthetic, tilting-disk valves,” *Exp.*

- Fluids*, vol. 39, no. 2, pp. 322–335, 2005.
- [116] M. Vukićević, S. Fortini, G. Querzoli, S. Espa, and G. Pedrizzetti, “Experimental study of an asymmetric heart valve prototype,” *Eur. J. Mech. B/Fluids*, vol. 35, pp. 54–60, 2012.
- [117] S. S. Khalafvand, J. D. Voorneveld, A. Muralidharan, F. J. H. Gijzen, J. G. Bosch, T. Van Walsum, A. Haak, N. De Jong, and S. Kenjeres, “Assessment of human left ventricle flow using statistical shape modelling and computational fluid dynamics,” *J. Biomech.*, vol. 74, pp. 116–125, 2018.
- [118] K. Nakashima, K. Itatani, T. Kitamura, and N. Oka, “Energy dynamics of the intraventricular vortex after mitral valve surgery,” *Heart Vessels*, vol. 0, no. 0, p. 0, 2017.
- [119] J. M. Van Dantzig, “Doppler Left Ventricular Flow Pattern Versus Conventional Predictors of Left Ventricular Thrombus After Acute Myocardial Infarction,” vol. 25, no. 6, pp. 1341–1346, 1995.
- [120] P. P. Sengupta, R. Burke, B. K. Khandheria, and M. Belohlavek, “Following the Flow in Chambers,” *Heart Fail. Clin.*, vol. 4, pp. 325–332, 2008.
- [121] S. A. H. Hendabadi, J. A. B. Ermejo, Y. O. B. Enito, R. A. Y. Otti, and S. H. C. S. Hadden, “Topology of Blood Transport in the Human Left Ventricle by Novel Processing of Doppler Echocardiography,” vol. 41, no. 12, pp. 2603–2616, 2013.
- [122] D. R. Troolin and E. K. Longmire, “Volumetric velocity measurements of vortex rings from inclined exits,” *Exp. Fluids*, vol. 48, no. 3, pp. 409–420, 2010.
- [123] H. Watanabe, S. Sugiura, and T. Hisada, “The looped heart does not save energy by maintaining the momentum of blood flowing in the ventricle,” *AJP Hear. Circ. Physiol.*, vol. 294, no. 5, pp. H2191–H2196, 2008.
- [124] T. B. Le and F. Sotiropoulos, “On the three-dimensional vortical structure of early diastolic flow in a patient-specific left ventricle,” *Eur. J. Mech. B/Fluids*, vol. 35, pp. 20–24, 2012.
- [125] S. S. Khalafvand, F. Xu, J. Westenberg, F. Gijzen, and S. Kenjeres, “Intraventricular blood flow with a fully dynamic mitral valve model,” *Comput. Biol. Med.*, vol. 104, no. November 2018, pp. 197–204, 2019.
- [126] M. S. M. Elbaz, E. E. Calkoen, J. J. M. Westenberg, B. P. F. Lelieveldt, A. A. W. Roest, and R. J. van der Geest, “Vortex flow during early and late left ventricular filling in normal subjects: quantitative characterization using retrospectively-gated 4D flow cardiovascular magnetic resonance and three-dimensional vortex core analysis,” *J. Cardiovasc. Magn. Reson.*, vol. 16, p. 78, 2014.
- [127] V. Meschini, M. D. De Tullio, G. Querzoli, and R. Verzicco, “Flow structure in healthy and pathological left ventricles with natural and prosthetic mitral valves,” pp. 271–307, 2018.
- [128] G. Pedrizzetti, A. R. Martiniello, V. Bianchi, A. D’Onofrio, P. Caso, and G. Tonti, “Cardiac fluid dynamics anticipates heart adaptation,” *J. Biomech.*, vol. 48, no. 2, pp. 388–391, 2015.
- [129] P. Martínez-Legazpi, J. Bermejo, Y. Benito, R. Yotti, C. Pérez Del Villar, A. González-Mansilla, A. Barrio, E. Villacorta, P. L. Sánchez, F. Fernández-Avilés, and J. C. Del Álamo, “Contribution of the diastolic vortex ring to left ventricular filling,” *J. Am. Coll. Cardiol.*, vol. 64, no. 16, pp. 1711–1721, 2014.
- [130] P. M. Arvidsson, S. J. Kovács, J. Töger, R. Borgquist, E. Heiberg, M. Carlsson, and H.

- Arheden, "Vortex ring behavior provides the epigenetic blueprint for the human heart.," *Sci. Rep.*, vol. 6, no. January, p. 22021, 2016.
- [131] A. Kheradvar, R. Assadi, A. Falahatpisheh, and P. P. Sengupta, "Assessment of Transmitral Vortex Formation in Patients with Diastolic Dysfunction," *J. Am. Soc. Echocardiogr.*, vol. 25, no. 2, pp. 220–227, Feb. 2012.
- [132] A. Pasipoularides, "Mechanotransduction Mechanisms for Intraventricular Diastolic Vortex Forces and Myocardial Deformations: Part 1," *J. Cardiovasc. Transl. Res.*, vol. 8, no. 1, pp. 76–87, Feb. 2015.
- [133] M. Correia, J. Provost, M. Tanter, and M. Pernot, "4D ultrafast ultrasound flow imaging: *in vivo* quantification of arterial volumetric flow rate in a single heartbeat," *Phys. Med. Biol.*, vol. 61, no. 23, pp. L48–L61, 2016.
- [134] S. Holbek, C. Ewertsen, H. Bouzari, M. J. Pihl, K. L. Hansen, M. B. Stuart, C. Thomsen, M. B. Nielsen, and J. A. Jensen, "Ultrasonic 3-D Vector Flow Method for Quantitative In Vivo Peak Velocity and Flow Rate Estimation," *IEEE Trans. Ultrason. Ferroelectr. Freq. Control*, vol. 64, no. 3, pp. 544–554, 2017.
- [135] S. Holbek, K. L. Hansen, H. Bouzari, C. Ewertsen, M. B. Stuart, C. Thomsen, M. B. Nielsen, and J. A. Jensen, "Common Carotid Artery Flow Measured by 3-D Ultrasonic Vector Flow Imaging and Validated with Magnetic Resonance Imaging," *Ultrasound Med. Biol.*, vol. 43, no. 10, pp. 2213–2220, Oct. 2017.
- [136] K. C. Assi, E. Gay, C. Chnafa, S. Mendez, F. Nicoud, J. F. P. J. Abascal, P. Lantelme, F. Tournoux, and D. Garcia, "Intraventricular vector flow mapping - A Doppler-based regularized problem with automatic model selection," *Phys. Med. Biol.*, vol. 62, no. 17, pp. 7131–7147, 2017.
- [137] D. Garcia, J. C. del Álamo, D. Tanné, R. Yotti, C. Cortina, É. Bertrand, J. C. Antoranz, E. Pérez-David, R. Rieu, F. Fernández-Avilés, and J. Bermejo, "Two-Dimensional Intraventricular Flow Mapping by Digital Processing Conventional Color-Doppler Echocardiography Images," *IEEE Trans. Med. Imaging*, vol. 29, no. 10, pp. 1701–1713, Oct. 2010.
- [138] A. Gomez, A. De Vecchi, M. Jantsch, W. Shi, K. Pushparajah, J. Simpson, N. Smith, D. Rueckert, T. Schaeffter, and G. Penney, "4D Blood Flow Reconstruction over the Entire Ventricle from Wall Motion and Blood Velocity Derived from Ultrasound Data," *IEEE Trans. Med. Imaging*, vol. 0062, no. c, pp. 1–1, 2015.
- [139] T. Grønli, M. Wiggen, P. Segers, and L. Lovstakken, "A fast 4D B-spline framework for model-based reconstruction and regularization in vector flow imaging," *IEEE Int. Ultrason. Symp. IUS*, vol. 1, no. 1, pp. 2–5, 2018.
- [140] S. Fadnes, M. S. Wiggen, S. A. Nyrrnes, and L. Lovstakken, "In Vivo Intracardiac Vector Flow Imaging Using Phased Array Transducers for Pediatric Cardiology," *IEEE Trans. Ultrason. Ferroelectr. Freq. Control*, vol. 64, no. 9, pp. 1318–1326, Sep. 2017.
- [141] M. S. Wiggen, S. Fadnes, A. Rodriguez-Molares, T. Bjastad, M. Eriksen, K. H. Stensaeth, A. Stoylen, and L. Lovstakken, "4D Intracardiac Ultrasound Vector Flow Imaging - Feasibility and Comparison to Phase-Contrast MRI," *IEEE Trans. Med. Imaging*, no. c, 2018.
- [142] H. Gao, N. Bijmens, D. Coisne, M. Lugiez, M. Rutten, and J. D'hooge, "2-D Left

- Ventricular Flow Estimation by Combining Speckle Tracking With Navier–Stokes-Based Regularization: An In Silico, In Vitro and In Vivo Study,” *Ultrasound Med. Biol.*, vol. 41, no. 1, pp. 99–113, Jan. 2015.
- [143] A. Kheradvar, H. Houle, G. Pedrizzetti, G. Tonti, T. Belcik, M. Ashraf, J. R. Lindner, M. Gharib, and D. Sahn, “Echocardiographic Particle Image Velocimetry: A Novel Technique for Quantification of Left Ventricular Blood Vorticity Pattern,” *J. Am. Soc. Echocardiogr.*, vol. 23, no. 1, pp. 86–94, 2010.
- [144] H. Gao, B. Heyde, and J. D’hooge, “3D Intra-cardiac flow estimation using speckle tracking: A feasibility study in synthetic ultrasound data,” in *2013 IEEE International Ultrasonics Symposium (IUS)*, 2013, pp. 68–71.
- [145] J. Voorneveld, A. Muralidharan, T. Hope, H. J. Vos, P. Kruizinga, A. F. W. van der Steen, F. J. H. Gijsen, S. Kenjeres, N. de Jong, and J. G. Bosch, “High Frame Rate Ultrasound Particle Image Velocimetry for Estimating High Velocity Flow Patterns in the Left Ventricle,” *IEEE Trans. Ultrason. Ferroelectr. Freq. Control*, vol. 65, no. 12, pp. 2222 – 2232, 2017.
- [146] J. Voorneveld, L. B. H. Keijzer, M. Strachinaru, D. J. Bowen, J. S. L. Goei, F. J. ten Cate, A. F. W. van der Steen, N. de Jong, H. J. Vos, A. E. van den Bosch, and J. G. Bosch, “High Frame Rate echoPIV can Measure the High Velocity Diastolic Flow Patterns,” *Circ. Cardiovasc. Imaging*, vol. ‘in press’, 2019.
- [147] C. T. Metz, N. Baka, H. Kirisli, M. Schaap, S. Klein, L. A. Neefjes, N. R. Mollet, B. Lelieveldt, M. de Bruijne, W. J. Niessen, and T. van Walsum, “Regression-Based Cardiac Motion Prediction From Single-Phase CTA,” *IEEE Trans. Med. Imaging*, vol. 31, no. 6, pp. 1311–1325, Jun. 2012.
- [148] H. Saaïd, J. Voorneveld, C. Schinkel, J. Westenberg, F. Gijsen, P. Segers, P. Verdonck, N. De Jong, J. G. Bosch, S. Kenjeres, and T. Claessens, “Tomographic PIV in a model of the left ventricle : 3D flow past biological and mechanical heart valves,” *J. Biomech.*, vol. 90, pp. 40–49, 2019.
- [149] D. Bera, F. van den Adel, N. Radeljic-Jakic, B. Lippe, M. Soozande, M. A. P. Pertijs, M. D. Verweij, P. Kruizinga, V. Daeichin, H. J. Vos, A. F. W. van der Steen, J. G. Bosch, and N. de Jong, “Fast Volumetric Imaging Using a Matrix Transesophageal Echocardiography Probe with Partitioned Transmit–Receive Array,” *Ultrasound Med. Biol.*, vol. 44, no. 9, pp. 2025–2042, 2018.
- [150] F. Scarano and M. L. Riethmuller, “Advances in iterative multigrid PIV image processing,” *Exp. Fluids*, vol. 29, no. 7, pp. S051–S060, Dec. 2000.
- [151] J. Ahrens, B. Geveci, and C. Law, “ParaView: An End-User Tool for Large-Data Visualization,” in *Visualization Handbook*, no. January 2005, Elsevier, 2005, pp. 717–731.
- [152] S. G. Foster, P. M. Embree, and W. D. O’Brien, “Flow Velocity Profile via Time-Domain Correlation: Error Analysis and Computer Simulation,” *IEEE Trans. Ultrason. Ferroelectr. Freq. Control*, vol. 37, no. 3, pp. 164–175, 1990.
- [153] I. K. Ekroll, M. Wigen, S. Fadnes, and J. Adval, “Quantitative vascular blood flow imaging : A comparison of vector velocity estimation schemes,” in *IEEE International Ultrasonics Symposium (IUS)*, 2018, pp. 1–4.
- [154] J. Voorneveld, S. Engelhard, H. J. Vos, M. M. P. J. Reijnen, F. Gijsen, M. Versluis, E. G.

- Jebbink, N. de Jong, and J. G. Bosch, "High Frame Rate Contrast-Enhanced Ultrasound for Velocimetry in the Human Abdominal Aorta," *IEEE Trans. Ultrason. Ferroelectr. Freq. Control*, vol. 65, no. 12, pp. 2245 – 2254, 2018.
- [155] A. Yu and L. Lovstakken, "Eigen-based clutter filter design for ultrasound color flow imaging: a review," *IEEE Trans. Ultrason. Ferroelectr. Freq. Control*, vol. 57, no. 5, pp. 1096–1111, May 2010.
- [156] A. M. S. Omar, S. Vallabhajosyula, and P. P. Sengupta, "Left Ventricular Twist and Torsion," *Circ. Cardiovasc. Imaging*, vol. 8, no. 6, pp. 74–82, Jun. 2015.
- [157] J. Voorneveld, P. Kruizinga, H. J. Vos, F. J. H. Gijssen, E. G. Jebbink, A. F. W. van der Steen, N. de Jong, and J. G. Bosch, "Native blood speckle vs ultrasound contrast agent for particle image velocimetry with ultrafast ultrasound - in vitro experiments," in *2016 IEEE International Ultrasonics Symposium (IUS)*, 2016.
- [158] C. A. V. Hoyos, M. B. Stuart, K. L. Hansen, M. B. Nielsen, and J. A. Jensen, "Accurate Angle Estimator for High-Frame-Rate 2-D Vector Flow Imaging," *IEEE Trans. Ultrason. Ferroelectr. Freq. Control*, vol. 63, no. 6, pp. 842–853, 2016.
- [159] M. Wigen and L. Lovstakken, "In vivo three-dimensional intra-cardiac vector flow imaging using a 2D matrix array transducer," *IEEE Int. Ultrason. Symp. IUS*, vol. 2016-Novem, pp. 2–5, 2016.
- [160] J. Faurie, M. Baudet, K. C. Assi, D. Auger, G. Gilbert, F. Tournoux, and D. Garcia, "Intracardiac Vortex Dynamics by High-Frame-Rate Doppler Vortography — In Vivo Comparison With Vector Flow Mapping and 4-D Flow MRI," vol. 64, no. 2, pp. 424–432, 2017.
- [161] S. N. Doost, D. Ghista, B. Su, L. Zhong, and Y. S. Morsi, "Heart blood flow simulation: a perspective review.," *Biomed. Eng. Online*, vol. 15, no. 1, p. 101, 2016.
- [162] R. J. van der Geest and P. Garg, "Advanced Analysis Techniques for Intra-cardiac Flow Evaluation from 4D Flow MRI," *Curr. Radiol. Rep.*, vol. 4, no. 7, p. 38, 2016.
- [163] A. Nilsson, K. M. Bloch, J. Töger, E. Heiberg, and F. Ståhlberg, "Accuracy of four-dimensional phase-contrast velocity mapping for blood flow visualizations: a phantom study," 2013.
- [164] C. Binter, V. Knobloch, R. Manka, A. Sigfridsson, and S. Kozerke, "Bayesian Multipoint Velocity Encoding for Concurrent Flow and Turbulence Mapping," vol. 1345, pp. 1337–1345, 2013.
- [165] J. Kweon, D. H. Yang, G. B. Kim, N. Kim, M. Y. Paek, A. F. Stalder, A. Greiser, and Y. H. Kim, "Four-dimensional flow MRI for evaluation of post-stenotic turbulent flow in a phantom: comparison with flowmeter and computational fluid dynamics," *Eur. Radiol.*, vol. 26, no. 10, pp. 3588–3597, 2016.
- [166] J. Lee, S. Ko, J.-H. Cho, and S. Song, "Validation of magnetic resonance velocimetry for mean velocity measurements of turbulent flows in a circular pipe," *J. Mech. Sci. Technol.*, vol. 31, no. 3, pp. 1275–1282, 2017.
- [167] C. Montalba, J. Urbina, J. Sotelo, M. E. Andia, C. Tejos, P. Irrarrazaval, D. E. Hurtado, I. Valverde, and S. Uribe, "Variability of 4D Flow Parameters When Subjected to Changes in MRI Acquisition Parameters Using a Realistic Thoracic Aortic Phantom," vol. 00, no. April, 2017.
- [168] J. J. M. W. Pankaj Garg, F. G. J. T. Pieter J. van den Boogaard, Peter P. Swoboda, Rahoz

- Aziz, James R.J. Foley, MBChB, Graham J. Fent, and S. P. L. Coratella, Mohammed S.M. ElBaz, R.J. van der Geest, David M. Higgins, John P. Greenwood, "Comparison of Fast Acquisition Strategies in Whole-Heart Four-Dimensional Flow Cardiac MR: Two-Center, 1.5 Tesla, Phantom and In Vivo Validation Study," *Magn. Reson. Imaging*, no. April, 2017.
- [169] S. Kozerke, J. M. Hasenkam, E. M. Pedersen, and P. Boesiger, "Visualization of Flow Patterns Distal to Aortic Valve Prostheses in Humans Using a Fast Approach for Cine 3D Velocity Mapping," vol. 698, pp. 690–698, 2001.
- [170] I. Khodarahmi, M. Shakeri, M. Kotys-traughber, S. Fischer, M. K. Sharp, and A. A. Amini, "In Vitro Validation of Flow Measurement With Phase Contrast MRI at 3 Tesla Using Stereoscopic Particle Image Velocimetry and Stereoscopic Particle Image Velocimetry-Based Computational Fluid Dynamics," vol. 1485, pp. 1477–1485, 2014.
- [171] J. Töger, S. Bidhult, J. Revstedt, M. Carlsson, and E. Heiberg, "Independent validation of four-dimensional flow MR velocities and vortex ring volume using particle imaging velocimetry and planar laser-Induced fluorescence," *Magn. Reson. Med.*, vol. 75, no. 3, pp. 1064–1075, 2016.
- [172] S. B. Jelena Bock, Johannes Toger and M. C. Karin Markenroth Bloch, Per Arvidsson, Mikael Kansk, Hakan Arheden, Frederik Testud, Andreas Greiser, Einar Heiberg, "Validation and reproducibility of cardiovascular 4D-flow MRI from two vendors using 2 x 2 parallel imaging acceleration in pulsatile flow phantom and in vivo with and without respiratory gating," *Acta radiol.*, vol. 60, no. 3, pp. 327–337, 2019.
- [173] V. Knobloch, C. Binter, U. Gülan, A. Sigfridsson, M. Holzner, B. Lüthi, and S. Kozerke, "Mapping mean and fluctuating velocities by Bayesian multipoint MR velocity encoding-validation against 3D particle tracking velocimetry," *Magn. Reson. Med.*, vol. 71, no. 4, pp. 1405–1415, 2014.
- [174] A. roldan-alzate R.medero, c. hoffman, "Comparison of 4D Flow MRI and Particle Image Velocimetry Using an In Vitro Carotid Bifurcation Model," *Ann. Biomed. Eng.*, vol. 46, no. 12, pp. 2112–2122, 2018.
- [175] C. J. Elkins, M. Markl, N. Pelc, and J. K. Eaton, "4D Magnetic resonance velocimetry for mean velocity measurements in complex turbulent flows," *Exp. Fluids*, vol. 34, pp. 494–503, 2003.
- [176] I. Marshall, "Feasibility of k-t BLAST Technique for Measuring 'Seven-Dimensional' Fluid Flow," vol. 196, no. January, pp. 189–196, 2006.
- [177] P. Van Ooij, A. Guédon, C. Poelma, J. Schneiders, and M. C. M. Rutten, "Complex flow patterns in a real - size intracranial aneurysm phantom : phase contrast MRI compared with particle image velocimetry and computational fluid dynamics," *NMR Biomed.*, no. January 2011, pp. 14–26, 2012.
- [178] J. Urbina, J. A. Sotelo, D. Springmüller, C. Montalba, K. Letelier, C. Tejos, P. Irrarázaval, M. E. Andia, R. Razavi, I. Valverde, and S. A. Uribe, "Realistic aortic phantom to study hemodynamics using MRI and cardiac catheterization in normal and aortic coarctation conditions," *J. Magn. Reson. Imaging*, vol. 44, no. 3, pp. 683–697, 2016.
- [179] H. Ha, G. B. Kim, J. Kweon, H. K. Huh, S. J. Lee, J. Koo, J. Kang, T. Lim, D. Kim, and Y. Kim, "Turbulent Kinetic Energy Measurement Using Phase Contrast MRI for Estimating the Post- Stenotic Pressure Drop: In Vitro Validation and Clinical

- Application,” *PLoS One*, pp. 1–14, 2016.
- [180] A. T. Lee, G. B. Pike, and N. J. Pelc, “Three-Point Phase-Contrast Velocity Measurements with Increased Velocity-to-Noise Ratio,” *Magn. Reson. Imaging*, vol. 33, pp. 122–126, 1995.
- [181] S. Schnell, S. A. Ansari, C. Wu, J. Garcia, I. G. Murphy, O. A. Rahman, A. A. Rahsepar, M. Aristova, J. D. Collins, J. C. Carr, and M. Markl, “Accelerated Dual- venc 4D Flow MRI for Neurovascular Applications,” *J. Magn. Reson. Imaging*, pp. 1–13, 2017.
- [182] T. Puisseux, A. Sewonu, O. Meyrignac, F. Nicoud, S. Mendez, and R. Moreno, “Reconciling PC-MRI and CFD : An in-vitro study,” no. December 2018, pp. 1–14, 2019.
- [183] H. A. Kirişli, M. Schaap, and S. Klein, “Evaluation of a multi-atlas based method for segmentation of cardiac CTA data : a large-scale , multicenter , and multivendor study,” *Am. Assoc. Phys. Med.*, vol. 37, pp. 6279–6291, 2010.
- [184] K. P. Pruessmann, M. Weiger, M. B. Scheidegger, and P. Boesiger, “SENSE : Sensitivity Encoding for Fast MRI,” vol. 962, pp. 952–962, 1999.
- [185] M. A. Bernstein, X. J. Zhou, J. A. Polzin, K. F. King, A. Ganin, N. J. Pelc, and G. H. Glover, “Concomitant Gradient Terms in Phase Contrast MR: Analysis and Correction,” pp. 300–308.
- [186] A. P. Yoganathan, K. B. Chandran, and F. Sotiropoulos, “Flow in prosthetic heart valves: State-of-the-art and future directions,” *Ann. Biomed. Eng.*, vol. 33, no. 12 SPEC. ISS., pp. 1689–1694, 2005.
- [187] A. Kheradvar, E. M. Groves, A. Falahatpisheh, M. K. Mofrad, S. Hamed Alavi, R. Tranquillo, L. P. Dasi, C. A. Simmons, K. Jane Grande-Allen, C. J. Goergen, F. Baaijens, S. H. Little, S. Canic, and B. Griffith, “Emerging Trends in Heart Valve Engineering: Part IV. Computational Modeling and Experimental Studies,” *Ann. Biomed. Eng.*, vol. 43, no. 10, pp. 2314–2333, 2015.
- [188] I. Borazjani, J. Westerdale, E. M. McMahon, P. K. Rajaraman, J. J. Heys, and M. Belohlavek, “Left ventricular flow analysis: Recent advances in numerical methods and applications in cardiac ultrasound,” *Comput. Math. Methods Med.*, vol. 2013, no. March, 2013.
- [189] V. Vedula, S. Fortini, J. H. Seo, G. Querzoli, and R. Mittal, “Computational modeling and validation of intraventricular flow in a simple model of the left ventricle,” *Theor. Comput. Fluid Dyn.*, vol. 28, no. 6, pp. 589–604, 2014.
- [190] R. Asami, T. Tanaka, K. Kawabata, K. Hashiba, T. Okada, and T. Nishiyama, “Accuracy and limitations of vector flow mapping: left ventricular phantom validation using stereo particle image velocimetry,” *J. Echocardiogr.*, 2016.
- [191] M. Siebes and Y. Ventikos, “The role of biofluid mechanics in the assessment of clinical and pathological observations: Sixth international bio-fluid mechanics symposium and workshop, March 28-30, 2008 Pasadena, California,” *Ann. Biomed. Eng.*, vol. 38, no. 3, pp. 1216–1224, 2010.
- [192] F. Domenichini, G. Querzoli, A. Cenedese, and G. Pedrizzetti, “Combined experimental and numerical analysis of the flow structure into the left ventricle,” *J. Biomech.*, vol. 40, no. 9, pp. 1988–1994, 2007.
- [193] S. Gesemann, “From Particle Tracks to Velocity and Acceleration Fields Using B-Splines and Penalties,” *Phys. Fluids A Fluid Dyn.*, 2018.

